Université Pierre et Marie Curie

Ecole doctorale 388

Laboratoire de Chimie-Physique – Matière et Rayonnement

Diffusion résonante des rayons X mous dans la glace de spins artificielle

Resonant Soft X-Ray Scattering on Artificial Spin Ice

Par Jonathan Perron

Thèse de doctorat de Chimie Physique et Chimie Analytique de Paris Centre

Dirigée par le Pr. Jan Lüning

Présentée et soutenue publiquement le 29 septembre 2014

Devant un jury composé de :

Marrows Christopher, Professeur, Université de Leeds, Rapporteur
Ravy Sylvain, Directeur de Recherche CNRS, Synchrotron SOLEIL, Rapporteur
Cugliandolo Leticia, Professeur, Université Pierre et Marie Curie
Allenspach Rolf, Chef de groupe, IBM Research Zürich
Heyderman Laura, Professeur, Paul Scherrer Institut/ETH Zürich, Co-encadrante
Lüning Jan, Professeur, Université Pierre et Marie Curie, Directeur de thèse

Except where otherwise noted, this work is licensed under
http://creativecommons.org/licenses/by-nc-nd/3.0/

Université Pierre et Marie Curie

Ecole doctorale 388

Laboratoire de Chimie-Physique – Matière et Rayonnement

Diffusion résonante des rayons X mous dans la glace de spins artificielle

Resonant Soft X-Ray Scattering on Artificial Spin Ice

Par Jonathan Perron

Thèse de doctorat de Chimie Physique et Chimie Analytique de Paris Centre

Dirigée par le Pr. Jan Lüning

Présentée et soutenue publiquement le 29 septembre 2014

Devant un jury composé de :

Marrows Christopher, Professeur, Université de Leeds, Rapporteur
Ravy Sylvain, Directeur de Recherche CNRS, Synchrotron SOLEIL, Rapporteur
Cugliandolo Leticia, Professeur, Université Pierre et Marie Curie
Allenspach Rolf, Chef de groupe, IBM Research Zürich
Heyderman Laura, Professeur, Paul Scherrer Institut/ETH Zürich, Co-encadrante
Lüning Jan, Professeur, Université Pierre et Marie Curie, Directeur de thèse

Except where otherwise noted, this work is licensed under
http://creativecommons.org/licenses/by-nc-nd/3.0/

Remerciements

En premier lieu, je tiens à remercier Jan Lüning pour avoir été mon directeur de thèse pendant ces trois années. Il a su me transmettre sa passion et son enthousiasme pour la recherche en me prodiguant de nombreux conseils tout au long de mon doctorat. Il m'a donné l'extraordinaire opportunité de pouvoir donner une composante internationale à ce travail en ayant effectué une partie en Suisse, mais également de participer à différents projets avec des groupes en France et en Allemagne.

Je remercie Laura Heyderman pour m'avoir accepté dans son groupe de recherche à l'institut Paul Scherrer en Suisse. Sa patience et son organisation m'ont permis de progresser scientifiquement et humainement pendant l'année et demie passée au Laboratoire pour la Micro- et Nanotechnologie. Elle a su me rappeler les objectifs scientifiques et m'a donné les moyens de les atteindre.

Je veux remercier Luca Anghinolfi pour toute l'aide qu'il m'a apporté dans la réalisation du travail présenté ici. Les nombreuses discussions que nous avons eu, sa patience et sa bonne humeur ont rendu notre collaboration très productive et agréable.

Par extension, je veux remercier tous les membres du projet "artificial spin ice": Alan Farhan, Valerio Scagnoli et Oles Sendetskyi pour leurs aides, leurs patiences et leurs commentaires justifiés qui ont permis de mener le projet au point où il en est aujourd'hui. Je tiens à souligner que Valerio Scagnoli et Oles Sendetskyi sont à l'origine de l'expérience présentée figure 6.1, et je leur souhaite bonne chance pour la suite du projet.

Je remercie également tous les techniciens du Laboratoire de Micro- et Nanotechnologie pour l'aide qu'ils m'ont apporté à chaque fois que j'en ai eu besoin. En particulier, je veux remercier Anja Weber pour m'avoir appris toutes ses astuces sur la lithographie, et Vitalyi Guzenko pour son aide et ses connaissances. C'est grâce à eux que le procédé présenté dans le chapitre 2 a pu être développé.

L'expérience de diffusion des rayons X introduite dans la section 5.2 chapitre n'aurait pas pu être réalisée sans Urs Staub et d'Aurora Alberca qui nous ont accompagné pendant nos temps de faisceau à SLS. Un grand merci également à Joachim Kohlbrecher pour son soutien durant celui-ci, ainsi que pour ses remarques pertinentes. Je remercie également Josep Noguès and Patxi Lopez-Barbera pour les mesures MOKE présentées figure 4.2.

Merci à Nicolas Jaouen du synchrotron SOLEIL et Jean-Marc Tonnerre de l'institut Néel pour leurs aides, leurs conseils et leurs soutiens pendant les temps de faisceau, et lorsqu'est venu le temps de comprendre les résultats présentés dans le chapitre 4. Merci également à Bharati Tudu du LCP-MR pour son énorme soutien lors de notre premier temps de faisceau en Juin 2012. Je ne peux également que remercier Horia Popescu du synchrotron SOLEIL pour son aide et ses précieux conseils quand est venu le temps de travailler sur la nouvelle chambre de la ligne SEXTANTS, brièvement introduite dans l'annexe C. Son optimisme et sa bonne humeur ont été plus que bienvenue pour la résolution des nombreux problèmes que nous avons affronté...

Enfin, je tiens à remercier tous les membres du groupe au sein du LCP-MR : Boris

Vodungbo, Renaud Delaunay et Sorin Chiuzbaian pour leurs conseils et leurs soutiens pendant l'année et demie passée à Paris. Je remercie également Régis Vacheresse ainsi que les mécaniciens du laboratoire, Hugues Ringuenet, Pascal Leroy et Chérif Filali, pour leurs conseils techniques grâce auxquels j'ai appris les rudiments de la mécanique et leurs réactions rapides lors de l'assemblage de la nouvelle chambre expérimentale.

Finalement, je veux remercier toutes celles et ceux qui m'ont soutenu et aidé pendant ces trois années. J'espère qu'ils m'excuseront de ne pas les nommer, par crainte de ma part d'oublier quelqu'un.

Contents

Introduction **15**

1 Artificial spin ice in the literature **17**
1.1 Water ice . . . 18
1.2 Basics notions of magnetism . . . 19
1.2.1 Hysteresis . . . 19
1.2.2 Magnetic domain . . . 19
1.2.3 Interactions in ferromagnets . . . 20
1.3 Spin ice . . . 23
1.4 Artificial spin ice . . . 24
1.4.1 Stoner-Wohlfarth model . . . 25
1.4.2 Artificial square ice . . . 25
1.4.3 Artificial kagome spin ice . . . 27
1.4.4 Current state of research . . . 28
1.5 The place of this work . . . 29

2 Fabrication **31**
2.1 Introduction . . . 32
2.2 First step: spin-coating . . . 34
2.3 Second step: electron-beam writing . . . 35
2.3.1 Introduction . . . 35
2.3.2 Sequence file . . . 37
2.3.3 Shape correction . . . 37
2.3.4 Development . . . 38
2.4 Third step: deposition of the magnetic material . . . 39
2.4.1 Metal evaporation . . . 39
2.5 Final step: Lift-off . . . 39
2.6 Thin film characterization . . . 40
2.6.1 Film thickness . . . 40
2.6.2 Structural characterization . . . 40
2.6.3 Magnetic characterization . . . 41
2.7 Summary . . . 42

3 Photon-matter interactions **43**
3.1 Absorption and resonant scattering of x-rays . . . 44
3.1.1 Absorption and Magnetic Circular Dichroism . . . 44
3.1.2 Resonant magnetic x-ray scattering . . . 47
3.2 Measuring in reciprocal space . . . 51
3.2.1 Unit cell . . . 52

3.2.2 Bragg diffraction . . . 52
3.2.3 Ewald's construction . . . 54

4 Resonant scattering on artificial spin ice 57
4.1 Method . . . 58
4.1.1 Sample preparation and characterization . . . 58
4.1.2 Experimental set-up . . . 59
4.2 Kinematic theory of x-ray diffraction . . . 62
4.2.1 Kinematic theory . . . 62
4.2.2 Extension of the theory to two dimensions . . . 64
4.2.3 Simulations . . . 65
4.3 Bragg scattering on artificial square ice . . . 65
4.3.1 As-grown ordering . . . 65
4.3.2 First magnetization curve . . . 66
4.3.3 Magnetization reversal . . . 70
4.3.4 Determination of the nanomagnet contributions to the remanent magnetization . . . 71
4.4 Diffuse scattering on an artificial kagome ice array . . . 76
4.4.1 As-grown state . . . 76
4.4.2 First magnetization . . . 77
4.4.3 Field dependency of the diffuse scattering . . . 78
4.4.4 Analysis of the diffuse scattering : difficulties and solutions . . . 80
4.4.5 Evolution of the dichroic contrast during magnetization reversal . . . 81
4.5 Summary . . . 84

5 Complementary studies 85
5.1 Induced disorder in artificial square ice . . . 86
5.2 Temperature dependence of the scattering pattern . . . 87
5.3 Summary . . . 89

6 Conclusion and outlooks 91
6.1 Summary and conclusions . . . 91
6.2 Outlooks . . . 92

A Fabrication 97

B Algorithms 99

C Instrumentation 103

Bibliography 105

Résumé 117

List of Figures

1.1 Water and spin ice structures . . . 17
1.2 Magnetic hysteresis . . . 20
1.3 Magnetic domains . . . 20
1.4 Stoner-Slater model . . . 22
1.5 Effect of the shape anisotropy . . . 23
1.6 Geometrical frustration . . . 23
1.7 Stoner-Wohlfarth model . . . 25
1.8 Coupled nanomagnets in artificial square ice and types of vertices . . . 26
1.9 Ice rules in artificial kagome ice . . . 27

2.1 Artificial spin ice structures produced by electron-beam lithography . . . 32
2.2 Fabrication steps . . . 33
2.3 Failed lift-off . . . 35
2.4 Simplified schematic of an electron-beam writer . . . 36
2.5 Electron trajectories in the case of forward scattering calculated by Monte-Carlo method . . . 37
2.6 Exposure pattern . . . 38
2.7 Observation of proximity effect in an artificial kagome spin ice . . . 38
2.8 Metal evaporation . . . 39
2.9 Cross-section and diffraction pattern of a Permalloy thin film . . . 40
2.10 Cross-section and diffraction pattern of a Permalloy thin film . . . 41
2.11 Defects in a Permalloy thin films . . . 41
2.12 EDX spectrum of a Permalloy thin films . . . 42
2.13 Hysteresis loop of a Permalloy thin film . . . 42

3.1 Resonant photon-in photon-out processes . . . 43
3.2 X-ray magnetic circular dichroism . . . 47
3.3 Unit cells . . . 52
3.4 X-ray diffraction . . . 54
3.5 Miller indices . . . 54
3.6 Ewald's construction . . . 55

4.1 SEM pictures of artificial square and kagome spin ice arrays . . . 58
4.2 NanoMOKE hysteresis curves of patterned Permalloy thin films . . . 60
4.3 Magnetic configurations of artificial square ice . . . 60
4.4 Single magnetic domain . . . 60
4.5 RESOXS endstation at beamline SEXTANTS . . . 61
4.6 Rocking curve recorded for an artificial square ice array with an incident angle of 10° . . . 62

4.7 Scattering geometry . . . 65
4.8 Scattering pattern on artificial spin ice in the as-grown state . . . 67
4.9 Scattering patterns recorded at 707 eV during the first application of an external field . . . 68
4.10 Evolution of the magnetic Bragg peaks intensities . . . 69
4.11 Magnetic dichroism of the scattering pattern recorded at opposite saturation 70
4.12 XMCD contrast of the selected Bragg peaks at remanence as a function of applied field . . . 72
4.13 Form factors . . . 73
4.14 Comparison between experimental and numerical dichroic scattering patterns 74
4.15 Micromagnetic simulation of a vertex at remanence following saturation . . 75
4.16 Simulated dichroic intensity as a function of the total number of reversed magnetic moments . . . 76
4.17 Artificial kagome ice in the as-grown state . . . 77
4.18 Evolution of the scattering pattern during the first magnetization . . . 78
4.19 Diffuse scattering during magnetization reversal . . . 79
4.20 Effect of the angle between external magnetic field and kagome lattice . . . 80
4.21 Simulated scattering patterns for different Dirac strings . . . 81
4.22 Analysis of the diffuse scattering . . . 82
4.23 Artificial kagome ice saturated . . . 83
4.24 Dichroic scattering patterns recorded on the same branch of the hysteresis . 83
4.25 Dichroic scattering pattern recorded with a tilt of 7 degrees . . . 84

5.1 Induced disorder in artificial square ice . . . 87
5.2 Effect of induced disorder on the scattering pattern . . . 87
5.3 Evolution of the scattering pattern with the temperature . . . 88
5.4 Comparison between 2D and 1D measurements . . . 88

6.1 2D scattering patterns on thermally activated artificial spin ice . . . 93
6.2 Scattering and frequencies accessible with spectroscopic techniques . . . 94

A.1 Artificial square ice created by electron-beam lithography . . . 98
A.2 Artificial kagome ice created by electron-beam lithography . . . 98

B.1 Determination of the spin value . . . 99
B.2 Computation of distances . . . 100
B.3 Nomenclature of the correlations . . . 100
B.4 Correlation ν,β and γ . . . 101
B.5 Correlation δ and τ . . . 101

C.1 Different views of COSMOS . . . 103
C.2 Experimental chamber . . . 104
C.3 Detector chamber . . . 104

List of Tables

4.1 Degree of ground-state ordering during first magnetization 68

Acronyms

μSR muon spin rotation

AFM atomic force microscope

CCD charged-coupled device

EDX energy-dispersive x-rays

FTH Fourier transform holography

FWHM full width at half maximum

GS ground-state

HRTEM high-resolution transmission electron microscopy

MFM magnetic force microscopy

MOKE magneto-optic kerr effect

PEEM x-ray photoemission electron microscopy

PMMA polymethylmethacrylate

SAXS small angle x-ray scattering

SEM scanning electron microscopy

SXRMS soft x-ray resonant magnetic spectroscopy

TEM transmission electron microscopy

XAS x-ray absorption spectroscopy

XMCD x-ray magnetic circular dichroism

XPCS X-ray photon correlation spectroscopy

Introduction

Frustration is an intriguing property found in many physical systems. It occurs when all the interactions in a system cannot be satisfied simultaneously [1]. Examples of frustrated systems are amorphous materials (glasses) and magnetic materials. Since about 2006, the latter includes materials finely tailored using state-of-the-art lithographic techniques: the *artificial spin ice*. This material is composed of nanomagnets arranged on the sites of frustrated geometries reminding the organization of the magnetic moments in rare-earth pyrochlore crystals, also called *spin ice* [2]. The study of the properties of the artificial spin ice is a hot topic which has attracted an increasing amount of interest in the recent years [3, 4].

A strong motivation for studying artificial spin ice is the possibility to image them in real space using magnetic microscopy such as Lorentz microscopy [5], photoelectron emission microscopy [6] or magnetic force microscopy [7]. On the other hand, reciprocal space techniques such as neutron scattering have been mainly used for the investigation of spin ice [8]. In contrast with the natural system, artificial spin ice allows simpler experimental conditions. Spin ice behaviour is observed at room temperature and the frustration can be tuned by changing the interaction strength, or by designing new geometries.

Scattering furnishes information about the average structure of a material. Can one study the deviations from this average in order to investigate the properties of artificial spin ice ? This is the question which we address in this thesis. In the following, we will see that scattering can provide valuable information although the analysis is complicated [9].

The soft x-ray range proposes itself for this investigation. The wavelength is ideal to study materials within one tenth of a nanometre. Also, the energy range is compatible with the $L_{2,3}$ absorption edge of $3d$ transition metals used in artificial magnetic materials. In the past, soft x-ray scattering has been applied successfully to a wide range of magnetic metamaterials, including grating of nanolines [10], spin-valves [11] or sub-micron patterned films [12].

The organisation of this thesis is as follows. We introduce in the first chapter the artificial spin ice. Starting from the frustration in water ice and in the pyrochlore spin ice, we describe the properties of artificial spin ice due to the frustration. We also remind the reader of the key notions of magnetism to facilitate the understanding of the work presented here. A particular focus is given to the description of the individual nanomagnets. We conclude by the current state of research on this topic, and why soft x-ray scattering is complementary to microscopic techniques.

Chapter 2 is devoted to the fabrication of artificial spin ice. It gives an overall overview of the lithography techniques as well as some specific details about the strategy used to fabricate the samples employed in this work. We also discuss the characterization of magnetic thin films in this chapter.

Prior to the presentation of our results, chapter 3 contains the description of the different interactions between x-rays and matter, in particular the sensitivity to magnetism.

We also review briefly the basic notions of crystallography used in the following chapter.

The nanomagnets being characterized in the chapter 4 are the core of this thesis. We discuss Bragg scattering in artificial square ice, and show that statistical information can be obtained via the x-ray circular magnetic dichroism [13]. Diffuse scattering is also discussed in this chapter, and a tentative interpretation will be given.

The last chapter, chapter 5, is dedicated to additional soft x-ray studies performed on tuned artificial spin ice.

Following the conclusions and outlook, three annexes are given, the first one (Annex A) containing the experimental parameters used in the fabrication process described in chapter 2, the second one describing the algorithms developed and used for the analysis of correlations in artificial spin ice (Annex B). Annex C is dedicated to a new instrument located at the SOLEIL synchrotron. It is expected to bring new light on the fast dynamics of artificial spin ice, and more generally magnetic systems, via state-of-the-art x-ray techniques.

Chapter 1

Artificial spin ice in the literature

Contents

1.1 Water ice 18
1.2 Basics notions of magnetism 19
1.2.1 Hysteresis 19
1.2.2 Magnetic domain 19
1.2.3 Interactions in ferromagnets 20
1.3 Spin ice 23
1.4 Artificial spin ice 24
1.4.1 Stoner-Wohlfarth model 25
1.4.2 Artificial square ice 25
1.4.3 Artificial kagome spin ice 27
1.4.4 Current state of research 28
1.5 The place of this work 29

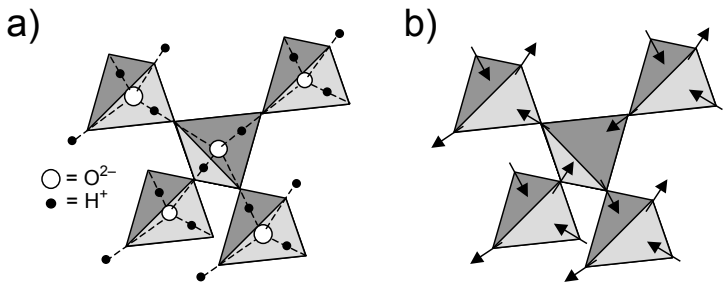


Figure 1.1: a) Water ice and b) spin ice structures. After Snyder *et al.* [2]

As briefly mentioned in the introduction, artificial spin ice belongs to a class of metamaterials exhibiting magnetic frustration. We cannot go further without giving more details about the two keywords "metamaterial" and "frustration". The first refers to the materials which are tailored in order to produce entities with specific properties, often by means of state-of-the-art methods. The second is the physical phenomenon occuring when all the interactions of a system cannot be satisfied simultaneously. From these very succinct definitions arise several questions such as "how can a system be tailored to exhibit magnetic frustration ?" or "what are the properties of such a system ?". We answer these questions through this first chapter which has been written to give to the reader the key information to understand the nature and properties of artificial spin ice.

How can a system be tailored to exhibit magnetic frustration ? And we can add the following question: what is frustration in magnetic systems ? In the first three sections, we address these two questions by reviewing the two systems which inspired the creation of artificial spin ice. In section 1.1, we describe one of the very first frustrated systems studied, the (water) ice. The organization of the hydrogen atoms in ice can be compared to the organization of the magnetic moments in the magnetic rare-earth pyrochlores, a class of crystal often referred to as spin ice [2] (section 1.3). In between these two sections, we remind the reader the basic concepts in magnetism, which will be used in 1.3 and in the rest of this thesis, in particular the different magnetic interactions.

What are the properties of artificial spin ice ? In the last section 1.4, we describe in detail this system, by focusing on the system which we have studied using soft x-ray magnetic scattering (chapter 4). The first subsection is dedicated to the *Stoner-Wohlfarth* model which offers a simple description of the individual nanomagnets composing the artificial spin ice. We describe both artificial square ice and artificial kagome ice, the two most commonly investigated systems. A small subsection is dedicated to the current state of the research which evolved quickly over the last years. Finally, the last subsection is devoted to the place of this work in the framework of the tools which can, or has been, used to study the intriguing properties present in these magnetic materials.

1.1 Water ice

From Antiquity, where it was considered as one of the four elements composing nature, to more recent days, its chemical composition was discovered thanks to the work from Cavendish and Lavoisier [14, 15], water has always attracted a lot of scientific interest.

At the beginning of the twentieth century, the structure of ice was solved by use of x-ray diffraction [16]. Bernal and Fowler found that the water molecules are arranged such as an oxygen atom is surrounded by four hydrogen atoms in a tetrahedron configuration (figure 1.1a); they gave the name *ice rules* to describe this peculiar arrangement [16]. The hydrogen atoms are located either close (covalent bonding) or far (hydrogen bond) from the oxygen atoms, thus forming a *two-in two-out* state [3].

One consequence is the frustration of the system as the energy of all oxygen-hydrogen interactions cannot be minimized at the same time, which would require the hydrogen atoms to be located at central positions between oxygen atoms. This leads to the degeneracy of the energy levels, and it is the origin of the non-zero value of the entropy of ice at temperatures close to the absolute zero point [17]; Pauling calculated that its value is equal to $R \ln 3/2$ at 0K, with R the gas constant [18]. [1]

[1] In a simpler approach, by using the definition of the entropy defined by Ludwig Boltzmann as : $S = k_B ln\Omega$ with k_B the Boltzmann constant and Ω the number of possible micro-states, we note that if the number of accessible states at a given temperature is more than 1, the entropy does not fall to zero.

1.2 Basics notions of magnetism

Magnetic materials can be classified as a function of the interactions dominating in the system. All materials exhibit a response when placed in an external magnetic field. Some present no net magnetization, due to the absence of long-range ordering between magnetic moments (diamagnetism, paramagnetism) or with an antiparallel alignment of equivalent moments at long-range (antiferromagnetism). If the moments are not equivalent, then the net magnetization is different from zero (ferrimagnetism).

When there is a long-range ordering of parallel equivalent moments, then the materials are called ferromagnetic. These materials are the most common magnets found in everyday life, and are known since the Antiquity. The response of the material magnetization $\mathbf{M}$ to an external field $\mathbf{H}$, the magnetic susceptibility χ, at a temperature T is given for ferromagnets by the Curie-Weiss law :

$$\chi = \frac{C}{T - T_c} \tag{1.1}$$

with C the Curie constant and T_c the Curie temperature. Below T_c, the interactions between magnetic moments is stronger than the thermal fluctuations, allowing the long-range ordering of the moments and thus the ferromagnetic state. Above T_c, the moments are disordered and the material is paramagnetic. In this thesis, we have worked with Permalloy ($Ni_{80}Fe_{20}$), a ferromagnetic material with a Curie Temperature of 450°.

1.2.1 Hysteresis

Another characteristic of ferromagnetic materials is the evolution of $\mathbf{M}$ when $\mathbf{H}$ is applied. This response is usually non-linear and depends of the material; this behaviour is called *hysteresis*. A typical representation is given in figure 1.2, which is called hysteresis loop or curve. Several important features characteristic of the system are retrieved from an hysteresis loop:

- the first magnetization curve;
- the magnetization at saturation (M_s) is the magnetization when $\mathbf{H}$ is strong enough to force all the magnetic moments to point parallel to the field direction;
- the magnetization at remanence (M_r) is the magnetization when $\mathbf{H}$ is removed following saturation;
- the coercive field ($\mathbf{H}_c$) is the value of $\mathbf{H}$ which cancel $\mathbf{M}$.

The first magnetization curve corresponds to the evolution of M with H when the sample starts in its virgin state. In this particuliar state, the magnetization at the macroscopic level is equal to zero, due to organization of the magnetic moments which prevent any stray field originating from the material.

1.2.2 Magnetic domain

On the microscopic level, the material in its virgin state is organized in several *magnetic domains*, regions where the magnetic moments are aligned parallel to each other (figure 1.3a) [19]. Magnetic domains exists to minimize the *stray field*, and thus to reduce the energy of the system (figure 1.3b). Two domains are separated by a domain wall, region where the magnetization is rotating either in-plane (Néel wall) or out-of-plane (Bloch wall).

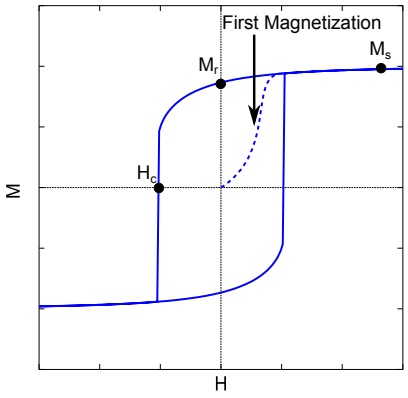


Figure 1.2: Magnetic hysteresis. The system starts in its virgin state, in which the magnetization is zero due to a large number of magnetic domains. A magnetic field **H** is applied on the system which forces all magnetic moments to point parallel to the field direction, thus destroying the magnetic domains. At saturation, all magnetic moments point in the direction of **H**. When the field is removed, some magnetic moments turn because of defects in the material for instance. The magnetization at remanence M_r is then slightly inferior to the value at saturation M_s. When **H** is applied in the opposite direction, the moments also rotate. At the coercivity H_c, the magnetization in the material is equal to zero.

These domain walls cost energy to the system, and in some cases it prefers to form only one magnetic domain (figure 1.3c), especially when the dimensions are very small (section 1.4.1).

1.2.3 Interactions in ferromagnets

The total energy E_{tot} of a ferromagnet is described as a sum of different terms, each one corresponding to an interaction:

$$E_{tot} \approx E_{ex} + E_a + E_d \tag{1.2}$$

where E_{ex} is the *exchange energy*, E_a the *magnetic anisotropy energy* and E_d the *dipolar energy*. A full description would require additional terms such as the Zeeman energy or

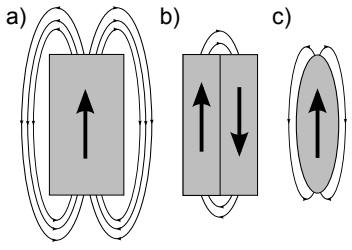


Figure 1.3: Magnetic domains. Each magnetic body produces a stray field (a). To minimize it, the system organizes itself into magnetic domains with opposite magnetization (b). These magnetic domains are separated by domain walls; these boundaries cost energy to create, and will be created only if they reduce efficiently the stray field. When dimensions are reduced, the magnets tend to be monodomaim (c), as creating a domain wall in this case would be too expensive compared to the reduction of the stray field.

the magnetostriction energy, but these play less of a role in the following, so we choose not give more details about them.

Exchange interaction

The origin of magnetic ordering between atomic spins mainly comes from the exchange interaction [20, 21]. The exchange interaction is arising from the competition between Coulomb interaction which favours the parallel alignment of magnetic moments and Pauli exclusion which does not allow two parallel electrons in the same quantum system [22]. This results in either a parallel or antiparallel alignment of the magnetic moments. In materials with localized magnetization on neighbouring atoms, the exchange interaction is described by the *Heisenberg exchange Hamiltonian* [20]:

$$H = -\sum_{i \neq j}^{N} J_{ij} \mathbf{S}_i \cdot \mathbf{S}_j = -\frac{1}{2} \sum_{i<j}^{N} J_{ij} \mathbf{S}_i \cdot \mathbf{S}_j \tag{1.3}$$

with J_{ij} the exchange constant between the spins $\mathbf{S}_i$ and $\mathbf{S}_j$. The sign determines the type of ordering:

- J_{ij} positive: parallel alignment;
- J_{ij} negative: antiparallel alignment.

Strictly spoken, this description is only valid for systems with localized magnetic moments. This is not the case in $3d$ transition metals such as Co, Ni and Fe, for which the electrons responsible for the magnetization are delocalized in energy bands (*itinerant ferromagnetism*). To understand how the exchange interaction is acting in these materials, we use the model originally developed by Mott, Slater and Stoner for the case of Ni (*Stoner-Slater model*, figure 1.4) [23–26].

In absence of a preferred axis (figure 1.4a), the reduction of the kinetic energy leads the electrons to favour an antiparallel alignment of their spins (equation (1.3)). In the $3d$ transition metals, the exchange interaction acts as an internal field which establish a favoured alignment axis (figure 1.4b). In the presence of this axis, the spins prefer to be aligned to each other, either parallel to the internal field or antiparallel. This creates two population of electrons, spins-up ($N_\uparrow$) and spins-down ($N_\downarrow$) (figure 1.4b) [19]. This leads to an increase of the kinetic energy, and the total energy of the system is lowered by splitting the valence band in two, a majority and a minority band (spin dependent potential). In this case, the exchange energy E_{ex} is expressed as [27]:

$$E_{ex} = J N_\uparrow N_\downarrow \tag{1.4}$$

with J the exchange constant as introduced above.

Dipolar interaction

Dipolar interaction is an other important interaction in magnetism. Less strong than exchange interaction, it has a longer range. It favours the antiparallel alignment of the magnetic moments through the reduction of their stray fields. For two dipoles with moments $\mathbf{m}_1$ and $\mathbf{m}_2$ separated by a distance r, the dipolar energy is given by [28]:

$$E_d = \frac{\mu_0}{r^3} \left[(\mathbf{m}_1 \cdot \mathbf{m}_2) - \frac{3}{r^2} (\mathbf{m}_1 \cdot \mathbf{r})(\mathbf{m}_2 \cdot \mathbf{r}) \right] \tag{1.5}$$

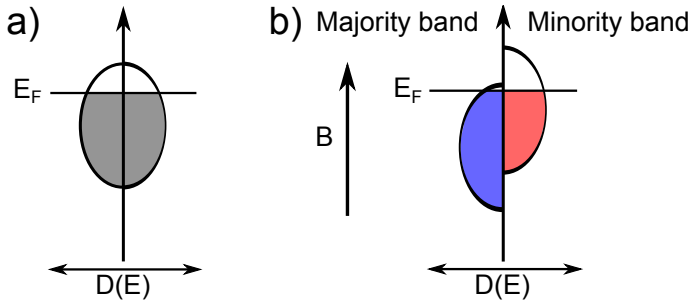


Figure 1.4: Stoner-Slater model. In non-magnetic systems (a), there is no difference between spin-up and spin-down population. In ferromagnets (b), the valence band splits into two components to reduce the total energy of the systems due to the difference between the two populations.

with μ_0 the vacuum permittivity. The second term in this equation (1.5) shows the direction dependency of the dipolar interaction, on contrary to the exchange interaction [28].

As we will describe in the following, the dipolar interaction is responsible for the magnetic frustration in the artificial spin ice, in particular because of the geomeotry of these systems which prevents the minimization of all dipolar interactions at the same time (section 1.4).

Magnetic anisotropy

Often referred to as the dependence of the magnetic properties with the direction [22], magnetic anisotropy gives rise to the existence of *easy* and *hard axes of magnetization* in magnetic materials. The easy axis corresponds to the direction along which the magnetization will point, while aligning the magnetization with the hard axis will require the application of an external magnetic field. In addition, the magnetization rotates back to the easy axis when the field is removed

There are several sources of magnetic anisotropy. In crystals, the magnetocrystalline anisotropy forces the magnetization along preferred crystalline directions. In nano-patterned media, shape of the nanomagnets can be tailored to favour the alignment of the magnetization (figure 1.5). *The shape anisotropy* allows the reduction of the stray field originating from the particle by closing the magnetic magnetic flux [22]. Let us consider the nanomagnets of figure 1.5. In panel a), the square shape of the particle allows the existence of four magnetic domains separated by domain walls; there is no stray field originating from the nanomagnet due to the closed loop. On the contrary in panel b), the shape forces the magnetization to point along the long direction of the particle. The stray field is thus not cancelled, but the size and volume of the nanomagnet does not allow the nucleation of a domain wall, which would cost even more energy. An additional reason for such a difference is the distribution of the stray field. While for the ellipsoid shape, the distribution of the stray field is uniform over the whole volume of the particle, it is absolutely not the case for the square shape [29].

For the ellipsoid nanomagnet of figure 1.5b with a volume V, the energy term corresponding to the shape anisotropy is written as:

$$E_a = KVsin^2(\varphi) \tag{1.6}$$

with K the uniaxial anisotropy constant and φ as defined in figure 1.7.

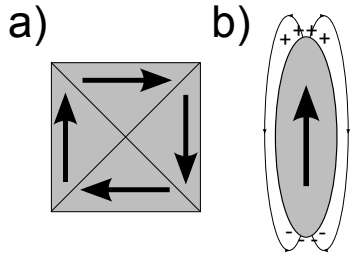


Figure 1.5: Effect of the shape anisotropy. The square shape (a) allows the existence of magnetic domains separated by domain walls. The magnetic loop is closed, thereby there is no stray field. On the contrary, the shape (b) forces the magnetization to point along the long direction of the nanomagnets. The stray field is not reduced because the size and volume does not allow the nucleation of domain wall

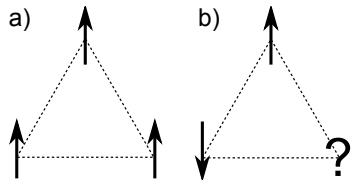


Figure 1.6: Geometrical frustration. Let us consider three spins arranged on a triangular lattice. In the case of ferromagnetism, there is one possibility to arrange them on the lattice (a); in this case, there is no frustration as all exchange interactions are equivalent. For an antiferromagnetic interaction, there are two possibilities to place the third spin on the lattice (b). However in both case, frustration will occur because of the alignment between spins : one is parallel and the other one antiparallel.

Geometrical frustration and magnetism

The geometry can prevent the simultaneous minimization of all interactions, typically exchange and/or dipolar, which leads to frustration [1, 30]. We present in figure 1.6 a simple example with three magnetic moments arranged on a triangular array. If the spins are ferromagnetically coupled, there is no frustration (figure 1.6a). On the other hand, if the spins are antiferromagnetically coupled, two possibilities exist to arrange the three spins, but neither of them will minimize all interactions (figure 1.6b). As a consequence, there are two states with the same energy, as it it equivalent to have the magnetic moments pointing up or down.

1.3 Spin ice

Spin ice is a family of compounds which exhibit intriguing properties, especially at low temperatures. The generic chemical composition is $A_2B_2O_7$ with A a magnetic rare-earth ion and B a non-magnetic transition metal. Their crystal adopts the pyrochlore crystalline structure (space group $Fd\bar{3}m$). The magnetic ions are located at the corner of the corner-sharing tetrahedra structure (figure 1.1b).

This structure is known to give rise to frustrated magnetic systems [1]. At low temperatures, the spins cannot rotate freely due to the crystal field anisotropy, but they are aligned along the (111) direction with their magnetic moments pointing either toward or away from the centre of the tetrahedron. The reader can note that this situation is similar to the hydrogen organization in water ice (figure 1.1). This behaviour has been observed

in several crystals such as $Ho_2Ti_2O_7$ [31,32], $Dy_2Ti_2O_7$ [2,33] or $Ho_2Sn_2O_7$ [34].

Origin of frustration

In a single tetrahedron of a pyrochlore structure, three different interactions can be distinguished, one related to the structure and two related to magnetism. As mentioned before, the crystal anisotropy forces the magnetic moments to be aligned along the (111) direction but do not fix their direction. Between spins dipolar coupling exists, which tends to minimize the magnetic stray field in the system. We should not forget that spin-ice crystals are composed of ions which are described by quantum physics, therefore, we also need to consider the exchange interaction between ions. This favours anti-parallel alignment between similar objects (Pauli exclusion principle). At room temperature, the two magnetic interactions are in competition with the thermal energy which renders the system paramagnetic. When cooling to low temperature, there is competition between exchange and dipolar interaction which leads to a degeneration of the energy of the system. Indeed, it is not possible to satisfy both interactions. In the simplest case of tetrahedron of four spins, 2^4 energy states exist. Out of these 16 states, 6 have the lowest energy [2,31]. They are described by the *ice rules*: two spins point toward the centre of the tetrahedron and two spins point away. Similar to water ice, the entropy value at low temperature is different from zero. Ramirez and co-workers determined by heat capacity measurements this value to be equal to $0.67R\ln 2$, which is close to the value of $0.71R\ln 2$ calculated by Pauling for the water ice [35]. The small difference between both values is related to the energetic barriers to spin reorientation in the spin ice.

Magnetic ordering

The origin of magnetic correlations in spin-ice crystals remained an elusive question for a number of years. Indeed, how can one combine the ice rules, which are limited to the nearest neighbouring ions, with the strong magnetic moment of rare earth ions ($10\mu_B$ for Ho^{3+}, with μ_B the Bohr magnetron [36]), which leads to long-range correlations through dipolar coupling. In 2001, Bramwell and co-workers showed that neutron scattering patterns indicates that nearest neighbour interactions are predominant in the system while theoretical models were based on long-range interactions [37]. This question has been solved with the use of an elegant model which demonstrates that the origin of the ice rules is the dipolar coupling between magnetic moments. Using weak antiferromagnetic interactions between nearest-neighbours, Isakov *et al.* have explained the origin of ordering in spin ice [38].

1.4 Artificial spin ice

For two reasons, the physics of spin ice is difficult to investigate. As we have mentioned in the previous section, one needs to work at low temperatures to observe the spin ice behaviour, which imposes a technical difficulty for experiments. The second reason is related to the experimental techniques used (neutron scattering [8,32], muon-spin rotation [39]). The experimental results can be difficult to understand, and can lead sometimes to strong controversy [40–42].

In 2006, Wang and co-workers presented an elegant way to obtain a metamaterial exhibiting magnetic frustration at room temperature [43]. *Artificial spin ice* mimics the spin ice pyrochlore by replacing the rare-earth ions by elongated nanomagnets on the sites of frustrated geometries such as square [43] or kagome [44] lattices. Composed of magnetic materials with in-plane anisotropy, these nanomagnets can be described to a first

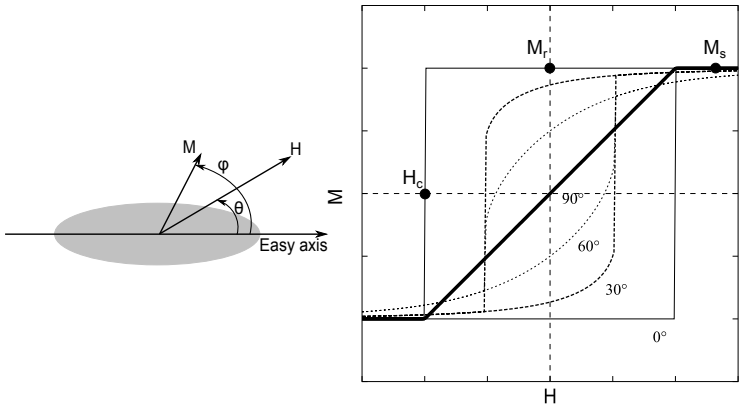


Figure 1.7: Stoner-Wohlfarth model. Evolution of the hysteresis loop as a function of φ. $\varphi = 0°$ corresponds to the magnetic field applied along the easy axis of the nanomagnet, $\varphi = 90°$ orthogonal to the easy axis. Reproduced and adapted from [48].

approximation by the Stoner-Wohlfarth model, which will be presented in the following section. They are coupled by dipolar interactions, which leads to similar ice rules as in pyrochlore spin-ice. Fabrication of artificial spin ice involves state-of-the-art lithography processes, similar to the one developed in the chapter 2. This process allows the tuning of the system properties: sizes and thickness of the nanomagnets, interaction strength and geometry. The most commonly studied geometries are square and kagome lattices, but triangular [45] or rectangular (brickwork) [46] lattices have also been investigated. More exotic arrangements have been proposed recently [47].

1.4.1 Stoner-Wohlfarth model

The individual nanomagnets can be described by the Stoner-Wohlfarth model, which is a simple model to describe the magnetization of monodomain particles [48, 49]. The total energy E_{tot} of the nanomagnet is approximated as the sum of the shape anisotropy and of the Zeeman energy. The Zeeman energy corresponds to the energy of a magnetic body with magnetization M in an external field H. The exchange energy is considered to be always optimized, hence constant, and can thus be neglected. Using the angle θ and φ defined in the figure 1.7, E_{tot} is given by:

$$E_{tot} \approx E_d + E_Z = KVsin^2(\varphi) - \mu_0 \mathbf{M} \cdot \mathbf{H} cos(\theta - \varphi) \tag{1.7}$$

with K the uniaxial anisotropy and V the volume of the particle.

The strength of this model is to predict the hysteresis as a function of φ, which represents the rotation of M away from the easy axis of the nanomagnet. It also allows one to consider the magnetization as a macrospin, thus simplifying the results [4]. We will however observe in the scattering experiments a deviation from this model in the experimental data (section 4.3.4).

1.4.2 Artificial square ice

Magnetic coupling and degeneracy in artificial square ice

The first artificial spin ice described in the literature has been the *artificial square ice* [43]. The nanomagnets are placed on the sites of a square lattice with four nanomagnets meeting

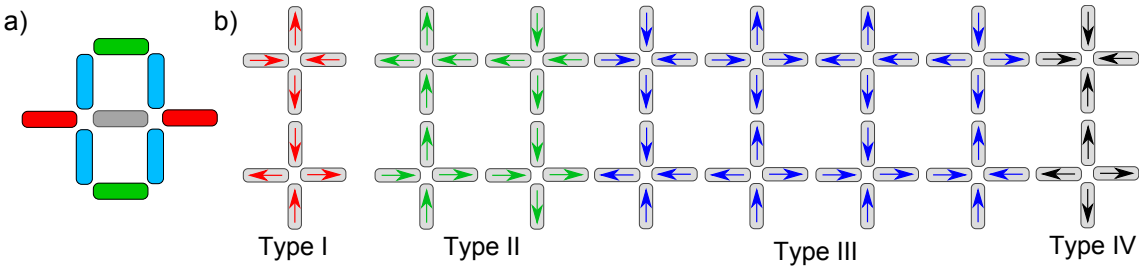


Figure 1.8: Coupled nanomagnets in artificial square ice (a) and types of vertices (b). Because of the geometry (a), the interactions are not equivalent between nanomagnets at a vertex. This leads to four energy levels, also called type (b). In order of increasing energy : type I, type II, type III and type IV vertices. Adapted from Wang *et al.* [43].

at each vertex. In contrast to magnetic pyrochlore, the interactions between the nanomagnets are not equivalent, while in a tetrahedron all spins have the same distance (figure 1.1b). In artificial square ice, we need to consider three different coupled nanomagnets: nearest-neighbours (in blue), longitudinal (in red) and transverse coupled nanomagnets (in green) (figure 1.8a) [43]. We note that a possible way to make all coupling between the nanomagnets equivalent would be to introduce a difference in height between the two sub-lattices forming the artificial square ice [50, 51], but the spins would then not meet at the same vertices [52].

Around one vertex, there are $2^4 = 16$ possibilities to arrange the spins, which correspond to four degenerated energy levels (1.8b). "Ice rules" are obeyed only by type I and type II vertices: two spins are pointing in and two spins are pointing out of the vertex, with the total magnetic charge equal to zero. In type I vertices, a "head-to-tail" arrangement of moments is found between neighbouring nanomagnets, leading to a reduction of the stray field. As a consequence, the longitudinal coupling is antiferromagnetic, which indicates the frustration of the system. It is the opposite in type II vertices: the longitudinal interaction is minimized by the ferromagnetic alignment of the nanomagnets, thus interactions between closest nanomagnets is antiferromagnetic. This explain why the type I vertices corresponds to the ground-state, as the corresponding energy is lower than the one of type II vertices.

Magnetic charges are observed in type III and type IV vertices where the ice rules are not obeyed; for example in type III vertices, three spins are pointing in and one out of the vertex, or vice-versa. This gives magnetic charges in the system (of charge $\pm$ 1 or $\pm$ 2 respectively), the charge ± 2 sometimes referred as magnetic monopoles in the literature [53].

Looking for the magnetic ground-state

One goal of the research on artificial square ice is to bring the system in its ground-state (GS), i.e. in a complete arrangement of type I vertices (figure 1.8b). Demagnetization protocols [54, 55] proved to be unable to reach a complete GS ordering starting from a saturated state. This has also been confirmed by theoretical calculations [56, 57]. Presence of defects in the lattice (*quenched disorder*) prevents the formation of the GS by pinning the magnetic moments [57]. These defects correspond to nanomagnets with different switching field due to the imperfection of the current lithography techniques.

Surprisingly, large domains of type I vertices were observed using magnetic force mi-

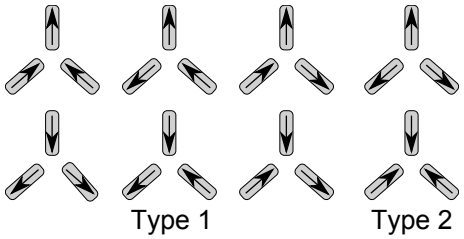


Figure 1.9: Ice rules in artificial kagome ice. In artificial kagome ice, three spins meet at one vertex. There are 8 ways to arrange the spins, which can be classified in two types. In type 1, two spins point in and one out of the vertex, or vice-versa. In type 2, all the spins are either pointing in or out of the vertex. In both cases, the magnetic charge at the vertex is not zero. Adapted from Qi *et al.* [44].

croscopy (MFM) in artificial square ice in its as-grown state [58]. Models show that thermalization occurs when the magnetic film is deposited during fabrication, with the formation of large type I domains, and type II and type III vertices acting as domain walls [59,60]. In ref. 60, Nisoli proposed to carefully control the temperature of the sample during deposition to reach the full GS ordering.

It is only recently that this full ordering has been achieved. Farhan and co-workers used nanomagnets with fluctuating moments at room temperature (superparamagnetism) [61]. After saturating the sample along the diagonal of the square lattice, they followed the relaxation process in the array with x-ray photoemission electron microscopy (PEEM). They demonstrated that the relaxation process involves two steps: the string process, creation of type I chains in a type II background. This is followed by the domain regime, the creation of large type I vertex domains separated by type II vertex domain walls. After eight hours, the sample ordered in a complete GS (see supplementary information of ref. 61).

1.4.3 Artificial kagome spin ice

From the Japanese words *kago*,"basket", and *me*,"eye" [62], the kagome lattice is the basis for a widespread organisation in minerals which leads to strong frustration in magnetic materials [1]. Placed on the site of the kagome lattice, the nanomagnets occupy the places of the rare-earth magnetic ions in the (111) plane of the pyrochlore crystals [2]. This geometry is very similar to the *honeycomb organisation*, but this latter term is usually employed when the nanomagnets are connected, forming a continuous network [63].

In contrast to artificial square ice, all interactions between the nanomagnets are equivalent as in the case of the pyrochlore spin ice. However, only three nanomagnets meet at each vertex, compared with four in the natural system. Consequently, there are $2^3 = 8$ possibilities to arrange the spins of the nanomagnets at one vertex, and these eight possibilities can be regroup in two energy levels (figure 1.9) [44]. Type 1 vertices follows the ice rules for the artificial kagome ice : two spins are pointing in and one out of each vertex, or vice-versa. Type 2 vertices have the three spins pointing either in or out of the vertex. In both cases, the magnetic charge is not equal to zero.

"Magnetic monopoles"

In type 1 vertices, the magnetic charges are $\pm 1q$ and in type 2, $\pm 3q$, with q a unit magnetic charge; they are often referred to as *emergent magnetic monopoles*. They have been

observed both in the honeycomb structure using MFM [64] and in the kagome lattice using PEEM [65]. The term monopole comes from the prediction made by Dirac of the existence of such single magnetic charges, by comparison with the single electric charge carried by electrons [66]. These Dirac monopoles are linked by a flux tube, a Dirac string, which corresponds to a singularity in the vector potential. In artificial kagome ice, these Dirac strings are formed by reversed magnetic moments in a saturated background [65]. These magnetic monopoles are not exclusive to the artificial spin ice. Indeed, their existence in spin ice has been predicted theoretically by Castelnovo and co-workers in 2008 [67] before being observed in both $Dy_2Ti_2O_7$ [68] and $Ho_2Ti_2O_7$ [32] using neutron scattering at very low temperature (close to 2 K). This provided the motivation to observe emergent magnetic monopoles in artificial spin ice. Once again, the advantage of the artificial spin ice is the possibility to work at room temperature, therefore rendering the observation much easier. Additional effort has been made to control their behaviour. By introducing islands with larger and lower anisotropy, which act as start and stop islands respectively, Hügli and co-workers have been able to control the avalanche behaviour of both monopoles and Dirac strings [69].

Impossible to reach the magnetic ground-state ?

As for the artificial square ice, scientists are interested to bring the kagome system into its GS. So far, this has not been observed. With PEEM, Mengotti [6] et *al.* and later Farhan and co-workers [70, 71] have studied the building blocks of the kagome lattice, namely the single, double and triple ring structures.

Using nanomagnets with static moments, Mengotti showed that the energy landscape grows dramatically when the number of rings increases [6]; from 2^6 states for one ring, 2^{15} states exist for three rings. In addition, increasing the system size diminished the probability to reach its GS; starting from a saturated state and using a rotating decreasing magnetic field, the frequency of GS is close to 100 % for one ring, while it only reaches 20 % for three rings.

Farhan *et al.* explored the energy landscape dynamically using superparamagnetic nanomagnets [70]. Defining an "hyper-cubic energy landscape" similar to the one met in protein dynamics [72], they followed the relaxation of the building blocks following saturation at room temperature. The increase in the system size is increasing the energy landscape, with the consequence of increased probability that the system is trapped in a local energy minimum.

1.4.4 Current state of research

Going thermal

Following the studies performed with the help of an external magnetic field, a recent trend in the research on artificial spin ice uses thermalization to access new magnetic states or study dynamical properties. Several methods have been proposed, some using new materials or others using the same materials as in all previous studies but with some tuning of the system properties.

In the first path, we can cite the work from Kaplaklis and co-workers who uses multilayered magnetic material to approach magnetic phase transitions [73]. In their work, they used δ-doped Fe(Pd) nanomagnets with a lower Curie temperature compared to Permalloy. While changing the sample temperature, they performed Magneto-optic Kerr effect measurements and compared the evolution of the magnetization with numerical simulations

to conclude about the magnetic phase of the system. Another work carried out by Porro and colleagues [74] uses NiFe alloy differing from the Permalloy composition ($Ni_{80}Fe_{20}$) with a lower Curie temperature. This work is remarkable with regard to the fact that by using a simpler material than Kaplaklis *et al.* [73], it allows them to perform several cooling/heating experiments without degradation of the sample.

The second experimental approach commits of using the same material composition, i.e. $Ni_{80}Fe_{20}$, but changing the method of study. An example is given by the work from Peter Schiffer's group in which the artificial spin ice was heated above the Curie temperature of Permalloy before being allowed to gently cool down to room temperature [75]. With this process, they observed the nucleation of low-energy arrangement of the vortex states, and crystallites of a magnetic phase predicted theoretically [51]. Another recent example is the use of low-thickness nanomagnets which allow thermal fluctuations at room temperature [61, 70]. These works demonstrated the possibility to study the slow dynamics in artificial spin ice without requiring a change in the sample temperature but rather in the film thickness. Such experiments have uncovered the complex nature of the energy landscape in artificial kagome ice [70], or the path to the full GS ordering in artificial square ice [61]. This has provided time and spatial measurements in real space microscopy.

New geometries

Most of the experiments carried out have so far been done with the nanomagnets arranged on the sites of a square or a kagome lattice. Nevertheless, both geometries present differences from the structure of the original pyrochlore crystals. New geometries or improvement of the existing ones has been used or proposed as new paths to tune the properties of artificial spin ice.

It is out of the focus of this thesis to give an exhaustive list of the new proposed geometries. Some work has been carried on triangular spin ice [76, 77], but recent simulations shows that reaching GS ordering in this system using a magnetic field could be achieved [78]. To get closer to the properties of spin ice, i.e. four magnetic moments at the same vertex with equivalent interactions, Morrison, Nelson and Nisoli proposed several new geometries derived from the square lattice to study the frustration of the vertices [47], as well as the degeneracy of the system [79]. We shall also mention the control of magnetic reversal and domain wall motion achieved by Bhat and co-workers using an artificial quasicrystal [80].

Following the suggestion from Moeller and Moessner [50, 51], recent work added a third dimension to artificial spin ice [81]. This pioneering work is the only experimental work published in the literature so far about a three-dimensional artificial spin ice system. The neutron scattering experiments presented in this article showed strong similarities between this system and the natural rare-earth pyrochlore. This opens up possibilities to study properties of the natural system at easier accessible temperatures (section 1.3).

1.5 The place of this work

Properties of artificial spin ice have been discovered and studied using numerous real-space techniques. Amongst them are most notable microscopy techniques. Pioneering experiments employing MFM and Lorentz microscopy revealed the magnetically frustrated nature of these systems [43, 44]. Recently, the GS ordering in as-grown artificial square ice has also been observed by MFM [58, 82]. The propagation of magnetic charges, or emergent magnetic monopoles, has been observed first in artificial kagome spin ice using PEEM [65],

then in artificial square ice with Lorentz microscopy [83]. The nature of their motion has been clarified using scanning transmission x-ray microscopy (STXM) by Zeissler *et al.* [84]. When research turned towards thermally activated systems, microscopy techniques have also been mainly used. We can cite the exploration of the energy landscape studied by PEEM [70] or the observation of magnetic crystallites by MFM [75] in artificial kagome ice.

Reciprocal space techniques have also contributed significantly to our understanding of the spin ice properties. Insights in the microscopic organization of the magnetic rare-earth ions in the pyrochlore structure have been brought by neutron scattering [85]. Following their theoretical predictions [67], diffuse neutron scattering have revealed the presence of magnetic monopoles in the spin ice [32, 68]

In 2012, Morgan *et al.* reported for the first time the study of artificial square ice using Soft X-ray Resonant Magnetic Resonance (SXRMS) [86]. In their experiment carried out at the National Synchrotron Light Source, they used a photodiode to acquire hysteresis loops on specular at different Bragg peaks and were able to determine qualitatively the contribution of the two sub-lattices to each hysteresis loop despite the limited amount of reciprocal space sampled.

In the present work, we applied SXRMS to investigate the magnetic behaviour of artificial spin ice but, in order to obtain a more detailed insight into the field dependence of the different Bragg peaks, we used a charged-coupled device (CCD) detector [9]. The extended observation of the reciprocal space allowed us to identify Bragg peaks arising from the magnetic arrangement in the system, as well as diffuse scattering related to the establishment of correlation. Simple models allowed us to interpret qualitatively the scattering patterns and its evolution as a function of an applied magnetic field. We also could quantify the magnetic state in the simple cases. The length and time scales available with SXRMS also allow us to get access to information not available by microscopic techniques; this is particularly true for the study of paramagnetic nanomagnets at different temperature range, experiments which would be much more difficult, or impossible, by other means. Finally, this technique is also one of the few which can be applied in the presence of a magnetic field and/or at very low temperature.

Chapter 2

Fabrication

Contents

2.1 Introduction 32
2.2 First step: spin-coating 34
2.3 Second step: electron-beam writing 35
2.3.1 Introduction 35
2.3.2 Sequence file 37
2.3.3 Shape correction 37
2.3.4 Development 38
2.4 Third step: deposition of the magnetic material 39
2.4.1 Metal evaporation 39
2.5 Final step: Lift-off 39
2.6 Thin film characterization 40
2.6.1 Film thickness 40
2.6.2 Structural characterization 40
2.6.3 Magnetic characterization 41
2.7 Summary 42

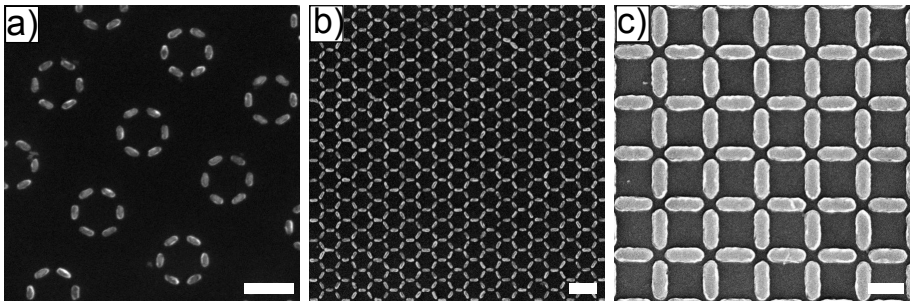


Figure 2.1: Artificial spin ice structures produced by electron-beam lithography. Single rings and infinite (a) kagome (b) and square artificial spin ice (c) structures. For a) and b), the island length and width are 60 nm and 20 nm respectively, for c) they are 470 nm and 80 nm. All islands are composed of 15 nm Permalloy ($Ni_{80}Fe_{20}$) capped by 5 nm aluminium to prevent oxidation. The scale bar (in white) represents 200 nm in all cases.

As mentioned in the previous chapter, artificial spin ice is produced using electron-beam lithography (figure 2.1) [6, 43]. This process shown consists typically of five steps (figure 2.2), but parameters can vary between research groups. First, a resist is *spin-coated* on a substrate. Then an electron beam is used to write a pattern in this polymer layer (*exposure*). After, the step of *development* dissolves away either the exposed or the unexposed areas using chemicals. Materials are thereafter *deposited* on the sample via thermal evaporation. In the final step, the structured resist and metals are removed during the *lift-off*.

Most of these steps are carried out in a clean-room which provides a particle-reduced environment, as well as a controlled atmosphere (temperature, humidity, air flow). They are very often used in the semi-conductor industry, where the size of particles such as human hair (around 50 μm) are larger than the size of the manufactured objects (below 10 μm). All the work presented in this chapter has been carried using the clean-room facilities of the Laboratory for Micro- and Nanotechnology (LMN) at the Paul Scherrer Institut. [1]

After a general introduction of lithography, we address in more detail the different fabrication steps. The last section of this chapter is also dedicated to the characterization (both structural and magnetic) of the metallic thin films. Characterization of the artificial spin ice magnetic properties is presented in section 4.1.1. All the experimental parameters can be found in appendix A which also presents the structures that can be realized with the process described in this chapter.

2.1 Introduction

Coming from the Greek words *lithos* (stone) and *graphien* (to write), lithography is a technique to transfer a pattern on a substrate. Since the process is not destructive for the main copy of the pattern, it can be repeated over and over again. Therefore, it is an easy way to repeat an image over time. Since its invention by Alois Senefelder at the end of the 18^{th} century [87], numerous developments led lithography to become a top-down fabrication of nano-objects. There are many fields of application, the semi-conductor industry certainly the most important one where lithography processes are used to produce smaller and smaller electronic compounds [88].

[1] An overview of the facilities is available at: http://www.psi.ch/lmn/facilities-and-equipment

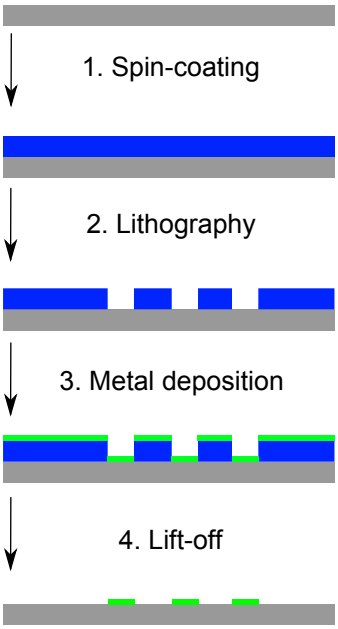


Figure 2.2: Fabrication steps. The fabrication process consists of four steps: spin-coating of the resist, lithography (electron-beam writing and development), metal deposition and lift-off. In the figure, the substrate is in grey, the resist in blue and the metal in green.

To tranfer the pattern onto a substrate, it needs to be covered with a thin film referred to as resist. Originally wax or arabic gum, nowadays mostly polymers are used, since the progress in polymer science enabled materials with high-resolution. We can distinguished two categories of resist, depending of their behaviour when exposed to a particle beam:

- Positive tone resist: the resist undergoes chain scission due to the interaction with the electron beam. The exposed area is subsequently removed using chemicals (*developers*) during the development step while the non-exposed area is not affected.
- Negative tone resist: the interaction between the beam and the resist leads to cross-links between the chains of the polymer. When developing the sample, the non-exposed area is removed by the developer but not the exposed area.

We note that some lithography techniques do not require resist. In these cases, the pattern transfer is performed by others means such as depositing materials through a shadow mask (stencil lithography) or by using pre-patterned substrates.

To expose the pattern into the resist layer, photons or electrons beams are typically used. The theoretical resolution limit is set by the wavelength, but one should consider additional consideration such as the resolution of the resist. The following four techniques are most commonly used:

- Optical (ultra-violet) lithography
- Laser interference lithography
- X-ray/extreme-ultraviolet interference lithography
- Electron-beam lithography

The last one, also referred to as *e-beam lithography*, allows the creation of features down to a few nanometres. We note that 10 nm is the resolution limit of the e-beam writer operated at 100 kV at the LMN [89].

After development, the transfer of the pattern to a material of choice can be performed in the following ways:

- Metal deposition: either evaporated or sputtered, the material is deposited as a thin film on both the resist and the substrate. In a final step, the resist is removed with a chemical during lift-off, dissolving off the unwanted resist along with the metal.

- Etching: either dry (physical) or wet (chemical), the resist is used as an etch mask and parts of the thin film are then removed. The resist is subsequently removed.

2.2 First step: spin-coating

Spin-coating is a standard process to form homogeneous thin films of a resist on a substrate. It involves the following steps; first, an excess of a solution containing a solvent and a resist with a photon- or an electron-sensitive component is deposited on the substrate. Then, the substrate is rotated at high speed. During the spinning, the solvent both evaporates, due to its low vapour pressure, and spins off the substrate, due to the centrifugal force. Varying in the spinning speed and acceleration gives different thicknesses [90]. The substrate is eventually baked to remove the rest of the solvent and to allow homogenization of the resist film.

Amongst all the available resists for e-beam lithography, we chose to use polymethylmethacrylate (PMMA), a high-resolution positive tone resist [91, 92]. It is a simple resist to handle thanks to its physical and chemical stability. We used two PMMA polymers, differing in their molecular weight: 70.000 g.mol^{-1} (70K) and 950.000 g.mol^{-1} (950 K). We decided to use these resists due to issues met during the development of the fabrication process. In particular, the lift-off (last step) proved not to be possible with the 70K resist as we will describe in section 2.5 (figure 2.3). Nevertheless, the smaller the molecular weight, the higher the sensitivity of the resist and the lower the resolution. A resist with a low molecular weight is more sensitive to the variation of the dose (the electric charge per square centimetre at the surface of the substrate). It has a lowest resolution than a resist with a high molecular mass. So, we needed to reach the best compromise between resolution and possibility to finish the lift-off (figure 2.3).

The deposition of the metal is a critical step, which also influences the choice of the resist. A rule of thumb about the deposited thickness is that it should be lower than half the thickness of the resist film. High molecular mass resists form rather thick layers (from 80 to 100 nm for low and medium spinning speed) whereas resists with a low mass form thinner films (from 10 to 20 nm) [90].

Temperature of deposition is an important parameter, as high temperature can degrade the resists and strongly hinder the lift-off. The deposition is the final step to take into account in the choice of a resist. The higher the molecular mass of a polymer is, the lower is its solubility [93].

After a series of trials and adjustments, we settled on use the following parameters:

- 20 nm PMMA (50K) and 70 nm PMMA (950K)

- 70 nm PMMA (950k)

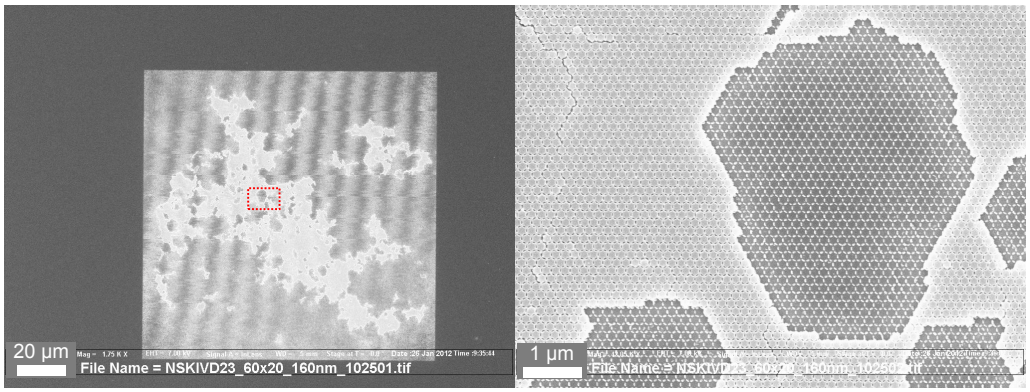


Figure 2.3: Failed lift-off. We present the case of an array of $50\mu m \times 50\mu m$ composed of nanomagnets with length $60nm$ and width $20nm$ for which the lift-off was not possible. We used a 70 nm PMMA layer as resist. Due to the high temperature during evaporation, the resist degrades and cannot eventually be removed from the surface of the substrate. The right panel corresponds to the area highlighted by a red square in the left panel.

The first one has been developed in the original fabrication process. The lower layer (PMMA 50K) is used to improve the lift-off, even when high temperatures are reached during deposition of the magnetic material. However, it limits the resolution because of its higher sensitivity to the electron beam. It is also not straightforward to use, as the same solvent is used for both layers. Consequently, it requires a quick process to deposit the second layer before degradation of the first layer.

The second recipe is now used since the availability of a water-cooled sample holder for the thermal evaporator (section 2.4.1), which prevents strong degradation of the resist layer due to high temperature (figure 2.3). It also improves the resolution compared to the original process.

2.3 Second step: electron-beam writing

2.3.1 Introduction

The key advantage of electron-beam lithography is the high-resolution thanks to the small wavelength of the electrons. Consequently, it is always used due to this advantage which balances the low writing speed. Amongst applications, we can cite the production of the masks used in photolithography or the fabrication of very small objects for research purposes [94].

Electron beam writer

The electron-beam writer Vistec EPBG 5000 Plus installed at the *Laboratory for Micro- and Nanotechnology* offers an ultimate resolution of sub-10 nm thanks to its 100 kV electron beam [89]. The key elements of the instrument are presented in the figure 2.4. Extracted from a tungsten wire coated with zirconium oxide, the electron beam is accelerated to an energy of 100 keV in the extractor. The focusing of the beam is obtained using three lenses, one electrostatic prior to the anode and two magnetic prior to the beam blanker and the exit of the column respectively. The beam blanker allows the deflection of the beam by application of a voltage, turning the beam on and off. It thus allow the writing of the structures. The aperture allows the control of the beam spot size and of the current

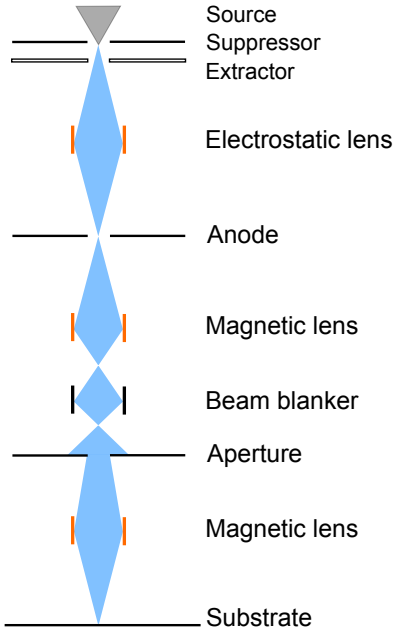


Figure 2.4: Simplified schematic of an electron-beam writer.

at the surface of the substrate. During exposure, the sample needs to be grounded either by use of a conductive substrate or by the deposition of a thin metallic film on top of an insulating substrate.

Proximity effect

Apart from the direct interaction between the electron beam and the resist, one should consider two secondary scattering events, often referred as called *proximity effect* [95]. Both types of secondary scattering of the electrons leads to a broadening of the exposed area.

Forward scattering occurs when the beam enters resist and substrate; electrons undergo collision with the electrons of the atoms and are scattered at a small angle. Figure 2.5 reproduces the trajectories of the electrons as obtained by Monte-Carlo simulations using the CASINO software [96]. We performed them for two beam currents, 20 kV and 100 kV respectively. One observes that increasing the beam voltage leads to a decrease in the forward scattering. In addition, at low beam voltage, thin resist layers help to improve the resolution as the scattering increases with the resist thickness.

One also notes that at low voltage (figure 2.5b), the electrons scatter more in the substrate where they undergo a second elastic scattering by the atoms of the substrate. This is the *backward scattering*. The differential scattering cross-section is proportional to the square of the atomic number Z [97]. Since Z is larger for the silicon substrate than for the resist (usually carbon chains), it originates mainly from the substrate and increases the effective dose received by the resist in a large area.

Taking the proximity effect into account is necessary to achieve small objects. Several proximity effect correction methods exist which can be based on computation (dose modulation [98, 99]) or be purely empirical.

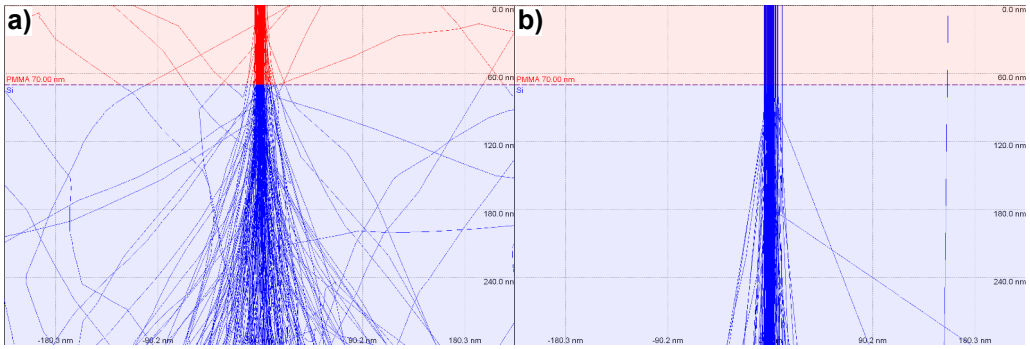


Figure 2.5: Electron trajectories in the case of forward scattering calculated by Monte-Carlo method. We considered a 70 nm-thick PMMA layer (red area) on top of a silicone (100) substrate (blue area). Beam acceleration voltages are a) 20 kV and b) 100 kV. Simulations performed using the Casino software [96].

2.3.2 Sequence file

The classical way to write a pattern is to fracture it in smaller geometrical shapes such as trapezoid, which are approximating as close as possible the original pattern. An illustration is given in the figure 2.6a. A nanomagnet of size 470 nm by 160 nm in length and width has been fractured using an algorithm existing in the software Layout Beamer from GenIsys [100]. This method generates an important amount of data which can saturate the pattern generator from an e-beam writer. It is thus not possible to use this method when the structure needs to be repeated a significant amount of times.

To address this issue, we used the sequence language developed by the company Vistec. This programming language is very rich and offers a lot of possibilities, therefore we will limit ourselves here to its basics. The idea behind this language is to offer a full control of the beam and its options, and to allow the exposure of a pattern pixel-by-pixel. The first consequence is the fine tuning of a shape compared to a fracturation (figure 2.6b). Moreover for a periodic pattern such as artificial spin ice, it allows the definition of a unit cell which will be repeated over large areas. This leads to a strong reduction in both the amount of data and exposure time because the electron beam is controlled precisely and does not approximate geometrical shapes. Nanomagnets similar to the ones in figure 2.1b can be produce over areas as large as 5 by 5 mm^2 in less than 8 hours. No stability issue in the writing process has been observed during this time.

2.3.3 Shape correction

The versatility of the lithography process allows to produce from large (100 microns range) to very small (sub-50 nm) objects (examples given in annex A). All cases show approximately the same uncertainties. For example, the variations in length, Δl, and in width, Δw, of the nanomagnets are typically 2 nm and 5 nm, respectively. While for large nanomagnets (230 $\times$ 80 nm^2), Δl and Δw represent variations of 0.8 % and 5 % in length and width, this is a variation of 5 % and 33 % in the case of the smallest nanomagnets (40 $\times$ 15 nm^2).

There are approaches to take into account these variations. In our case, we reach the desired dimensions by reducing the size of the nanomagnets in the files we are using for e-beam exposure and by increasing the applied dose. This is often referred to as the *undercut-overexposed* strategy. For example, to obtain nanomagnets with size of 60 nm $\times$

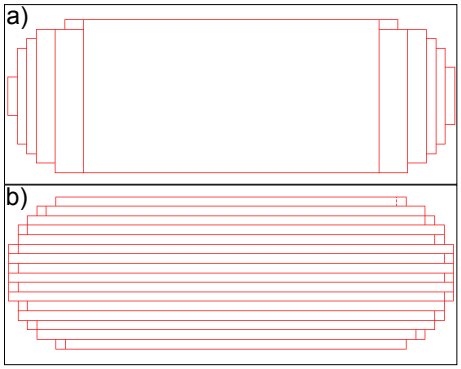


Figure 2.6: Exposure pattern. An island of dimension 470 nm by 160 nm in length and width respectively is obtained by a) use of an algorithm and b) sequence programming as described in the text.

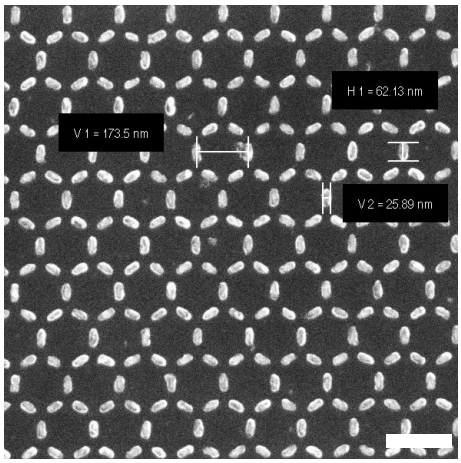


Figure 2.7: Observation of proximity effect in an artificial kagome spin ice. In the design, all the nanomagnets are identical and of size 60 nm × 20 nm in length and width respectively. In reality, perfect reproducibility cannot be achieved due to parameters such as the proximity effect (forward and backward scattering of the electron beam in the resist and substrate). The scale bar (in white) represents 200 nm.

20 nm in length and width (figure 2.1b), respectively, we have aimed for nanomagnets of 65 nm × 15 nm with a dose of 1200 μC/cm^2 instead of 1000 μC/cm^2 as usually used.

To conclude this section, we note that controlling the size of the nanomagnets is easier than controlling their shapes. This is due to the stochastic nature of the secondary scattering processes. The distribution of shapes and sizes in an array leads to a distribution of the coercitivy. One notes that this can give rise to unexpected effects. For example, it is the origin of the quenched disorder responsible for the avalanche behaviour of the magnetization reversal in artificial spin ice [69].

2.3.4 Development

After exposure, the sample is immersed in a chemical, called developer, which allows the removal of exposed or non-exposed areas depending on the resist. Duration and temperature of this step as well as composition of the developer are important parameters of the development step [101].

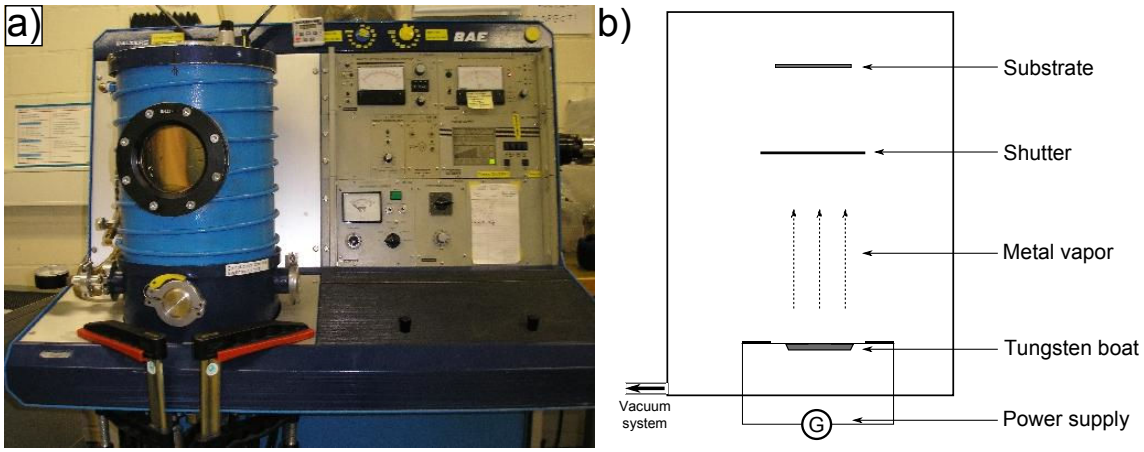


Figure 2.8: Metal evaporation. a) Balzers BAE 250 evaporator installed at the LMN. The blue tank is the deposition chamber (b). Materials are put in a boat which is heated by applying a current (Joule Effect). Above the boiling point, significant evaporation of the material occurs and the evaporated atoms condensate on the sample.

We used a mix of methyl isobutyl ketone and isopropanol with a ratio of 1:3 to develop our samples. This is the standard process used at the LMN for this type of samples. We note that improvements could be obtained by using other developers such as a mix between isopropanol and water [102, 103].

2.4 Third step: deposition of the magnetic material

2.4.1 Metal evaporation

We deposited the magnetic materials by thermal evaporation (figure 2.8). This is a rather simple technique to use: pellets of a material are deposited in a boat which is heated with a current. Once the boiling temperature of the material is reached, significant evaporation takes place and the atoms condense on the substrate. This is performed at a base pressure of 10^{-7} mbar to prevent formation of metal oxides.

In this thesis, we routinely evaporated in-plane magnetic materials such as Permalloy ($Ni_{80}Fe_{20}$), always capped by a thin aluminium layer (around 5 nm) to prevent oxidation of the sample. To obtain the correct composition of the Permalloy, we used FeNi pellets enriched in Ni ($Ni_{81}Fe_{19}$) [104, 105]. The samples were also water-cooled during the deposition, to lower their temperature and prevent the degradation of the resist during deposition, as already mentioned (figure 2.3).

One drawback of this method is the formation of an alloy the boat material [106]. Energy-dispersive x-ray (EDX) analysis showed no significant traces of tungsten in the deposited thin magnetic films.

2.5 Final step: Lift-off

The lift-off is the last step of the fabrication process. It involves the use of chemicals to remove all the unwanted metal and resist from the sample, therefore leaving only the nanostructures on the substrate.

To remove the PMMA layer, we used acetone as solvent in combination with ultrasound in a sonic bath. We took also into account the dependence with temperature of the

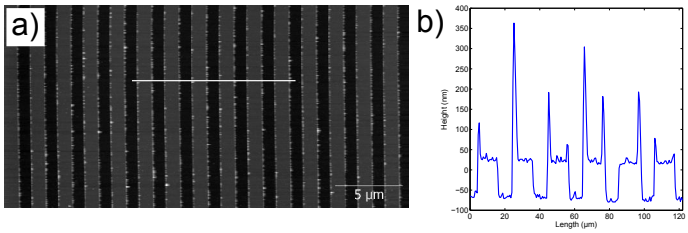


Figure 2.9: AFM characterization of a Permalloy thin film. a) AFM picture of a line gratings used to determine the exact deposited thickness. b) Profile extracted from the white line in picture a). The irregularities in the profile at the beginning and end of each line is a lift-off edge, rest of metal stuck on the edges of the lines.

solubility of PMMA to speed up the lift-off process to prevent significant oxidation of the nanomagnets [93, 107]. For example, the lift-off of nanomagnets as small as 60 nm × 20 nm (figure 2.1b) over 1 mm^2 takes more than 1 hour at room temperature, but less than 45 minutes at 50°C. We also tested other solvents such as N-methyl-2-pyrrolidone or dimethyl sulfoxide, but none brought significant improvements compared to acetone. Once the resist and metal are removed, the samples were rinced with isopropanol. In addition, in order to limit contamination with particles, all the solvents were high-purity CMOS (Complementary Metal Oxide Semiconductors). Following lift-off, the samples were stored in a vacuum desiccator.

2.6 Thin film characterization

2.6.1 Film thickness

The deposition rate is monitored by a quartz balance inside the chamber. This is a rather inaccurate method to measure thickness of the deposited film. We deposited in parallel a grating at the same time (figure 2.9a). This sample also produced by lithography allows us to measure the deposited thickness using an atomic force microscope (AFM). The AFM profile shown in figure 2.9b has been obtained from a grating for which 100 nm of Permalloy were deposited.

We observe that the profile is not regular and has jumps at the beginning and at the end of most of the grating lines. These are the so-called "lift-off" edges, i.e. part of the resists which remains on the sample after the lift-off. It is usually not problematic when scattering experiments are performed in transmission, but it may cause problems when measuring in reflection as we did. As we describe in section 4.3.4, these edge can be an explanation for the discrepancies between experimental results and numerical simulation, as they are not taken into account in the models.

2.6.2 Structural characterization

We characterized the film structure with transmission electron microscopy (TEM) using a Tecnai F30ST microscope located at the *Electron Microscopy* of the *ETH Zürich* laboratory. The films had same composition and thickness as the one used for our artificial spin ice samples: 20 nm thick Permalloy layer, capped by a 5 nm thick aluminium layer. To perform a complete characterization, films were deposited on both Si_3N_4 membranes and Si substrates.

We present in figure 2.10 a cross-section view of the thin film deposited on Si. One can

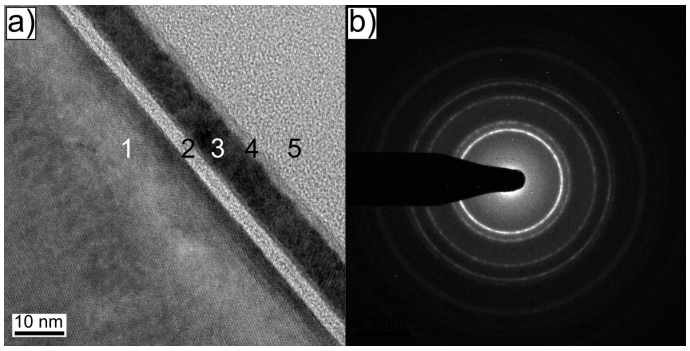


Figure 2.10: Cross-section and diffraction pattern of a Permalloy thin film. a) Cross-section high-resolution transmission electron microscopy (HRTEM) picture : 1. Si substrate, 2. SiO_2, 3. Permalloy ($Ni_{80}Fe_{20}$), 4. aluminium, 5. adhesive layer used for crossed-section imaging. b)Electron diffraction pattern recorded in the Permalloy layer presenting Bragg rings.

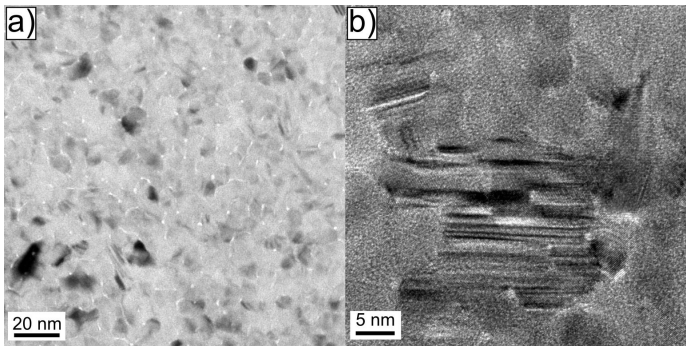


Figure 2.11: Defects in a Permalloy thin films. a) Grain boundaries (white spots) observed in TEM. b) Twinning defects in the crystal order observed in HRTEM.

observe the crystalline plane in the Si substrate (layer 1); on the other hand, no crystalline plane is observed for the Permalloy layer (layer 3). We performed electron diffraction on the layer 3, and the diffraction pattern (figure 2.10b) exhibits Bragg rings instead of Bragg peaks. This demonstrate that the Permalloy deposited with thermal evaporation is polycrystalline. Additional measurements have been carried on a film deposited on a Si_3N_4 membrane. In the panel a of the figure 2.11, one observes several grain boundaries in the material. Crystalline defects such as twinning crystals are present in the material (figure 2.11b).

As described in the previous section, materials can form alloys with the boat used for evaporation. Iron and nickel are known to form alloys with tungsten [106], so we performed EDX measurements to evaluate the formation of alloys. We use energy-dispersive x-rays (EDX) measurement to evaluate the contamination rate of the magnetic film with tungsten (figure 2.12). As observed in the figure, there is no strong signal coming from tungsten in the EDX spectrum. At the same time, presence of nickel and iron is confirmed in the film.

2.6.3 Magnetic characterization

Magnetic characterization were performed on a 20 nm thick Permalloy film using the magneto-optic kerr effect (MOKE) set-up of the *SIM Beamline* at the *Swiss Light Source*. The set-up was configured for longitudinal MOKE, i.e. the detection of the in-plane com-

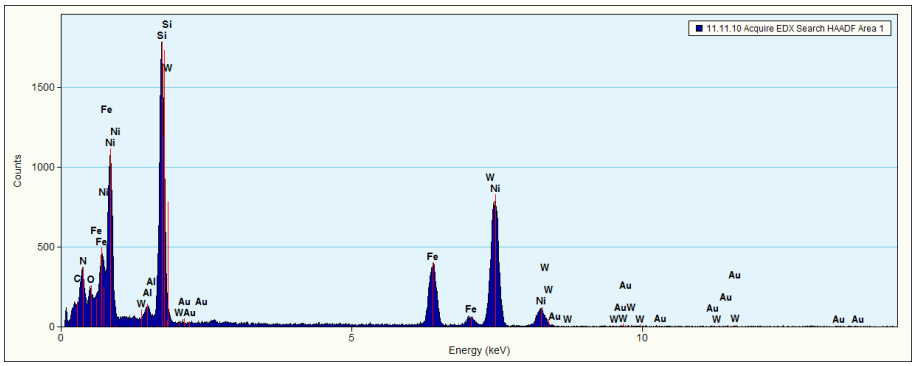


Figure 2.12: EDX spectrum of a Permalloy thin films. No significant tungsten signal is observed in the spectrum, indicating a low contamination rate of the film.

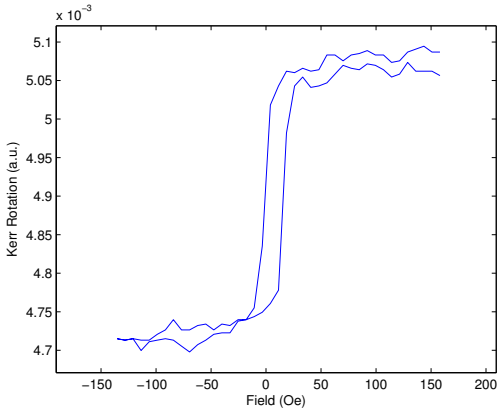


Figure 2.13: Hysteresis loop of a Permalloy thin film. Recorded by MOKE; it exhibits the character of a soft magnetic material, as one would expect from a Permalloy thin film.

ponent of the magnetization. Indeed, the thin films exhibit a hysteresis loop, typical for a soft magnetic material (figure 2.13).

To conclude this section, we have observed that our Permalloy thin films are polycrystalline when deposited with thermal evaporation. Nevertheless, this composition do not alter the magnetic properties of the film which still present an in-plane magnetization.

2.7 Summary

In this chapter, we have presented the fabrication process which has been developed to produce the artificial spin ice samples.

We remark that the final lift-off proved to be the most critical step of the overall process. Choices of resist and temperature of metal deposition showed direct effect on the speed of the lift-off. We have presented the strategy we used in the choice of the resist, especially the effect of low-molecular weight resists in the fabrication, with an increase in lift-off speed but a decrease in the resolution. Water-cooling of the sample during metal deposition improved the process by decreasing the damage of the resist due to high temperature.

Chapter 3

Photon-matter interactions

Contents

3.1 Absorption and resonant scattering of x-rays 44
3.1.1 Absorption and Magnetic Circular Dichroism 44
3.1.2 Resonant magnetic x-ray scattering 47
3.2 Measuring in reciprocal space 51
3.2.1 Unit cell 52
3.2.2 Bragg diffraction 52
3.2.3 Ewald's construction 54

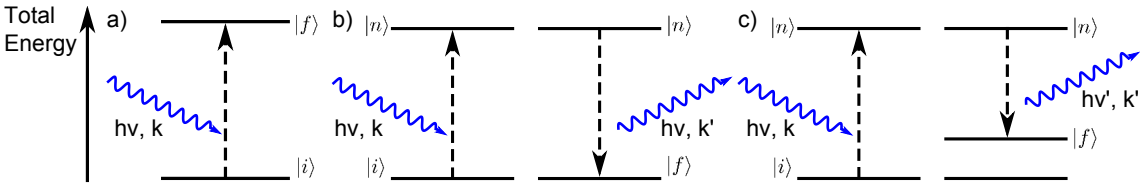


Figure 3.1: Resonant photon-in photon-out processes. a) Absorption, b) elastic scattering and c) inelastic scattering.

Following fabrication, we used the samples of artificial spin ice to perform soft x-ray magnetic scattering. Before going into the details of these experiments, we now remind the basics of x-ray - matter interactions. Our goal here is not to give a complete description of the physics, which can be already found in reference textbooks [108–110].

We have divided this chapter in two sections. The first one is devoted to the interactions between photons and electrons. Absorption is introduced with the principal equations of the quantum physics; the particular case of absorption of polarized x-rays by magnetic materials is treated, an effect called x-ray magnetic circular dichroïsm. We go one step further with the description of the resonant scattering mechanism. A special emphasis is brought on the sensitivity to magnetism.

The second section introduces the notion of reciprocal space. Indeed, scattering measurements are carried out in this space, which corresponds to the Fourier Transform of the real space. We introduce the few notions of crystallography required such as the definition of unit cells and Bragg's law. We also present the concept of the Ewald's construction. More than a "simple" representation, it is observed in the experimental results presented in the next chapter.

3.1 Absorption and resonant scattering of x-rays

Since the pioneering work from de Bergevin and Brunel on two antiferromagnets (NiO and Fe_2O_3) in 1981 [111–113], x-ray scattering became a tool to study magnetic materials due to the development of third-generation light sources. They provide high brilliance photon fluxes with a tunable energy, therefore allowing the probing of different elements in materials.

Resonant scattering is a photon-in photon-out process (figure 3.1): following the absorption of a photon, a second photon is emitted with either the same (elastic) or a different energy (inelastic). In both cases, the wavevector $\mathbf{k}$ due to a transfer of the momentum to the electronic system. Measurement of the variation of the wavevector, $\mathbf{q} = \mathbf{k'} - \mathbf{k}$ with q the *momentum transfer*, brings information about the structure of the system such as the crystallinity, the shape or the presence of magnetic correlations.

X-rays are chemical sensitive probes which can be tuned to match the incident photon energy with exact difference between two energy levels (*absorption edge* or *resonance*). Such properties are not available for other probes such as neutrons or muons. In $3d$ magnetic transition metals such as Fe, Co or Ni, the L_3 absorption edge is located in the 700 - 800 eV range. Exciting the system with soft x-rays thus allows the study of their magnetic properties ($2p \rightarrow 3d$ transitions). In addition, the possibility to change the polarization of the photon allows the study of magnetism through the x-ray magnetic circular dichroism (XMCD) [13, 114–116].

Following the discovery of the resonant scattering and, at the same time, of the sensitivity of scattering to magnetism [117–120], soft x-ray resonant scattering became a standard technique to study a broad range of materials: magnetic multilayers [121, 122], coupled nanowires [10], spin-valves [11] or sub-micron patterned films [12].

3.1.1 Absorption and Magnetic Circular Dichroism

X-Ray Absorption Spectroscopy

Absorption is the transfer of the energy and momentum of a photon to an electron (figure 3.1 a). This happens at specific energy value, which corresponds to the *absorption edge*

(or resonance) of an element [109]. These edges vary from element to element, making the photon a chemically sensitive probe. These values are known and tabulated [123].

The experiments reported here were carried out in the soft x-ray photon range; this energy range covers the $2p \rightarrow 3d$ ($L_{2,3}$) edge of $3d$ transition metals Co,Fe,Ni and the $5d \rightarrow 4f$ ($M_{4,5}$) of $4f$ edge rare-earth, e.g. Sm or Gd.

In the following, we will briefly discuss x-ray absorption using a quantum mechanics approach. This discussion follows the approach of the book by Altarelli in ref. 108. In particular, our interest will be the establishment of the Hamiltonian of the system, and the expression of the transition rate within the perturbation theory, which we will compare later with its expression in the case of scattering.

The total Hamiltonian H_{tot} is the sum of two Hamiltonians, H_{el} which describes the electrons and H_{rad} for the photons:

$$H_{tot} = H_{el} + H_{rad} \tag{3.1}$$

H_{el} is given by:

$$H_{el} = \sum_i \left(\frac{\mathbf{p}_i^2}{2m} + V(\mathbf{r}_i) \right) \tag{3.2}$$

$\mathbf{p}$ is the momentum operator and m the electron rest mass. $V(\mathbf{r}_i)$ is the potential energy which in the case of a system with N electrons:

$$V(\mathbf{r}_1, ..., \mathbf{r}_n) = \sum_{i=1}^{N} V_{nuc}(\mathbf{r}_i) + \sum_{i>j} V_C(|\mathbf{r}_i - \mathbf{r}_j|) \tag{3.3}$$

where V_{nuc} describes the coulombic interaction of all electron with the nucleus and V_C the coulombic repulsion between electrons. This expression can be simplified to a one-electron system by considering the behaviour of one electron in an averaged field through the *self-consistent field approximation* [108]:

$$V(\mathbf{r}_1, ..., \mathbf{r}_n) \simeq \sum_{i=1}^{N} V(\mathbf{r}_i) \tag{3.4}$$

In the presence of an electro-magnetic field, the momentum of the electrons changes. To take this into account, we replace $\mathbf{p}_i$ by $\mathbf{p}_i - (e/c)\mathbf{A}$:

$$H_{el} = \sum_{i=1}^{N} \left(\frac{\mathbf{p}_i^2}{2m} - \frac{e}{mc}\mathbf{A} \cdot \mathbf{p}_i + \frac{e^2}{2mc^2}\mathbf{A}^2 + V(\mathbf{r}_i) \right) \tag{3.5}$$

where $\mathbf{A}(\mathbf{r}_i)$ is the vector potential [108]:

$$A(\mathbf{r}, t) = \sum_{\mathbf{k},\lambda} \left(\frac{hc^2}{\Omega w_{\mathbf{k}}} \right)^{1/2} \left[\mathbf{e}_\lambda(\mathbf{k}) a(\mathbf{k}, \lambda) e^{i(\mathbf{k}\cdot\mathbf{r} - w_{\mathbf{k}}t)} + \mathbf{e}_\lambda^*(\mathbf{k}) a^\dagger(\mathbf{k}, \lambda) e^{-i(\mathbf{k}\cdot\mathbf{r} - w_{\mathbf{k}}t)} \right] \tag{3.6}$$

with h the Planck constant, $\mathbf{e}$ polarization vector of the mode λ, Ω volume of the quantization box and $w_{\mathbf{k}} = c|\mathbf{k}|$.

$a(\mathbf{k}, \lambda)$ and $a^\dagger(\mathbf{k}, \lambda)$ are the operators of *annihilation* and *creation* of a photon which are also used to write the Hamiltonian related to the electro-magnetic field [108]:

$$H_{rad} = \sum_{\mathbf{k},\lambda} \hbar\omega_{\mathbf{k}} (a(\mathbf{k}, \lambda) a^\dagger(\mathbf{k}, \lambda) + 1/2) \tag{3.7}$$

The total Hamiltonian is thus given by:

$$\begin{aligned} H_{tot} &= H_{el} + H_{rad} \\ &= \sum_{i=1}^{N} \left(\frac{\mathbf{p}_i^2}{2m} - \frac{e}{mc}\mathbf{A}\cdot\mathbf{p}_i + \frac{e^2}{2mc^2}\mathbf{A}^2 + V(\mathbf{r}_i) \right) + \sum_{\mathbf{k},\lambda} \hbar\omega_{\mathbf{k}} (a(\mathbf{k},\lambda)a^\dagger(\mathbf{k},\lambda) + 1/2) \end{aligned} \tag{3.8}$$

which can be rewritten as:

$$H_{tot} = H_{el} + H_{rad} + H_{int} \tag{3.9}$$

with H_{int}, interaction Hamiltonian between photons and electrons, expressed as:

$$H_{int} = -\sum_i \frac{e}{mc}\mathbf{p}_i \cdot \mathbf{A} + \sum_i \frac{e^2}{2mc^2}\mathbf{A}^2 \tag{3.10}$$

The fist term linear in $\mathbf{A}$ corresponds to the absorption of a photon. The second one, quadratic in $\mathbf{A}$, corresponds to the *Thomson scattering*, i.e. the elastic scattering of a photon by the electronic cloud. It also corresponds to the scattering of the photon via an intermediate state, which we will describe in section 3.1.2 as resonant scattering.

In the following, we are only interested in absorption. To simplify the theoretical treatment, it is usual to use the *electric dipole approximation*. Let us consider the transition between an initial state $|i\rangle$ and a final state $|f\rangle$. As the wavelength of the photon is much larger than the size of an atom, the matrix elements which describes the transition in the first and second terms of the equation (3.10) of form $\langle f| e^{i(\mathbf{q}\cdot\mathbf{r})} |i\rangle$ can be rewritten as $\langle f| \mathbf{q}\cdot\mathbf{r} |i\rangle$ [109]. Within this approximation, the probability that a photon is absorbed is given by the absorption cross-section σ_{abs}; its expression is given in equation (9.59) in ref. 109. Using σ_{abs}, we can now write the transition rate up to the first order in the perturbation theory using the *Fermi's Golden Rule* [109]:

$$\begin{aligned} w &= \frac{2\pi}{\hbar} \left| \langle f| H'_{int} |i\rangle \right|^2 \delta(E_f - E_i) \\ &\approx \left| \langle f| \frac{e}{mc}\mathbf{p}_i \cdot \mathbf{A} |i\rangle \right| \end{aligned} \tag{3.11}$$

As a consequence of the dipole approximation, one obtains from equation 3.11 the following selection rules, written here in the case of single-electron transition [109]:

$$\Delta l = \pm 1; \Delta m_l = 0, \pm 1; \Delta s = 0; \Delta m_s = 0.$$

with l the azimuthal quantum number, m_l the magnetic quantum number, s the spin and m_s the spin projection quantum number.

X-ray Magnetic Circular Dichroism

Absorption cross-section in ferromagnetic elements does not depend only on the photon energy, but also on the polarization. This was first demonstrated by Schütz and co-workers at the Fe K-edge and was the first demonstration of the XMCD [13]. To describe this effect, we use a two-component model to the $2p \rightarrow 3d$ transition (figure 3.2) following ref. 109 and 124; the XMCD effect stays however a single step process.

In a first part, a circularly polarized photon is absorbed by an electron. Conservation of the momentum imposes the transfer of the photon momentum to the electron via spin-orbit coupling [125]; absorption of a photon alone cannot change the spin. The relative

transition probabilities are given by the *Clebsch-Gordan coefficient* [126] which take into account the photon polarization. The excitation probability will be high if they both photon and spin are parallel to each other [125]. Let us consider the case of the transition presented in figure 3.2; if the photon have a momentum of $+\hbar$ (right-handed), there will be excitation of 62.5 % of spin-up electrons at the L_3 edge and of 25 % at the L_2 edge (L_3 and L_2 have opposite spin-orbit coupling). If the photon have a momentum of $-\hbar$ (left-handed), the probability will be 37.5 % of spin-down electrons at the L_3 edge, and 75 % at the L_2 edge [109]. Without the spin-orbit coupling of the $2p$ shell, there would be no possible distinction.

The second step of the model is the transition of the excited electron to the spin-split valence band, as we have already seen in the Stoner-Slater model (section 1.2.3). This will act as a detector of the electron polarization. Indeed, if one of the bands is completely filled, then no transition will be possible and there will be a strong dichroism [126].

The XMCD effect is usually calculated as the difference between spectrum recorded with opposite helicities:

$$I_{XMCD} = I_R - I_L \tag{3.12}$$

with I_R and I_L the intensity corresponding to right and left polarization respectively (red curve in figure 3.2). More than an indication of magnetism, XMCD can be used to obtain information on the orbital and spin moments using the sum rules developed by Thole *et al.* [127] and Carra *et al.* [128].

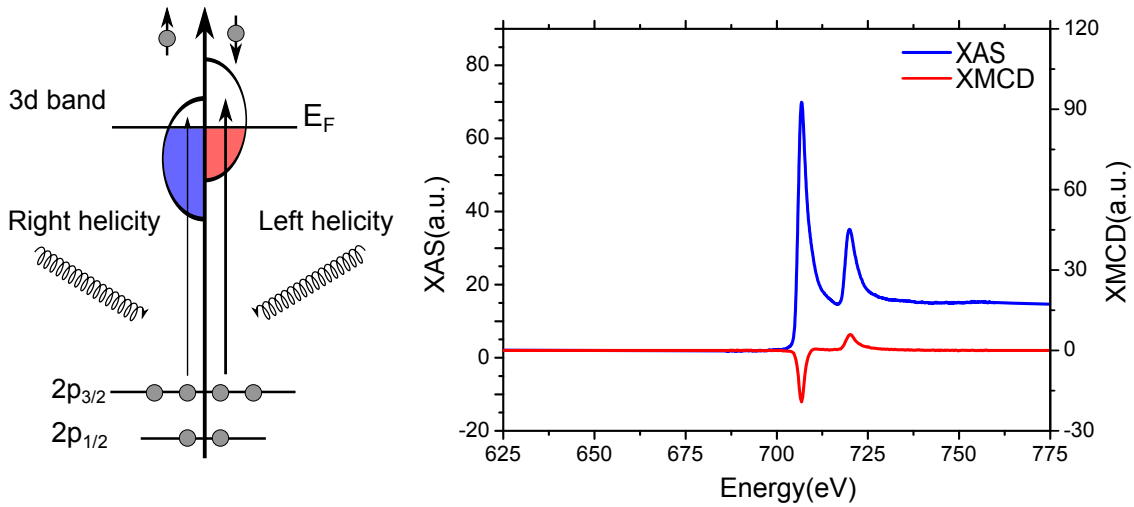


Figure 3.2: X-ray magnetic circular dichroism. On the right side is presented a x-ray absorption spectroscopy (XAS) spectrum recorded with circularly polarized photons at the Fe L-edges (blue curve) and the XMCD spectrum obtained at the same edges (red curve). XAS and XMCD data from Dr. N. Jaouen., *Synchrotron SOLEIL*.

3.1.2 Resonant magnetic x-ray scattering

We start again from the same Hamiltonian H_{tot} as used above for the description of absorption:

$$H_{tot} = H_{el} + H_{rad}$$

Historically, resonant scattering has been treated with the use of a Dirac Hamiltonian by Blume [117]. In this section, we will follow this notation, hence using a Dirac Hamiltonian, but alternative treatments can be found in ref. 129 and 130. The use of this Hamiltonian

introduces the electron spins via Dirac matrices, and also relativistic effects happening to core electrons in heavy atoms [131, 132].

Within the self-consistent field approximation (section 3.1.1), the electronic Hamiltonian H_{el} is expressed by:

$$H_{el} = \sum_{i=1}^{N} (c\boldsymbol{\alpha} \cdot \mathbf{p}_i + \beta mc^2 + V(\mathbf{r}_i)) \tag{3.13}$$

with $\mathbf{p}$ the momentum operator, m the rest mass of the electron and c the speed of light. $V(\mathbf{r}_i)$ is given in equation 3.3; α and β are the Dirac matrices with complete expressions given by Altarelli in ref. 110. As before, we take into account the interaction between electrons and photons, and thus to replace $\mathbf{p}_i$ by $\mathbf{p}_i - (e/c)\mathbf{A}$. H_{el} is then written as:

$$H_{el} = \sum_{i=1}^{N} (c\boldsymbol{\alpha} \cdot [\mathbf{p}_i - (e/c)\mathbf{A}] + \beta mc^2 + V(\mathbf{r}_i)) \tag{3.14}$$

As pointed out by Altarelli [110], the soft x-ray range is in the non-relativistic limit of the Dirac Hamiltonian, because the photon energy is very small (500 to 200 eV) compared to the electron rest energy ($\approx$ 511 keV). All the implications are given in Section 15 of ref. 133, but we will keep for our purpose only that H_{el} can be re-written under the form [110]:

$$H_{el} = \sum_{i=1}^{N} \left[\frac{[\mathbf{p}_i - (e/c)\mathbf{A}]^2}{2m} + V(\mathbf{r}_i) - (e\hbar/mc)\mathbf{s}_i \cdot \mathbf{B} - (e\hbar/2m^2c^2)\mathbf{s}_i \cdot (\mathbf{E} \times [\mathbf{p}_i - (e/c)\mathbf{A}]) \right] \tag{3.15}$$

with $\mathbf{s}$ the electron spin, $\mathbf{B}$ and $\mathbf{E}$ being the magnetic and electric field of the incident photons.

Using the expression of H_{rad} given in equation (3.7), the complete Hamiltonian describing the system is:

$$\begin{aligned} H_{tot} = & \sum_{\mathbf{k},\lambda} \hbar\omega_{\mathbf{k}} (a(\mathbf{k},\lambda)a^{\dagger}(\mathbf{k},\lambda) + 1/2) + \\ & \sum_{i=1}^{N} \left[\frac{[\mathbf{p}_i - (e/c)\mathbf{A}]^2}{2m} + V(\mathbf{r}_i) - (e\hbar/mc)\mathbf{s}_i \cdot \mathbf{B} - (e\hbar/2m^2c^2)\mathbf{s}_i \cdot (\mathbf{E} \times [\mathbf{p}_i - (e/c)\mathbf{A}]) \right] \end{aligned} \tag{3.16}$$

Following the treatment from ref. 108, we can write H_{tot} as the sum of three Hamiltonians:

$$H_{tot} = H'_{el} + H'_{rad} + H'_{int} \tag{3.17}$$

H'_{el} and H'_{rad} are describing the electronic cloud and the electro-magnetic field respectively, and H'_{int} the interactions between the two systems [117]. H'_{int} is expressed as the sum of four independent Hamiltonians:

$$H'_{int} = H'_1 + H'_2 + H'_3 + H'_4 \tag{3.18}$$

The complete expressions of H'_1, H'_2, H'_3 and H'_4 can be found in ref. 117 and 110. For the following, we only consider the dependency of each term with $\mathbf{A}$, i.e. H'_1 and H'_4 being quadratic in $\mathbf{A}$, and H'_2 and H'_3 being linear.

Resonant scattering is a second order process (figure 3.1b and c). The transition rate is obtained by extending the Fermi's Golden Rule to the second order, which is also known as the *Kramers-Heisenberg equation* [134]:

$$w = \frac{2\pi}{\hbar} \left| \langle f | H'_{int} | i \rangle + \sum_n \frac{\langle f | H'_{int} | n \rangle \langle n | H'_{int} | i \rangle}{E_i - E_n + i\Gamma} \right|^2 \delta(E_f - E_i) \tag{3.19}$$

$|n\rangle$ is a virtual state in the scattering process with a lifetime of Γ. The elastic case implies $|i\rangle = |f\rangle = |0\rangle$ (figure 3.1b), therefore by introducing equation (3.18), equation (3.19) can be rewritten as:

$$w = \frac{2\pi}{\hbar} \left| \langle 0 | H'_1 + H'_4 | 0 \rangle + \sum_n \frac{\langle 0 | H'_2 + H'_3 | n \rangle \langle n | H'_2 + H'_3 | 0 \rangle}{E_0 + \hbar\omega_{\mathbf{k}} - E_n + i\Gamma} \right|^2 \tag{3.20}$$

with $E_i = E_0 + \hbar\omega_{\mathbf{k}}$, E_0 being the energy of the state $|0\rangle$ and $\hbar\omega_{\mathbf{k}}$ the difference in energy between $|0\rangle$ and $|n\rangle$. Equation 3.20 is a general equation which contains both non-resonant (first) and resonant (second) terms. We now review the physical meaning of each of them in the elastic scattering case.

Non resonant terms

H'_1 is related to the Thomson scattering (section 3.1.1). We remind to the reader that this phenomenon is related to the scattering of photon by the whole electronic cloud, thus not allowing the difference between core and valence electrons. The latter accounting mainly for the magnetism, Thomson scattering cannot be used as an efficient probe for magnetic properties. It is always observed and is the dominant phenomenon for non-resonant photon energies. In this case and by neglecting H'_4, equation (3.20) becomes:

$$w = \frac{2\pi}{\hbar} \left| \langle 0 | H'_1 | 0 \rangle \right|^2 \tag{3.21}$$

and the scattering cross-section can be written as:

$$\frac{d\sigma}{d\omega} = r_0^2 \left| \sum_j \langle 0 | e^{i\mathbf{q}\cdot\mathbf{r}_j} | 0 \rangle \right|^2 (\mathbf{e}^*_\lambda \cdot \mathbf{e}_\lambda)^2 \tag{3.22}$$

with $\mathbf{q}$ the *momentum transfer*, defined as $\mathbf{q} = \mathbf{k} - \mathbf{k}'$. $\mathbf{e}_\lambda$ and $\mathbf{e}^*_\lambda$ correspond to the polarization vector of the incident and scattered wave, r_0 the Thomson radius. This formula contains the *atomic form factor* which is defined as

$$F(\mathbf{q}) = \sum_j \langle 0 | e^{i\mathbf{q}\cdot\mathbf{r}_j} | 0 \rangle \tag{3.23}$$

Equation (3.23) is proportional to the Fourier Transform of the electron density f_0:

$$f_0 = -r_0 F(\mathbf{q})(\mathbf{e}^*_\lambda \cdot \mathbf{e}_\lambda). \tag{3.24}$$

The element H'_4 is a small non-resonant term which contains a magnetic contribution related to the spin-orbit interaction. It is smaller compared to the Thomson scattering by a factor $(\hbar\omega_{\mathbf{k}}/mc^2)$ as demonstrated by Altarelli in ref. 108. Because in the x-ray region $\hbar\omega_{\mathbf{k}} \ll mc^2$, it represents a small contribution f_{mag} to the scattering amplitude. Its exact expression can be found in ref. [135].

Resonant terms

At resonance, the second term of equation (3.20) becomes dominant and then the scattering cross-section can be approximated as:

$$\frac{d\sigma}{d\omega} = |f_{res}|^2 \tag{3.25}$$

with f_{res} given in the electric dipole approximation by the *Hannon-Trammel formula* [119, 120]:

$$\begin{aligned} f_{res} = -r_0[\frac{1}{2}\mathbf{e}_\lambda^* \cdot \mathbf{e}_\lambda(F_{1,1}^e + F_{1,-1}^e) \\ - \frac{i}{2}(\mathbf{e}_\lambda^* \times \mathbf{e}_\lambda) \cdot \mathbf{z}(F_{1,1}^e - F_{1,-1}^e) + \\ (\mathbf{e}_\lambda^* \cdot \mathbf{z})(\mathbf{e}_\lambda \cdot \mathbf{z})(2F_{1,0}^e - \frac{1}{2}F_{1,1}^e - \frac{1}{2}F_{1,-1}^e)] \end{aligned} \tag{3.26}$$

with $\mathbf{z}$ the unit vector of the quantization axis. $F_{1,m}^e$ is defined as:

$$F_{1,m}^e = m_e \sum_n \frac{[E_n - E_0]^3}{\hbar^3 w_\mathbf{k}} \frac{|\langle n| R_m |0\rangle|^2}{E_0 - E_n + \hbar\omega_\mathbf{k} + i\Gamma_n/2} \tag{3.27}$$

with m_l magnetic quantum number defined as $-l < m_l < l$, l the azimuthal quantum number; Γ_n is the lifetime of the excited state as defined previously.

The Hannon-Trammel formula is describing the transitions between core electrons and d or f shells in transition metals. The magnetic sensitivity arises from the difference $F_{1,1}^e - F_{1,-1}^e$ which requires different populations in the levels $m_l = 1$ and $m_l =$ -1.

We can now write the total elastic scattering amplitude as [119, 136]:

$$f(\mathbf{q}, \hbar\omega) = f_0(\mathbf{q}) + f_{mag}(\hbar\omega) + f_{res}(\hbar\omega) \tag{3.28}$$

with f_0 the electron density and f_{mag} the spin-orbit contribution as described above.

Sensitivity to magnetism

Following Hannon *et al.* [119, 120] we can rewrite f_{res} as:

$$f_{res} \approx f_c(\mathbf{e}_\lambda^* \cdot \mathbf{e}_\lambda) - if_m(\mathbf{e}_\lambda^* \times \mathbf{e}_\lambda) \cdot \mathbf{z} \tag{3.29}$$

where f_c and f_m are described as complex numbers:

$$\begin{aligned} f_c &= f_c' + if_c'' \\ f_m &= f_m' + if_m'' \end{aligned}$$

The term f_c represents the resonant charge scattering; it gives information about the structural ordering in the sample. Note that this is not Thomson scattering due to the explicit energy dependency.

The second term f_m represents the resonant magnetization sensitive term that is probed through the transition of a spin-polarized photoelectron from a spin-orbit split core level to a magnetically polarized empty state above the Fermi level. It depends linearly on the magnetization vector and thus provides the magnetic contribution to the scattering amplitude at absorption resonances.

Introducing equation (3.29) in equation (3.28) shows the origin of the sensitivity of resonant scattering to magnetism at resonance due to the presence of the f_m term in the expression.

Determination of f'_m and $f"_m$

Momentum transfer and wavelength are related by:

$$\mathbf{q} = \frac{4\pi sin\theta}{\lambda}, \tag{3.30}$$

with θ the refractive angle.

In the soft x-ray range, the photon wavelength is large, hence the accessible **q**-range is rather small. This allows the use of the *optical theorem* which links the total cross-section to the forward scattering amplitude ($\mathbf{k} = \mathbf{k}'$ and $e'_{k'} = e_k$) [108]:

$$\sigma_{tot}(w) = \frac{4\pi}{k}\Im[f(0)] \tag{3.31}$$

In this case of forward scattering, f_0 and f_{mag} are pure real character. Equation (3.31) becomes then:

$$\begin{aligned}\sigma_{tot}(w) &= \frac{4\pi}{k}\Im[f_{res}] \\ &= \frac{4\pi}{k}f''\end{aligned} \tag{3.32}$$

with $f'' = f''_c + f''_m$ For transition metals, $\sigma_{tot} \approx \sigma_{absorption}$ in the soft x-ray range [137]. Therefore measuring the absorption allows one to evaluate f'' and by using the *Kramers-Kronig relation*, determination of $f' = f'_c + f'_m$ is possible via [138]:

$$f'(w) = \frac{2}{\pi}\int_0^\infty \frac{w' f''(w)}{w'^2 - w^2}dw' \tag{3.33}$$

Within the section 3.1, we have used the quantum formalism to describe absorption and scattering of soft x-rays in the elastic case. One should be reminded of the following:

- Absorption of polarized x-ray photons depend of the magnetization state of a material via the XMCD effect;
- Scattering is sensitive to magnetism due to the term f_m in the scattering amplitude.

3.2 Measuring in reciprocal space

X-ray crystallography is a well-established technique which has allowed important scientific discoveries such as the double-helical structure of DNA by Watson and Crick in 1953 [139]. This discovery happened at the Cavendish laboratory which was headed at that time by W.L. Bragg who established with his father, W.H. Bragg, one of the most important law of this field : the Bragg's law [140].

Crystallography measurements are performed in reciprocal space, related to real space by the Fourier Transformation. The momentum transfer **q**, which we have already met in the previous section, is measured in this space. This is the reason why we will now introduce the terms and concepts necessary to describe the artificial spin ice in the next chapter. This system can be regarded as a 2D crystal.

3.2.1 Unit cell

Any crystal is the periodic arrangement of a pattern called a *unit cell*; this unit cell can be composed of atoms, molecules, proteins... There is an infinity of possible unit cell. Amongst them one usually distinguishes *primitive* and *non-primitive* unit cells (figure 3.3). A primitive unit has the smallest possible size. Consequently, it contains only one lattice point [138]; a non-primitive unit cell on the other hand contains more than one lattice point. In both cases, translation of the unit cell is described by a set of vector $\mathbf{R}_n$. These translation vectors can be written in 2D:

$$\mathbf{R}_n = n\mathbf{a} + m\mathbf{b} \tag{3.34}$$

with m and n integers, and $\mathbf{a}$ and $\mathbf{b}$ real-space vectors.

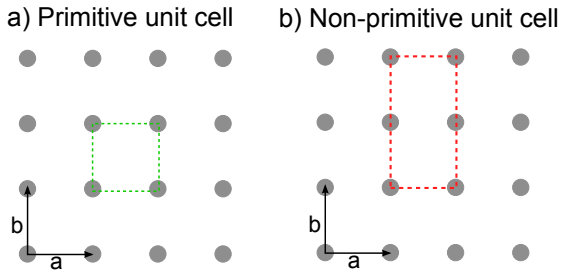


Figure 3.3: Unit cells. The crystal is obtained by the repetition of the unit cell by translation. However, an infinite number of unit cells can be considered. The unit cell in a) is called primitive unit cell as it is the smallest possible unit cell. The one in b) is a non-primitive unit cell.

3.2.2 Bragg diffraction

Let us consider the case of a crystalline magnetic material, the unit cell being composed of magnetic atoms. We already know the total scattering amplitude for an atom (equation (3.28)), and we can assume that the scattering signal for the material is the sum of the scattering signals for each of the atoms in the material:

$$A(\mathbf{q}) = \sum_l f_l(\mathbf{q}) e^{i\mathbf{q}\cdot\mathbf{r}_l} \tag{3.35}$$

with f_l the atomic form factor of the atom positioned at $\mathbf{r}_l$. The only component of equation (3.28) depending on $\mathbf{q}$ is the Thomson scattering term f_0. f_{mag} is negligible and f_{res} depends on the photon energy and on the angle between the magnetization $\mathbf{M}$ and $\mathbf{q}$. For the lattice defined by $\mathbf{r}_l = \mathbf{R}_n + \mathbf{r}_j$, with $\mathbf{r}_j$ the position of the atom in the unit cell, the scattering amplitude can be rewritten as:

$$A(\mathbf{q}) = \sum_{\mathbf{R}_n+\mathbf{r}_j} f_{0,j}(\mathbf{q}) e^{i\mathbf{q}\cdot(\mathbf{R}_n+\mathbf{r}_j)} = \sum_n e^{i\mathbf{q}\cdot\mathbf{R}_n} \sum_j f_{0,j}(\mathbf{q}) e^{i\mathbf{q}\cdot\mathbf{r}_j} \tag{3.36}$$

where the first term concerns the lattice and the second term concern the atoms comprising the unit cell, also known as the *unit cell structure factor* $F^{u.c.}(\mathbf{q})$:

$$F^{u.c.}(\mathbf{q}) = \sum_j f_{0,j}(\mathbf{q}) e^{i\mathbf{q}\cdot\mathbf{r}_j} \tag{3.37}$$

The scattering function $S(q)$ is expressed using equations (3.36) and (3.37) [138]:

$$S(\mathbf{q}) = |A(\mathbf{q})|^2 = |F^{u.c.}(\mathbf{q})|^2 \left| \sum_n e^{i\mathbf{q}\cdot\mathbf{R}_n} \right|^2 \tag{3.38}$$

$S(q)$ is the quantity measured during scattering experiment. From the equation, we note that when measuring its value with a detector, one is in fact measures $|A(\mathbf{q})|^2$ which leads to the loss of the information about the phase, an issue often referred as the *phase problem* [141]. This lost of phase prevents the reconstruction of the real space configuration. A solution is the use of one of the numerous phase retrieval algorithms [142]. It is however problematic when the initial information about the system is unknown.

Another solution is the use of x-ray holography. This technique uses a mask containing a reference hole which allows the encoding of the phase of the incident wave in the scattering pattern [143]. The real space image is then recovered by using an inverse Fourier Transformation on the scattering pattern. The strong advantage of this technique is that an initial guess on the sample configuration is not required.

Laue condition

The lattice term in equation (3.36) can be described as the sum of the space components. If we consider only two dimensions [138]:

$$\sum_n e^{i\mathbf{q}\cdot\mathbf{R}_n} = \sum_{u=0}^{Na} e^{i\mathbf{q}\cdot u\mathbf{a}} + \sum_{v=0}^{Nb} e^{i\mathbf{q}\cdot v\mathbf{b}} \tag{3.39}$$

with Na and Nb the number of unit cells.

Each of the component is a geometric series for which one can calculate the modulus. For the first term:

$$\left| \sum_{u=0}^{Na} e^{i\mathbf{q}\cdot u\mathbf{a}} \right|^2 = \frac{sin^2(\frac{Na\mathbf{q}\cdot\mathbf{a}}{2})}{sin^2(\frac{\mathbf{q}\cdot\mathbf{a}}{2})} \tag{3.40}$$

$S(q)$ presents a peak each time the denominator is equal to zero, implying $\mathbf{q}_x \cdot a = 2\pi h$ or $\mathbf{q}_x = 2h\pi/a$. One can recognise here the definition of a reciprocal lattice vector [138]:

$$\mathbf{a}.\mathbf{a}^* = 2\pi \cdot h \tag{3.41}$$

For the other term of (3.39), the same treatment can be applied, and one finds that the scattering vector is maximum when:

$$\mathbf{q} = \mathbf{G} \tag{3.42}$$

with G the reciprocal lattice vector defined as:

$$\mathbf{G} = h\mathbf{a}^* + k\mathbf{b}^* \tag{3.43}$$

h and k are the *Miller indices* (described below). $\mathbf{a}^*$ and $\mathbf{b}^*$ are the vectors of the reciprocal space equal to:

$$\mathbf{a}^* = 2\pi\frac{\mathbf{b}}{\mathbf{a}\cdot\mathbf{b}}; \mathbf{b}^* = 2\pi\frac{\mathbf{a}}{\mathbf{a}\cdot\mathbf{b}}$$

Equation (3.42) is known as the *Laue condition* for x-ray diffraction which is equivalent to *Braggs' law* [138].

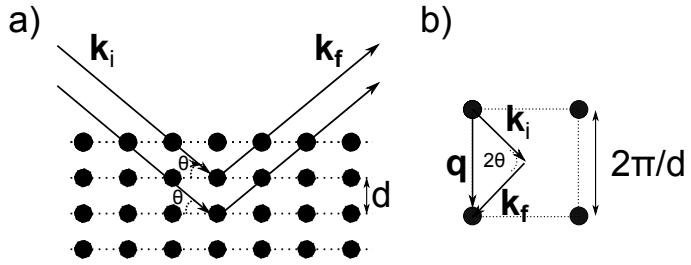


Figure 3.4: X-ray diffraction. a) Bragg's law illustrated in real space; b) Laue condition in reciprocal space.

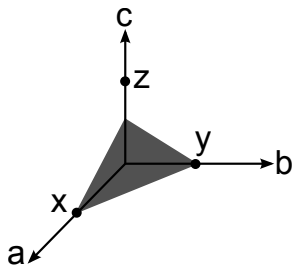


Figure 3.5: Miller indices. Miller indices are defined as the inverse of the crossing coordinate on the axis.

Bragg's law

Bragg's law is:

$$n\lambda = 2dsin\theta \tag{3.44}$$

with n an integer, λ the photon wavelength, d the interplanar distance and θ the incident angle (figure 3.4).

For the first order ($n = 1$), one can link $\mathbf{q}$ and d by using equation (3.30):

$$q = \frac{4\pi sin\theta}{\lambda} = \frac{2\pi}{d} \tag{3.45}$$

This shows how measurements in the reciprocal space are related to distances in real space.

Miller indices

We now come back to the Miller indices which we have introduced previously (h and k in equation (3.43)). They are used to specify directions and planes in crystals [144]. To define them, let us consider the figure 3.5. The considered plane crosses the axis a, b and c in x,y and z respectively. The Miller indices are defined as the inverse value of these intersections, therefore to $h = \frac{1}{x}$, $k = \frac{1}{y}$ and $l = \frac{1}{z}$. In the considered example, $x = 1$, $y = 1$ and $z = \frac{1}{2}$, so the plane is defined by (112). If the plane does not cross one axis, then the corresponding Miller index is equal to 0: if the value is negative, the index is written $\bar{h}$. The number of Miller indices depends on the dimensionality of the crystal: in the case of artificial spin ice which is a 2D crystal, we use only two Miller indices.

3.2.3 Ewald's construction

Introduced by P. Ewald in 1965 [145], the Ewald's construction is a way to visualize the Bragg reflections which can be observed in reciprocal space.

In two dimensions, it is a circle of radius $k = 2\pi/\lambda$ (*Ewald's circle*), i.e. its radius depends on the wavelength of the probe used. It is rather small in the soft x-ray range ($\lambda \approx 10$ nm), but is large when electrons are used, typically in transmission electron microscopy ($\lambda \approx 5$ pm).

The wavevector of the incident photons k_i is placed into the reciprocal space with its tip ending on a lattice point. The Ewald's circle is then defined by the extremities of the **q** vector. Each point located on this circle will obey the Laue condition (equation (3.42)) and gives a Bragg reflection which will be observed in the scattering pattern. This construction can be extended to three dimensions, where it will be a sphere (*Ewald's sphere*).

It is important to stress that the Ewald's construction is not only a geometrical construction. Indeed, it has a direct influence on the scattering pattern, as we will see in chapter 4.

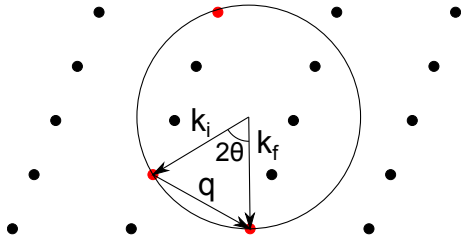


Figure 3.6: Ewald's construction. All the points located on the circle of radius $k = 2\pi/\lambda$ will give a Bragg reflection, as they obey the Laue condition.

Chapter 4

Resonant scattering on artificial spin ice

Contents

4.1 Method 58

4.1.1 Sample preparation and characterization 58

4.1.2 Experimental set-up 59

4.2 Kinematic theory of x-ray diffraction 62

4.2.1 Kinematic theory 62

4.2.2 Extension of the theory to two dimensions 64

4.2.3 Simulations 65

4.3 Bragg scattering on artificial square ice 65

4.3.1 As-grown ordering 65

4.3.2 First magnetization curve 66

4.3.3 Magnetization reversal 70

4.3.4 Determination of the nanomagnet contributions to the remanent magnetization 71

4.4 Diffuse scattering on an artificial kagome ice array 76

4.4.1 As-grown state 76

4.4.2 First magnetization 77

4.4.3 Field dependency of the diffuse scattering 78

4.4.4 Analysis of the diffuse scattering : difficulties and solutions . . . 80

4.4.5 Evolution of the dichroic contrast during magnetization reversal 81

4.5 Summary 84

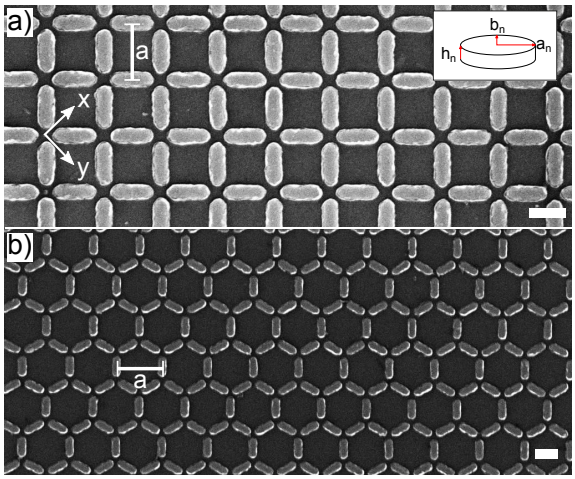


Figure 4.1: SEM pictures of artificial square (a) and kagome (b) spin ice arrays. Islands are 230 nm by 80 nm in length and width respectively, a is the lattice parameter. The scale bar (in white) represents 200 nm.

In this chapter, we present the results of our investigation on artificial spin ice using soft x-ray resonant magnetic scattering (SXRMS). In the first section, we start out with the presentation of the samples and the characterization of their magnetic properties. We also include in this section a description of the experimental set-up. We then present the model, which is based on the kinematic theory of x-ray diffraction that we have developed to simulate and interpret the experimental data.

The third section is dedicated to Bragg scattering on artificial square ice arrays. We show that real space information can be retrieved from the scattering patterns. We observed pure magnetic signal arising from the magnetic configuration of the sample, and we used x-ray magnetic circular dichroism (XMCD) to follow the evolution of the magnetization as a function of an applied external field. We also discuss the limitations of our model in this section.

The last section of this chapter reports our SXRMS studies of the artificial kagome ice array. We were able to observe magnetic diffuse scattering which originates from deviation from the perfect magnetic order. We present our analysis and also explain which difficulties are met in the interpretation of the scattering pattern. Finally, we propose a relation between diffuse scattering and change of the dichroic contrast during the inversion of the magnetization.

4.1 Method

4.1.1 Sample preparation and characterization

Preparation

Following the lithography process described in chapter 2, we produced arrays as large as 2×2 mm^2 of nanomagnets of 230 nm in length and 80 nm in width (figure 4.1). For the artificial square ice (4.1a) the lattice parameter a is equal to 310 nm while in the artificial kagome ice (4.1b), it is equal to 550 nm. The nanomagnets are composed of 20 nm Permalloy capped by a 5 nm aluminium layer to prevent oxidation. The materials were deposited using thermal evaporation at a base pressure of $1{\cdot}10^{-7}$ mbar.

Characterization

Characterization was performed following lift-off. The sample structural quality was checked using scanning electron microscopy (SEM). In particular, we verified that no defects were present in the arrays.

Characterization of the magnetic properties of the arrays using MOKE has been done in collaboration with Dr. P. López-Barberá and Pr. Dr. J. Nogués from the Institut Català de Nanotechnologia in Barcelona, Spain. In-plane hysteresis loops were recorded at different angles. We present in figure 4.2 two such hysteresis loops. The hysteresis curve shown in panel (a) has been recorded on the artificial square ice with longitudinal MOKE applying the magnetic field at 45° to the islands' long axis. Panel (b) shows a hysteresis loop recorded on the artificial kagome ice. These geometries correspond to one of the SXRMS experiments presented in the following sections. In both cases, one notes that the magnetization at remanence is inferior to the one at saturation. Let us take the example of the artificial square ice as presented in figure 4.3. When the applied external field is above 400 G (panel a), the magnetic field is strong enough to overcome the shape anisotropy. Therefore, the magnetic moments point in the field direction. However, when the external field is removed (panel b), the magnetic moments fall back to be parallel to the long axis of the nanomagnets (easy axis), thus the total magnetization at remanence is inferior to the total magnetization at saturation. The degree of remanence is nevertheless high for both square and kagome arrays.

We also verified that the size of the nanomagnets was suitable to obtain a single magnetic domain behaviour [29,146]. To do so, we performed micromagnetic simulations using the code OOMMF[1]. To describe the nanomagnets of $230\times80\times20$ nm^3 in length, width and thickness, respectively, we used a unit cell size of $5\times5\times5$ nm^3. The material's parameters were set to $M_s = 860{\cdot}10^3$ A.m^{-1} and A = $13{\cdot}10^{-12}$ J.m^{-1} (exchange constant), as used in the literature [147, 148]. The initial magnetic configuration was obtained by random distribution of the cells, followed by saturation using an external magnetic field. We present in panel (a) of figure 4.4 the result of this simulation at remanence. We observe that all magnetic moments are pointing along the long axis of the nanomagnet as one can expect for such small particles.

Following the OOMMF simulations, we investigated these nanomagnets with photoelectron emission microscopy (PEEM) (figure 4.4b and c). This allows imaging of the nanomagnets with 50 nm spatial resolution. They have been placed on an arrangement used in magnetoplasmonic devices (Annex A), and do not exhibit the artificial spin ice behaviour in this case. The XMCD image shown in panel c) of the figure has been obtained by recording two images with opposite circularly polarized photons and dividing one by the other one. When the magnetization of the nanomagnets is parallel (anti-parallel) to the incoming x-rays, the nanomagnets appears black (white); if the magnetization is perpendicular, they appear grey. We note that within the spatial resolution of PEEM, the nanomagnets have indeed a monodomain state.

4.1.2 Experimental set-up

Diffractometer

The scattering experiments presented in this thesis have been performed using the diffractometer RESOXS, which is located at the beamline SEXTANTS of Synchrotron SOLEIL (figure 4.5a) [149, 150]. This beamline is dedicated to scattering in the soft x-ray range,

[1]Code available at http://math.nist.gov/oommf/

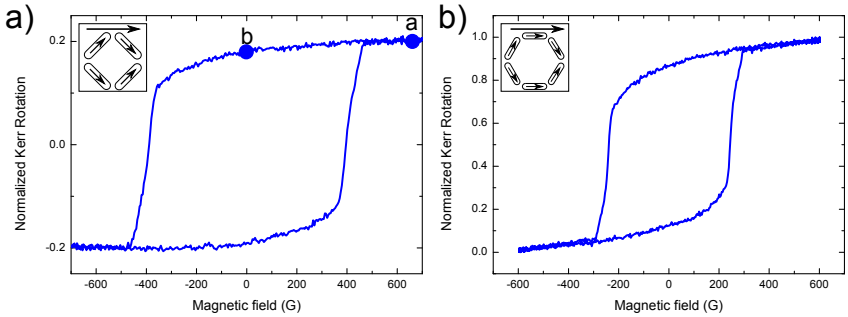


Figure 4.2: NanoMOKE hysteresis curves of patterned Permalloy thin films. Hysteresis curves were measured on artificial square (a) and on kagome spin ice (b), with the configuration shown in insets. In panel (a), the points a and b refer to the magnetic configurations presented in figure 4.3.

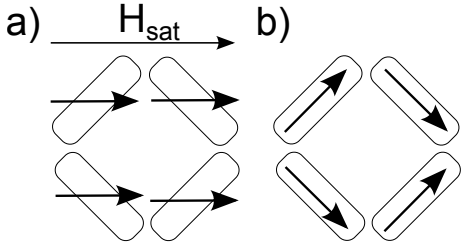


Figure 4.3: Magnetic configurations of artificial square ice. At saturation (panel a), the magnetic moments are poiting along the external applied field. However this situation is not energetically favourable and when the saturating field (H_{sat}) is removed (panel b), the magnetic moments are falling back along the easy axis of the nanomagnets, i.e., the long direction.

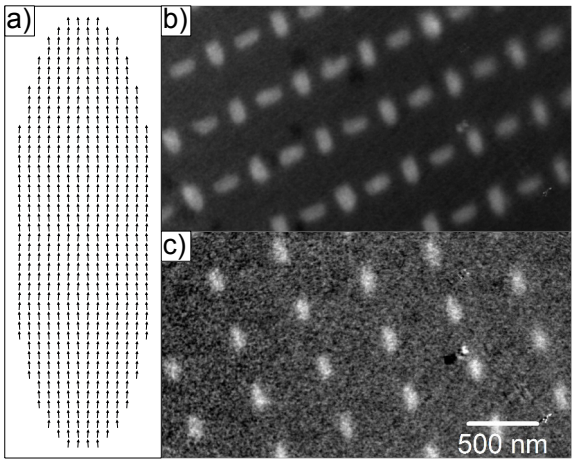


Figure 4.4: Single magnetic domain. a) Micromagnetic simulation of a single nanomagnet performed with OOMMF. b) PEEM picture of a saturated sample consisting of nanomagnets. It has been recorded at the Fe L_3-edge with circularly polarized light. c) XMCD picture obtained at the Fe L_3-edge. Magnetization aligned with the beam direction appears white, while islands with a perpendicular magnetization direction do not yield a XMCD signal and thus match the colour of the background. Pictures b) and c) have been provided by Pr. Dr. J. Nogués, *Institut Català de Nanotechnologia* and have been recorded using the PEEM endstation located at the beamline CIRCE of the synchrotron ALBA.

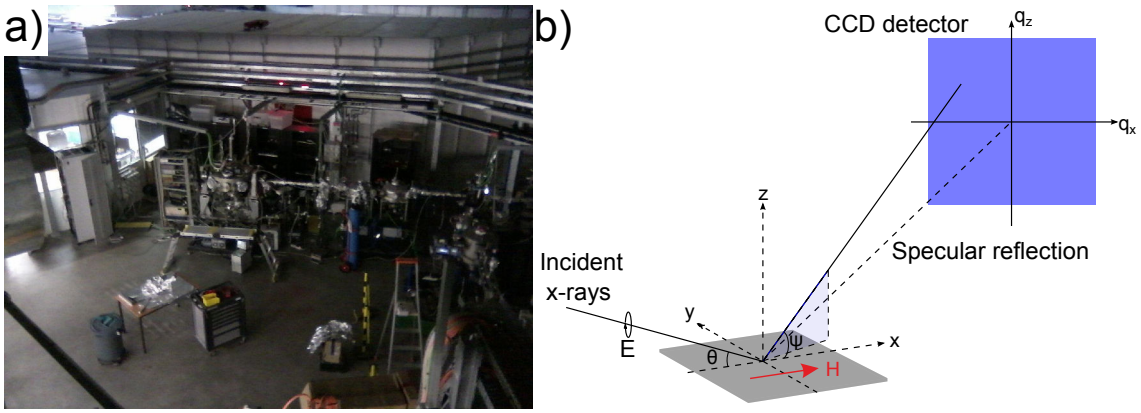


Figure 4.5: RESOXS endstation at beamline SEXTANTS, synchrotron SOLEIL. A sketch of the experimental geometry is given on the right side. The sample is mounted on a rotation (θ) and the detector on a second rotation (2θ). The notation θ and 2θ are usual notation used for reflectivity experiments.

between 50 eV and 1070 eV, with an average flux of $1^{1}3$ photons on the sample depending on the energy. There are three branches dedicated to different techniques, including the elastic scattering branch where the diffractometer is.

This instrument was originally designed with a photodiode on the 2θ arm and has been upgraded in 2012 with a charge-coupled device (CCD) camera as an additional detector. This allows the recording of an extended portion of the **q**-space at once. To be sensitive to the in-plane magnetization of the nanomagnets, experiments were carried out using the reflection geometry as illustrated in figure 4.5b. We define the reference system: x corresponds to the beam axis and y points towards the storage ring. The incident angle θ_i and the reflective angle ψ are 8°.

The CCD detector contains 2048 × 2048 pixels, each with a size of 13.5 μm^2, the distance between the detector and the sample is 25 cm. Considering the specular reflection to be in the center of the detector, the angular opening in the horizontal direction is equal to ±3° and the angular opening in the vertical direction is equal to $8 \pm 3°$. With these conditions, the detector is able to cover a momentum transfer range of about $\Delta q_x = \pm 2{\cdot}10^{-1}$ nm^{-1} and $\Delta q_z = \pm\ 1$ nm^{-1}.

Magnetic fields were applied *in situ* using two pairs of electromagnets. This allows us to generate a field of up to 2000 G (0.2 T) in any direction parallel to the sample plane [149]. In our experiments, the field was applied along the y direction as illustrated in panel b of figure 4.5.

Rocking curves

One common measurement performed in scattering experiments is the rocking curve. It is obtained by keeping the incident angle θ constant and moving the detector around the specular beam, thus varying the reflective angle ψ (figure 4.6). The rocking curve can be represented as a function of ψ, of $\theta + \psi$ or the momentum transfer in the scattering plane q_x.

In the experiments that we carried out, performing a rocking curve provided a way to align the CCD detector as described in the following. We note that any CCD image is a rocking curve. The incidence angle is fixed, and the CCD records the intensity for different reflective angles. However, the poor dynamic range compared to a 1D detector renders the

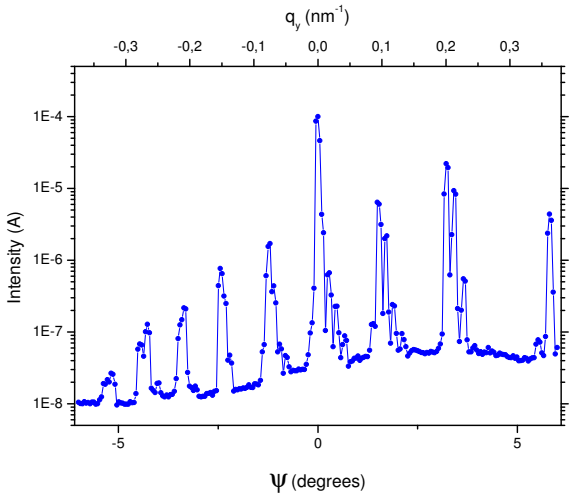


Figure 4.6: Rocking curve recorded for an artificial square ice array with an incident angle of 10°. ψ is the reflective angle.

rocking curves less interesting. We also used rocking curves to measure **q** values, in order to obtain the average value of the lattice parameters and to compare it with their expected values.

We present an example of rocking curve measured on artificial square ice in figure 4.6. The most intense peak located at $q_x = 0$ ($\theta = \psi$) corresponds to the reflection of the direct beam and is referred to as the specular peak. The other peaks on the rocking curve are Bragg peaks of increasing order. The numerous satellite peaks observed in figure 4.6 are Bragg peaks located at different values of q_z; they have been recorded due to the finite length of the slit present in front of the photodiode in this direction. As the 1D detector moves on a circle with the 2θ arm of the instrument, it moves along the Ewald's sphere (section 3.2.3). This presents an advantage to extract information as from a scattering pattern recorded with a 2D detector since in this latter case one needs to take into account the projection of the Ewald's sphere on the detector plane.

Alignment procedure

Alignment of the CCD camera was performed in two steps. First, we optimized the position of the photodiode in all directions using rocking curves similar to the one presented in figure 4.6. Then, the center of the CCD camera is placed at the position of the photodiode, with a beam stop protecting the detector against damage from the intense specular beam. The flux of incoming x-ray photons can be adjusted by inserting gold filters with different thicknesses prior to the diffractometer.

4.2 Kinematic theory of x-ray diffraction

4.2.1 Kinematic theory

To interprete our experimental data, we developed simulations based on the kinematic theory of x-ray diffraction [130]. This theory is based on two assumptions:

- scattering events on neighbouring atoms are independent;
- the scattered photons are not scattered any further (no multiple scattering).

Note that these two simplifications are correctly taken into account within the dynamical theory of x-ray diffraction [151]. We did not use the latter theory as only the first atomic layers of our samples interact with the incident x-ray beam due to the small incident angle. Therefore, the beam is not scattered deeply in the material and multiple scattering events are rare. Moreover, the kinematic theory proved to be sufficient to build an efficient model to reproduce our experiments.

The kinematic theory allows us to use the following approximation to simplify the theoretical treatment of our scattering experiments:

- Born approximation: the atomic form factor is the Fourier transform of the electron density (equation (3.24));
- the scattering signal mainly arises from the first atomic layers due to the strong absorption of the soft x-rays, in particular in the vicinity of absorption resonance;
- in addition, we assume that the nanomagnets are uniform, i.e. the atomic form factor is the same for all atoms of the nanomagnets.

Intensity of the scattered wave

In the resonant regime, assuming coherent illumination, the intensity of the scattered beam is related to the magnitude squared of the total atomic scattering factor $f_j(\mathbf{q}, \hbar\omega)$ [135]:

$$I(\mathbf{q}, \hbar\omega) \propto \left| \sum_j f_j(\mathbf{q}, \hbar\omega) \exp(i\mathbf{q} \cdot \mathbf{r}_j) \right|^2 \tag{4.1}$$

with $f_j(\mathbf{q}, \hbar\omega)$ the atomic scattering factor of an atom located at position r_j and $\hbar\omega$ the photon energy. We remind the reader that $f_j(\mathbf{q}, \hbar\omega)$ is given by [119, 120]:

$$f(\mathbf{q}, \hbar\omega) = f_0(\mathbf{q}) + f_{mag}(\hbar\omega) + f_{res}(\hbar\omega) \tag{4.2}$$

with the terms as defined in section 3.1.2.

In the following:

- we neglect the dependence on $\mathbf{q}$ since only small momentum values are probed in the soft x-ray regime;
- we neglect f_{mag} which accounts for the scattering due to the spin-orbit interaction, which is negligible compared to the Thomson scattering and to the resonant terms of the scattering amplitude [110];
- f_0 is the Thomson scattering term; in the limit of small momentum, it is equal to the number of electrons Z.

Therefore, we can rewrite equation (4.2) and obtain in first approximation using equation (3.29) [119, 120]:

$$f_j(\hbar\omega) \approx (Z + f_c)(\mathbf{e}'_\lambda \cdot \mathbf{e}_\lambda) - i f_m (\mathbf{e}'_\lambda \times \mathbf{e}_\lambda) \cdot \mathbf{m}_j \tag{4.3}$$

where $\mathbf{e}_\lambda$ and $\mathbf{e}'_\lambda$ are the polarization vectors of the incident and scattered photons respectively, and $\mathbf{m}_j$ the unit vector of the magnetic moment at the j^{th} site. We remind the reader that f_c represents the resonant charge scattering and is added to the Thomson scattering at resonance; on the other hand, f_m depends linearly on the magnetization vector.

In the following, we have worked with a photon energy of 706.8 eV (Fe L_3-edge) because it corresponds to the valence bands, where the electrons responsible for the magnetic properties of Fe are located. It also presents a strong absorption as shown in fig. 3.2. For this edge, we will use $f_c = 10.554 + i59.388$ and $f_m = -10.895 - i12.361$. These values have been determined using the method from Sève and co-workers [152]. In their work, they performed scattering experiments at the $L_{2,3}$ absorption edge of Ni on an Ag/Ni multilayer. Using the angular variation of a first-order Bragg peak, they recovered the value of f_c and f_m. They found results similar to those calculated with the Kramers-Kronig relations (paragraph 4 of ref. 152).

By combining the atoms belonging to the same nanomagnet and summing over all nanomagnets, the scattering intensity becomes [2]:

$$I(\hbar\omega) \propto \left| \sum_n f_n(\hbar\omega) F_n(\mathbf{q}) \exp(i\mathbf{q} \cdot \mathbf{r}_n) \right|^2 \tag{4.4}$$

with F_n the form factor of the n^{th} nanomagnet located at position r_n. Assuming the nanomagnets to be homogeneous Permalloy particles of volume V with uniform magnetization, the form factor is given by:

$$F_n(\mathbf{q}) = \frac{1}{V_n} \int_{V_n} \exp(i\mathbf{q} \cdot \mathbf{r}) d^3\mathbf{r} \tag{4.5}$$

We do not write explicitly the expression of F_n here, but will return to this in section (4.3.4).

4.2.2 Extension of the theory to two dimensions

Although the scattering pattern of artificial 2D magnetic structures has already been measured using a CCD camera [10, 153], surprisingly, we did not find in the literature a set of equations to describe the scattering out of the scattering plane. To address our results and allow direct comparisons between experiment and simulation, we therefore developed a set of equations, based on the one introduced by van der Laan [154]. For this we employed the scattering geometry presented in figure 4.5 and reproduced in figure 4.7 for clarity: x is the beam axis, θ the incident angle, ψ the reflective angle and φ the angle between the beam axis and the scattered beam in the x-y plane . Using these coordinates, we can rewrite the polarization unit vectors as:

$$\mathbf{e}_\sigma = (0, 1, 0) \qquad \mathbf{e}_\pi = (sin(\theta), 0, cos(\theta))$$

$$\mathbf{e}'_\sigma = \frac{k' \times k}{|k' \times k|} \qquad \mathbf{e}'_\pi = \frac{k' \times \mathbf{e}'_{sigma}}{\left| k' \times \mathbf{e}'_{sigma} \right|}$$

and the vectors of the incident and scattered beam as:

$$\mathbf{k} = (cos(\theta), 0, -sin(\theta)) \qquad \mathbf{k}' = (cos(\psi)cos(\varphi), cos(\psi)sin(\varphi), sin(\psi))$$

We can write the expression of the dot and triple products from equation (4.3) using the matrix form of the scattering channels $\begin{pmatrix} \sigma\to\sigma' & \pi\to\sigma' \\ \sigma\to\pi' & \pi\to\pi' \end{pmatrix}$ (in the following, we replace sin by s and cos by c to simplify the writing) [154]:

[2] By assuming coherent scattering. Otherwise: $I(\hbar\omega) = \sum \left| \sum_n f_n(\hbar\omega) F_n(\mathbf{q}) \exp(i\mathbf{q} \cdot \mathbf{r}_n) \right|^2$

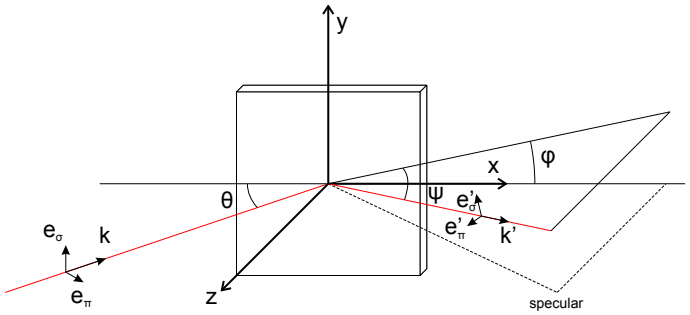


Figure 4.7: Scattering geometry. x is the beam axis, θ the incident angle, ψ the reflective angle and φ the angle between the beam axis and the scattered beam in the x-y plane.

$$\mathbf{e}_\lambda^* \cdot \mathbf{e}_\lambda = \begin{pmatrix} c\varphi & -s\theta s\varphi \\ -s\psi s\varphi & -s\theta s\psi c\varphi + c\theta c\varphi \end{pmatrix} \tag{4.6}$$

$$(\mathbf{e}_\lambda^* \times \mathbf{e}_\lambda) \cdot \mathbf{m_j} = \begin{pmatrix} -s\varphi z_z & c\theta c\varphi z_x + c\theta s\varphi z_y - s\theta c\varphi z_z \\ -c\phi z_x - s\psi c\varphi z_z & -c\theta s\psi s\varphi z_x - (c\theta s\psi c\varphi + s\theta c\psi) z_y + s\theta s\psi s\varphi z_z \end{pmatrix} \tag{4.7}$$

with $\mathbf{m_j} = (z_x, z_y, z_z)$.

4.2.3 Simulations

We consider the nanomagnets to be Ising spins, i.e., one single magnetic moment. As demonstrated by Rougemaille and co-workers [155] , this is not necessarily the case in reality. We will discuss later that this can explain differences between experiment and simulation that we observe for higher diffraction orders. We also assume that the spins are completely aligned along the structural axis.

4.3 Bragg scattering on artificial square ice

In the following section, we will refer to Bragg peaks with $h^2 + l^2 = 1$ as *first order Bragg peaks* and with $h^2 + l^2 = 2$ as *second order Bragg peaks*, with h and l being the respective Miller indices.

4.3.1 As-grown ordering

Soft x-ray magnetic scattering (SXRMS) patterns recorded on an artificial square ice in the as-grown state are presented in figure 4.8. As illustrated in panel (a) of the figure, the nanomagnet array is oriented such that the incident beam is parallel to the diagonal of the square lattice. As the applied magnetic field is also oriented in this direction, such a configuration ensures that for a perfect alignment all magnetic moments see the same applied field.

Description of the square lattice

The pattern recorded for an off-resonance photon energy (690 eV) is shown in figure 4.8b. Since there is no magnetic component in the non-resonant atomic form factor (section

3.1.2), this pattern results from pure charge scattering of the nanomagnets and contains only information about structural properties of the array. To understand the positions of the Bragg peaks, we therefore need to consider only the structure of the artificial square ice (figure 4.8a). The square lattice can be decomposed in two sublattices which are characterized by the different orientations of the nanomagnets as indicated by white and grey in figure 4.8a; the primitive unit cell contains one nanomagnet from each sublattice, and is repeated on a square lattice with periodicity a (the lattice parameter) to form the square array. As a consequence, the Bragg peaks are arranged on a square lattice with periodicity $2\pi/a$. We have highlighted in figure 4.8b the first order Bragg peaks with dashed lines. Note that these lines do not form a square because of the stretching of the scattering pattern in the horizontal direction due to the reflection geometry. In addition, the Bragg peaks are located on arcs as a consequence of the projection of the Ewald's sphere on the detector plane; the tilt of these arcs is caused by a slight misalignment of the CCD and the sample with respect to the scattering plane.

Magnetic ground-state ordering

By tuning the photon energy to an absorption edge, additional resonant terms are added to the atomic form factor (section 3.1.2). Most importantly, this is the term f_m which is sensitive to the magnetization. As expected, tuning of the photon energy to the Fe L_3-edge (706.8 eV) gives rise to additional Bragg peaks in the scattering pattern (figure 4.8d). Since the peaks are located between the structural Bragg peaks, they have to be of pure magnetic origin. In fact, they indicate the presence of a long-range order of the nanomagnets moment in the as-grown state of the system, as previously reported in the literature [58,82]. The primitive cell of this magnetic ground-state is presented in the panel c of the figure 4.8. It contains four nanomagnets (against two in the structural case) and is repeated on a square lattice with periodicity $a\sqrt{2}$. Note that the lattice (as indicated by the translation vectors) is rotated by 45 degrees relative to the case of the structural lattice. Therefore, the magnetic Bragg peaks form a square lattice placed in-between the structural peaks with a smaller periodicity $2\pi/a\sqrt{2}$.

4.3.2 First magnetization curve

We followed the evolution of the scattering pattern from the as-grown state as a function of an applied external magnetic field. At each step, we applied the magnetic field along the beam axis and then removed it to measure the scattering pattern at remanence to keep the magnetic moments aligned along the nanomagnets' long axis. Four scattering patterns recorded at increasing field values are shown in figure 4.9. No changes in the intensity of the magnetic Bragg peaks are observed for $H < H_c$; for $H > H_c$, one notes a strong decrease of their intensity until no signal is observed (figure 4.10 b). This behaviour is in agreement with the reversal of the individual magnetic moments in the direction of the applied magnetic field, which annihilates the as-grown state ordering.

To extract quantitative information from the scattering patterns, we performed simulations starting from an ordered array in the magnetic ground-state to the saturated state. At each step of the simulation, a given number of magnetic moments were flipped randomly in the direction of the external magnetic field. We are here interested in the Bragg peaks which brings statistical information on a large portion of the array. Therefore, the exact arrangement of the magnetic moments is not relevant for the simulation, but rather the amount of moments pointing along the beam direction and the amount pointing in the opposite direction.

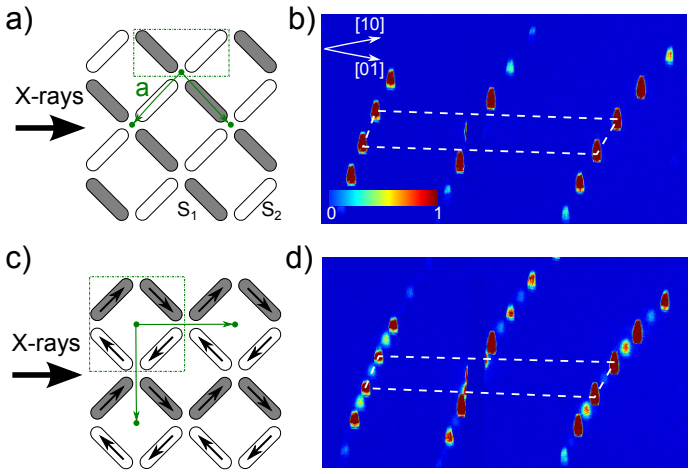


Figure 4.8: Scattering pattern on artificial spin ice in the as-grown state. a) Illustration of the sample geometry. The dashed box indicates the structural unit cell, containing two nanomagnets with different orientations. The corresponding two sublattices S_1 and S_2 are highlighted in gray and white, respectively. The green arrows represent the lattice vectors and the dots indicate the square lattice, which has periodicity a. b) Experimental scattering pattern recorded off-resonance (690 eV), containing structural information only. The first order Bragg peaks are connected by a dashed box. c) Illustration of the magnetic ground state, consisting of alternating rows of nanomagnets (highlighted in gray and white) with magnetic moments pointing towards opposite directions. The magnetic unit cell, twice as large as the structural one, is indicated by the dashed box.(d) Experimental scattering pattern recorded at the Fe L_3 edge (706.8 eV), including both structural and magnetic information. Additional Bragg peaks of pure magnetic origin can be observed due to the long range ground-state ordering.

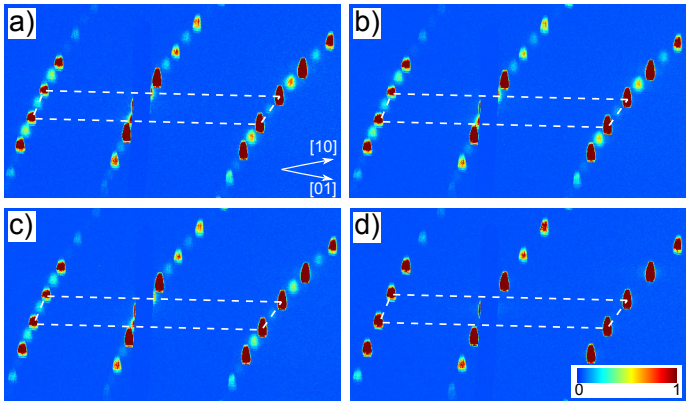


Figure 4.9: Scattering pattern recorded at 707 eV during the first application of an external field. The scattering patterns have been recorded at a) 0G, b) 300 G, c) 600 G and d) 900 G.

Table 4.1: Degree of ground-state ordering during first magnetization. Values derived from the $(3/2\,\bar{3}/2)$ Bragg peak (reference in figure 4.10) as discussed in the text.

Magnetic field	**Experimental normalized intensity**	**Simulated normalized intensity**	**Ground-state ordering**
250 G	1 ± 0.01	1 ± 0.01	> 95 %
400 G	0.95 ± 0.01	0.94 ± 0.01	95 %
700 G	0.88 ± 0.01	0.83 ± 0.01	90 %
750 G	0.65 ± 0.01	0.66 ± 0.01	80 %
800 G	0.03 ± 0.01	0.03 ± 0.01	20 %
850 G	0.01 ± 0.01	0.01 ± 0.01	10 %
900 G	0	0	0 %

Our data suggests a high degree of ordering in the as-grown state, above 95 % (table 4.1). This value has been obtained by comparing the normalized intensity of the magnetic Bragg peak $(3/2\,\bar{3}/2)$ in experiment and simulation where few defects in the perfect magnetic ordering have been introduced. We can relate the real space imaging performed on a similar array [156]. The artificial square ice is organized in large domains of type I vertices separated by domain walls of type II and type III vertices (figure 1.8). This important ordering is however not complete, i.e. the array is not formed only by type I vertices. Such a case has not been reached in the as-grown state of nanomagnets with static moments. It has only been achieved by exploiting thermal annealing combined to superparamagnetic nanomagnets [70].

We followed the evolution of intensity of eight magnetic Bragg peaks, and report them in figure 4.10 for both experiments and simulations. In order to estimate the total magnetization we compared the peak intensity normalized to the ground state. For example, we report in table 4.1 the results for the $(3/2\,\bar{3}/2)$ peak. Good agreement is reached between experiment and simulation.

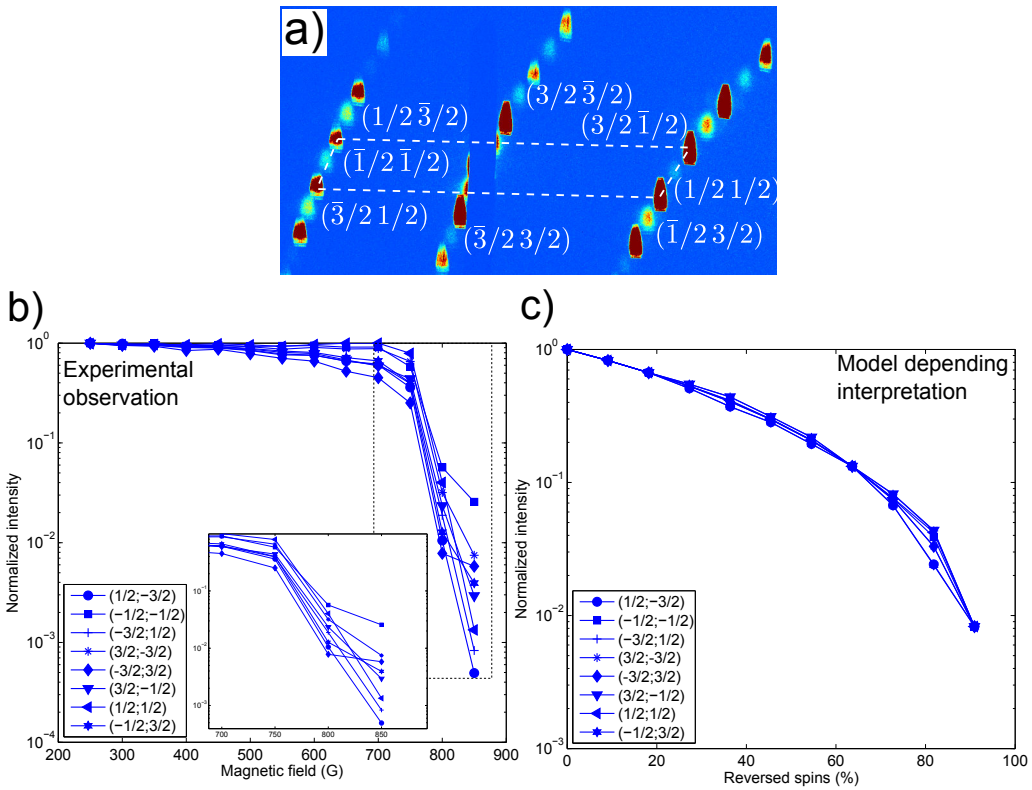


Figure 4.10: Evolution of the magnetic Bragg peaks intensities. a) Miller indices of the magnetic Bragg peaks. b) Evolution of the normalized intensity of the magnetic Bragg peaks as a function of the magnetic field. c) Evolution of the intensity for the same peaks derived from the amount of reversed spins.

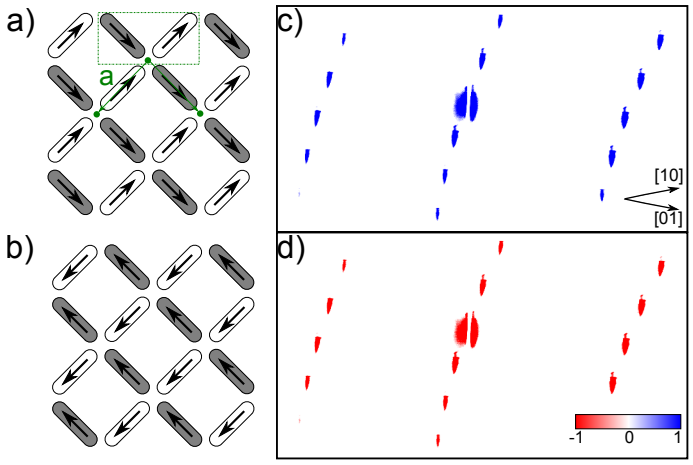


Figure 4.11: Magnetic dichroism of the scattering pattern recorded at opposite saturation. The scattering patterns exhibits only Bragg peaks at the location of the non-resonant (structural) Bragg peaks. To follow the evolution of the magnetic contribution to the scattering, we used the XMCD.

4.3.3 Magnetization reversal

Once the sample is saturated, the purely magnetic Bragg peaks have disappeared (figure 4.9d). The magnetic and structural unit cells are identical (figure 4.11a), and the scattering pattern exhibits Bragg peaks only at the positions corresponding to this periodicity. No magnetic peaks appear while moving further along the hysteresis loop. This is a stronger confirmation that no large domain of type I vertices are formed. Indeed, no such domains have been observed with PEEM and MFM which only probe small areas and have therefore a limited field of view. On the other hand, scattering probes the entire sample and indicates that no significant fraction of ordered regions exist. This is coherent with what has been described in the literature. As we discussed in section 1.4.2, the nanomagnets have a distribution of coercivities related to the defects induced by the lithography process, which is also referred as *quenched disorder* [56, 157]. This disorder prevents the system from reaching low-energy magnetic states by means of a demagnetization process [157].

In order to extract the magnetic component of the Bragg peaks, we recorded scattering patterns with right- and left-handed polarizations. As discussed in section 3.1.1, subtracting one from the other (equation (3.12)) yields the magnetic component. The dichroic contrast characterizing the remanent state after saturation along the beam axis are shown in figure 4.11. When all magnetic moments points towards the direction of the beam (y in figure 4.7), the observed dichroic contrast corresponds to its largest positive value which is shown by the blue colour of the peaks (figure 4.11b). The lowest negative value is observed after saturation along the negative y-axis, illustrated by a red colour of the peaks (figure 4.11d).

Applying a reverse magnetic field following saturation leads to changes in the dichroic scattering pattern, with particularly strong changes occurring for applied field values around the coercive field where the magnetization reversal takes place. As already observed by Morgan and co-workers [86], the dichroic contrast does not change equally for all Bragg peaks, but can differ from peak to peak. We show in the following that is via these differences that a detailed insight can be obtained into the reversal process.

In figure 4.12 we show the hysteretic behaviour of the dichroic intensity of four Bragg peaks (see figure 4.12a, c and d): the two first order peaks $P_1 = (10)$ and $P_2 = (01)$ and

the two second order peaks $P_3 = (1\bar{1})$ and $P_4 = (\bar{1}1)$. The hysteresis curves of the first order peaks (figure 4.12c) reveal a small difference in their respective coercive fields of $H_{P_1} = 475 \pm 2$ Oe and $H_{P_2} = 455 \pm 2$ Oe. The behaviour of the two second order peaks P_3 and P_4 (see figure 4.12d) are identical within the experimental uncertainty with a coercive field value of $H_{P_3} = H_{P_4} = 468 \pm 2$ Oe. Note that this value is close to the mean value of the coercive fields of the two first order peaks.

The observation of different coercive fields for the two first order peaks (P_1 and P_2) can be understood by assuming a slight misalignment between the sample axis and the direction of the applied magnetic field, i.e. $\varphi_1 > \varphi_2$ as illustrated in figure 4.12b. Discussion on how P_1 and P_2 are sampling the different sublattices is performed in the next section. Here we focus on the consequence of such a misalignment, which increases the applied effective field along the long axis of the nanomagnets for the sublattice S_1 (in white), while it is decreased for the sublattice S_2 (in gray). Consequently, the magnetic moments on sublattice S_1 will tend to switch at a lower external field value than the moments on S_2, thus giving rise to the small difference in the apparent coercive field. From the coercive field values of P_1 and P_2, we can estimate the angle of misalignment, which we find to be smaller than 1.5°. The observation of different coercive fields for the two sublattices is also in line with the absence of such a difference in the hysteresis curves of the two second order Bragg peaks (P_3 and P_4). The reason for this is that these peaks sample both sublattices equally. Consequently, the field dependence of the dichroic contrast for P_3 and P_4 is directly proportional to the total magnetization of the array.

4.3.4 Determination of the nanomagnet contributions to the remanent magnetization

Method

The dichroic contrast of the Bragg peaks gives statistical information about the configuration of the magnetic moments and we show in this section how one can derive separately the remanent magnetization M_{r_1} and M_{r_2} of the two sublattices S_1 and S_2 from the intensities of the Bragg peaks P_1 to P_4 indicated in figure 4.12a. The procedure is as follow. First, we assume a distribution of the magnetic moments for which we simulate the scattering pattern. We then compare experiment and simulation characterized by values of M_{r_1} and M_{r_2}. We repeat the simulation until the best agreement is reached.

To evaluate equation (4.4), we need first a representation of the form factor of the nanomagnets. Here we approximate the shape of the nanomagnets with a cylinder of height $\mathbf{h}$ and an elliptical cross-section with semiaxes $\mathbf{a}$ and $\mathbf{b}$. The set of form factors $F_n(\mathbf{q})$ becomes [158]:

$$F_n(\mathbf{q}) = 2j_0(\mathbf{q} \cdot \mathbf{h_n}/2)\frac{j_1(\xi_n)}{\xi_n} \tag{4.8}$$

with

$$\xi_n = \sqrt{(\mathbf{q} \cdot \mathbf{a_n})^2 + (\mathbf{q} \cdot \mathbf{b_n})^2} \tag{4.9}$$

where j_0 and j_1 are spherical Bessel functions. As indicated in figure 4.8a, the structural unit cell contains two structurally identical nanomagnets, but with different orientations. Their respective form factors $F_1(\mathbf{q})$ and $F_2(\mathbf{q})$ are therefore given by the following sets of vectors that define their spatial orientation:

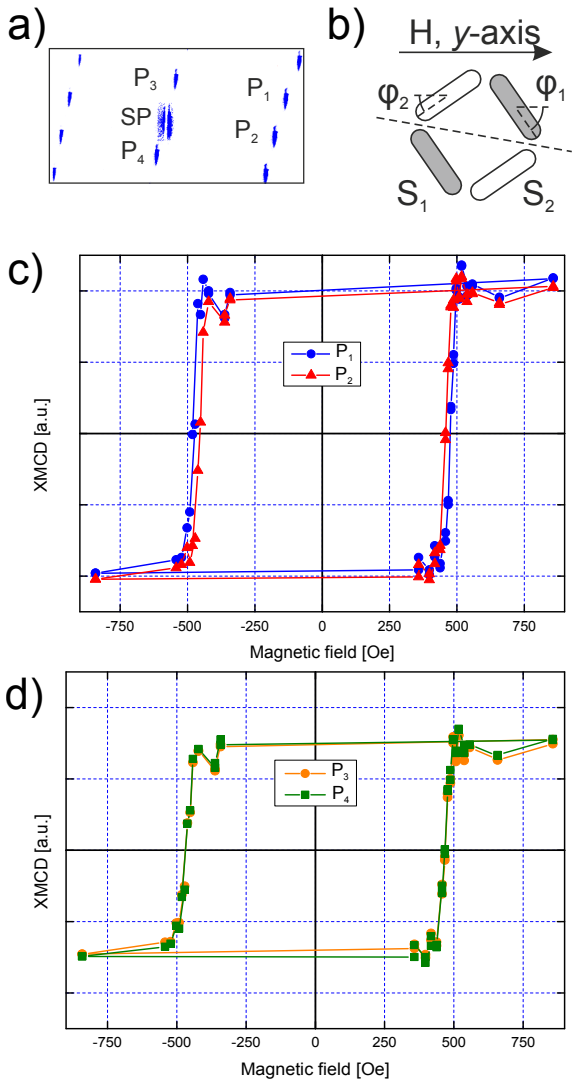


Figure 4.12: XMCD contrast of the selected Bragg peaks at remanence as a function of applied field. a) Scattering pattern indicated the selected Bragg peaks P_1 to P_4 (SP indicates the specular reflection). b) Illustration of the sample misalignment with respect to the direction of the applied field. Note that due to the misalignment the nanomagnets of the sublattice S_1 have a large angle relative (φ_1) to the applied field direction than the ones from S_2 (φ_2). c) XMCD contrast of the first order peaks P_1 and P_2. The two loops have different coercive fields, $H_{P_1} = 475 \pm 2$ Oe and $H_{P_2} = 455 \pm 2$ Oe, respectively. d) XMCD contrast of the second order peaks P_3 and P_4. Here, the two curves are identical within the experimental error, the coercive field is $H_{P_3} = H_{P_4} = 468 \pm 2$ Oe. [9]

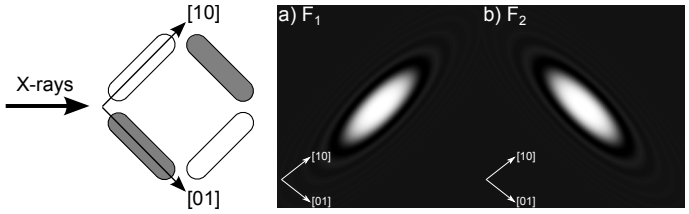


Figure 4.13: Form factors. We have computed equation (4.8) using the sets of vectors (4.11). F_1 is represented in panel a) and F_2 in panel b). Along [11], F_1 and F_2 are identical while along [10] and [01], they are not. Therefore, the Bragg peaks from the first order P_1 and P_2 will be sensitive to the magnetization of the individual sublattices, while P_3 and P_4 will be sensitive only to the overall magnetization.

$$\mathbf{a}_1 = \frac{230\,\mathrm{nm}}{2}\left(\frac{1}{\sqrt{2}},\frac{1}{\sqrt{2}},0\right), \quad \mathbf{b}_1 = \frac{80\,\mathrm{nm}}{2}\left(-\frac{1}{\sqrt{2}},\frac{1}{\sqrt{2}},0\right), \quad \mathbf{h}_1 = 1\,\mathrm{nm}\,(0,0,1) \quad (4.10)$$

$$\mathbf{a}_2 = \frac{230\,\mathrm{nm}}{2}\left(-\frac{1}{\sqrt{2}},\frac{1}{\sqrt{2}},0\right), \quad \mathbf{b}_2 = \frac{80\,\mathrm{nm}}{2}\left(\frac{1}{\sqrt{2}},\frac{1}{\sqrt{2}},0\right), \quad \mathbf{h}_2 = 1\,\mathrm{nm}\,(0,0,1) \quad (4.11)$$

We have set the relevant thickness of the nanomagnets to 1 nm in order to take into account that, due to the low penetration depth of soft X-rays at small grazing angles, the scattering signal originates within the context of the kinematic scattering approximation from the first few atomic surface layers only (section 4.2.1). The form factors of the two sublattices are shown in figure 4.13. We can see that along the [11] direction the form factors are identical, while they are different along [10] and [01]. P_3 and P_4 are therefore equally sensitive to the two sublattices, i.e., to the total magnetization. P_1 and P_2 on the other hand, are dominated by one of the two sublattices. Our procedure therefore consists of determining M from the second-order Bragg peaks and then vary M_1 and M_2 (while keeping the sum $M = M_1 + M_2$ constant) to reproduce the experimentally observed intensities.

In order to compare the experimental and numerical scattering pattern, the dichroic contrast measured (or simulated) at remanence after applying a specific field H has been normalized to the one measured (or simulated) at remanence following saturation. Hence for each Bragg peak we consider the normalized dichroic contrast $\mathcal{I}_{dic}(H) \equiv I_{dic}(H)/I_{dic}(H_{sat})$. This quantity can take the values between +1 and -1. Since the dichroic contrast of the second order peaks (either P_3 or P_4) is proportional to the total remanent magnetization M_r, $\mathcal{I}_{dic}$ at these peaks directly gives M_r normalized to the saturation value, $\mathcal{I}_{dic} = M_r/M_{sat} \equiv \mathcal{M}_r$. We can therefore determine $\mathcal{M}_r$ from the average of $\mathcal{I}_{dic}$ of peaks P_3 and P_4. This quantity takes the value of +1 (-1) when all moments are oriented towards the positive (negative) y direction.

The total magnetization is related to the fraction of nanomagnets N^- that have reversed their magnetic moments on application of a reverse magnetic field following saturation. We therefore have $\mathcal{M}_r = (N^+ - N^-)/N = 1 - 2N^-/N$, where N^+ is the number of nanomagnets that have not reversed their magnetic moments and $N = N^+ + N^-$ is the total number of nanomagnets. N^- (and N^+) can therefore be calculated from $\mathcal{M}_r$. The normalized dichroic intensity at the first order peaks (P_1 and P_2) is now determined by the distribution of N^- nanomagnets between the two sublattices S_1 and S_2, i.e., by the values of N_1^- and N_2^-, with $N^- = N_1^- + N_2^-$.

To derive these values we generate trial configurations varying N_1^- and N_2^- values and numerically compute the corresponding dichroic scattering patterns and compare them

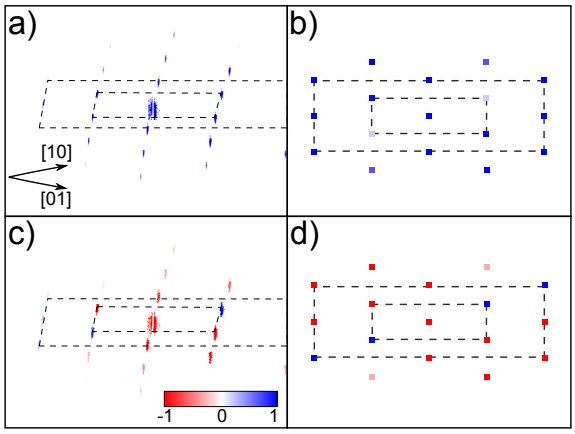


Figure 4.14: Comparison between experimental and numerical dichroic scattering patterns. (a) and (c) have been measured at applied magnetic fields of 480 Oe and -472 Oe, respectively. The corresponding calculated best-fit patterns are shown in (b) and (d). [9]

to the experimental data. This procedure is repeated until the best agreement for the asymmetry of dichroic intensity at P_1 and P_2 is obtained. We note that as long as N_1^- and N_2^- are identical but different arrangements of the magnetic moments in S_1 and S_2 are used, the simulated patterns are similar in their intensities within the simulation uncertainty.

Results

The numerical simulations reproduce quantitatively the dichroic intensity of the first and second order Bragg peaks, but we were also able to obtain qualitative agreement for the higher scattering order reflections. Two examples are shown in figure 4.14. The dichroic pattern in figure 4.14a was measured at remanence after application of a magnetic field of $H = +480$ Oe along the positive y-direction. The best agreement was obtained in figure 4.14b with 81% of the moments reversed on sublattice S_1 and 72% on sublattice S_2. The corresponding numbers for the simulation shown in figure 4.14d are 73% and 20% for S_1 and S_2, respectively, to reproduce the dichroic contrast shown in figure 4.14c which was recorded at remanence after applying an external field of $H = -472$ Oe.

We highlight that obtaining such insights within the magnetic configuration of S_1 and S_2 would not have been possible with a different technique such as MOKE which provides an averaged value of the magnetization without distinction of the different sublattices. These results are therefore a strong argument in favour of scattering for the study of such systems.

Discussion

When comparing experiment and simulation in more detail, one notes that significant differences appear for higher order peaks, even if the sign of the computed dichroic intensity is still correct for most of the observed peaks. We attribute this behaviour to following reasons.

Firstly, the higher scattering orders probe shorter length scales and are therefore more sensitive to details of the shape of the nanomagnets. This includes not only deviations from the assumed cylindrical shape, but also small variations in size, shape and microstructure between the nanomagnets themselves. Secondly, in our model we are assuming the nano-

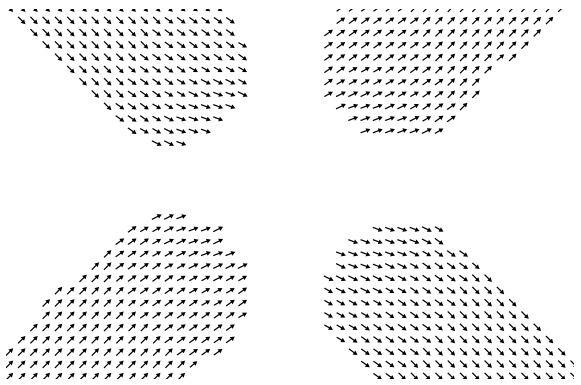


Figure 4.15: Micromagnetic simulation of a vertex at remanence following saturation. At the extremities of the nanomagnets, the magnetization curves to reduce the magnetostatic energy originating from the closest nanomagnets. As a consequence, the contribution to the form factor of these regions differs slightly from the rest of the nanomagnet. Note that this has been reported before by Rougemaille and co-workers [155].

magnets as macrospins. However, one has to expect the magnetization at the extremities of the nanomagnets to curve, in order to close the magnetic flux originating from the neighbouring nanomagnets at remanence. This behaviour is verified by the results of the micromagnetic simulation shown in figure 4.15. This angular dependence of the magnetization is not taken into account in the model. Thirdly, we note that our approach neglects the effects related to the refractive index, which give a modulation of the scattered intensity as a function of the direction of the reflected beam. This modulation is small close to the specular beam, but can be significant for higher order reflections. We note that for the determination of M_{r_1} and M_{r_2}, a quantitative agreement between simulations and experiments for the higher scattering orders is not necessary. And we thus take the "qualitative" agreement at high scattering orders as an additional validity of our model.

We remark that the above analysis is possible due to the misalignment between the sample axis and applied magnetic field (section 4.3.3). To illustrate this, we present in the figure 4.16 the simulated evolution of the dichroic intensity as function of the number of reversed magnetic moments N^- for two first order Bragg peaks. The right panel of figure 4.16a shows the case we have discussed so far, i.e. N_1^- and N_2^- are different. The case presented in figure 4.16b corresponds $N_1^- \approx N_2^-$, i.e., the same number of magnetic moments have been reversed in both sublattices, which corresponds to the situation when sample axis and magnetic field are parallel. We note that this latter case is difficult to realise experimentally due to the configuration of the diffractometer. Indeed, the sample is manipulated within the instrument using a long transfer arm (of length two meters) which makes it difficult to orientate the sample accurately.

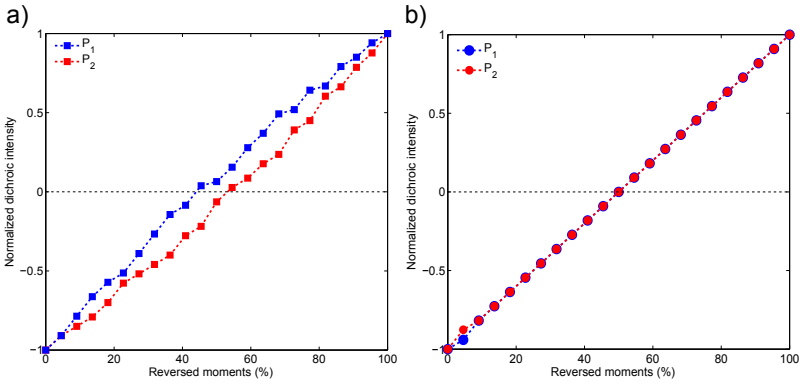


Figure 4.16: Simulated dichroic intensity as a function of number of reversed magnetic moments. Figure a) corresponds to the case for which $N_1^- \neq N_2^-$ and figure b) to $N_1^- = N_2^-$.

4.4 Diffuse scattering on an artificial kagome ice array

4.4.1 As-grown state

SXRMS measurements have been performed on artificial kagome ice in the as-grown state (figure 4.17). The kagome lattice and its orientation are shown in panel a). Similar to the square lattice, we can decompose the lattice into three sublattices comprising two nanomagnets, each oriented at 0, 60 and 120°, respectively, as indicated by the different colours in figure 4.17a. In the experiment, the sample was aligned such that the projection of the incident beam on the sample plane was oriented parallel to one of the three sublattices.

Description of the kagome lattice

The pattern recorded at a non-resonant photon energy (740 eV, above the absorption edge) is presented in figure 4.17b. Due to the absence of magnetic component in the scattering amplitude, this results from the charge scattering of the nanomagnets (section 3.1.2). The scattering pattern can thus be understood by taking into consideration the structure of the kagome lattice. Since it can be decomposed in three sub-lattices (figure 4.17a), the primitive cell contains one nanomagnets from each sub-lattice. It is repeated in space on a triangular lattice (red dots in figure 4.17a) with lattice parameter a. The Bragg peaks therefore form a hexagonal array with periodicity $4\pi/(a\sqrt{3})$. We have highlighted the first-order Bragg peaks by connecting them with a dashed lines. In contrast with the artificial square ice (section 4.3.1), we do not define the first diffraction order peaks as $h^2 + l^2 = 1$. This notation is not convenient here due to the six-fold symmetry of the system. Instead, we will refer to the directions in the scattering pattern. White arrows are drawn in the figure 4.17b to show the [10] and [01] directions. As we will describe in the following sections, the observed magnetic signals are related to one of these two directions.

Short-range ordering in the as-grown state

Because of the strong frustration in the kagome lattice (section 1.4.3), this system has a lower probability to reach a long-range ordered state even through thermalisation during metal deposition (section 1.4.2) [6]. Instead it forms a state with several small ordered regions of magnetic moments. This is shown in panel (c) of figure 4.17 by the PEEM picture recorded at the Fe L_3 edge (706.8 eV). One notes the absence of long-range ordering

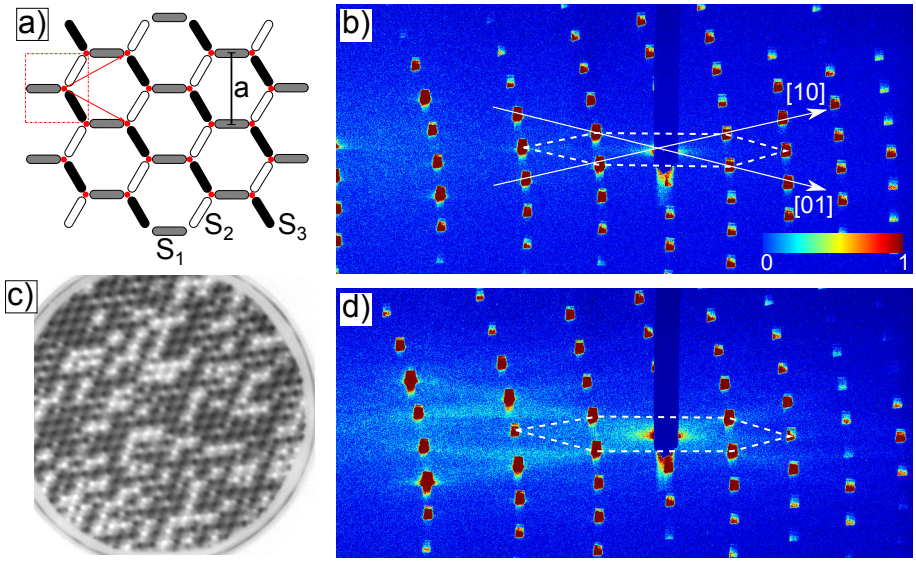


Figure 4.17: Artificial kagome ice in the as-grown state.a) Illustration of the kagome lattice. The primitive unit cell (red dotted square) is composed of three nanomagnets with different orientation (in black, white and grey). The two repetition vectors are indicated in red. b) Scattering pattern recorded above the Fe L_3 edge. Only structural information are obtained c) PEEM picture recorded at the Fe L_3-edge on an artificial kagome ice array in the as-grown state. Recorded at the PEEM endstation at beamline SIM, Swiss Light Source. (Courtesy of A. Farhan, *Paul Scherrer Institut*). d) Scattering pattern recorded at the Fe L_3 on a similar sample. No additional pure magnetic Bragg peaks are observed. Instead, diffuse scattering is found which indicates the presence of small ordered regions. In b) and d), first order Bragg peaks are highlighted with a white dashed box.

of the system. The scattering pattern shown in panel (d) has been recorded at the same photon energy on a similarly prepared artificial kagome ice sample. As expected, one does not observe additional pure magnetic Bragg peaks.

Instead, we can see a weak diffuse scattering signal. This originates from the disordered configuration of the magnetic moments as observed in the PEEM picture. As we will discuss below, it is possible to derive from the diffuse magnetic signal a statistic description of the disorder in the magnetization of the lattice as usually performed in small angle x-ray scattering (SAXS) [159] . This suggests that the as-grown state has no preferred direction for the magnetic moments (figure 4.17c).

4.4.2 First magnetization

We applied an external magnetic field on the as-grown sample parallel to the beam axis of stepwise increasing strength. After each step, we recorded the scattering pattern at remanence (figure 4.18). When the field is increased from 0 G to 1000 G, the intensity of the diffuse signal decreases until it disappears when the sample's magnetization is saturated. This evolution reflects the magnetic ordering of the system. Starting from a state with short-range correlations (figure 4.17c), we gradually reverse the magnetic moments in the direction of the external field, thus increasingly ordering the system. At saturation, the system is fully ordered with all the moments aligned along the field direction. As in the artificial square ice, the magnetic and structural primitive cell are equivalent and no

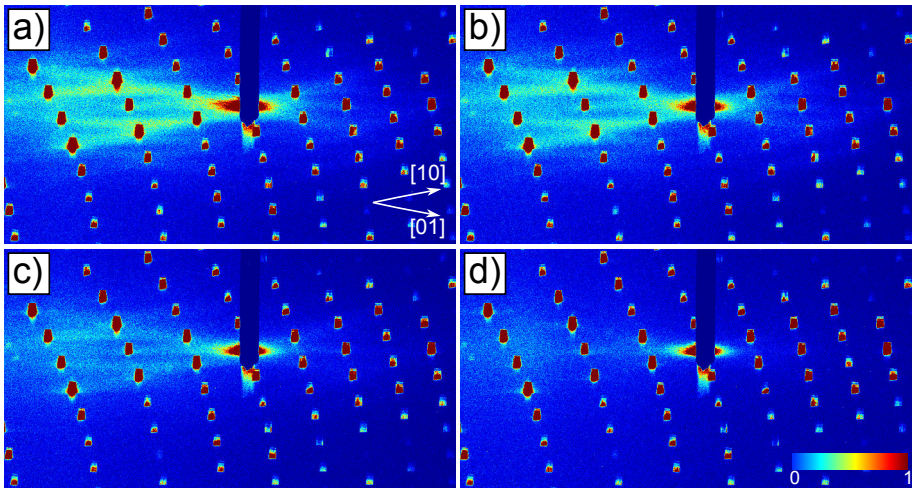


Figure 4.18: Evolution of the scattering pattern during the first magnetization. On-resonance scattering patterns recorded at remanence after applying a field of a) 0G, b) 500 G, c) 750 G and d) 1000 G (saturation).

additional magnetic Bragg peaks are present in the scattering pattern.

The diffuse scattering remaining on the left of the scattering pattern in panel (d) is also observed off resonance (figure 4.18a). It is not related to the magnetic properties of the system, but must originate from structural imperfections.

One notes that both magnetic and non-magnetic diffuse scattering are observed only on the left of the scattering pattern and not on the right. We believe that due to geometrical effects combined to the low intensity of the diffuse scattering, the detection is possible only at small scattering angle (left of the detector) but not at high angle (right).

4.4.3 Field dependency of the diffuse scattering

In the literature, one encounters the term "Dirac strings" which describes short-range ordering in artificial spin ice. It refers to the presence of chains of reversed magnetic moments in a saturated background, which connect non-zero magnetic charges (section 1.4.3). These chains can be nucleated with an external magnetic field; recent experiments indicated that they also appear during the relaxation process of thermally activated systems [61]. In the first case, the growth of the string can be controlled by additional parameters such as the angle between the lattice and the magnetic field and/or the nanomagnets can be tailored with modified anisotropies to allow the control of the nucleation of the strings [52, 69].

Acting as local deviations from the perfectly ordered state, we expect Dirac strings to induce variations in the scattering pattern, namely, the appearance of diffuse scattering in-between the Bragg peaks. We recorded the changes of the diffuse scattering as a function of the magnetic field. We present in figure 4.19 four scattering patterns recorded at remanence. Two (a and c) have been recorded after applying a saturating field and the two others (b and d) at values close to the coercitivity. These points are indicated on the hysteresis loop recorded on the specular peak.

We first look at the scattering patterns recorded on the saturated lattice (figure 4.19 a) and c)). We observe no diffuse scattering. This is in agreement with the alignment of all magnetic moments in the same direction with an external field. Indeed, in this case, all the magnetic moments are aligned with the magnetic field, similar to the case of artificial

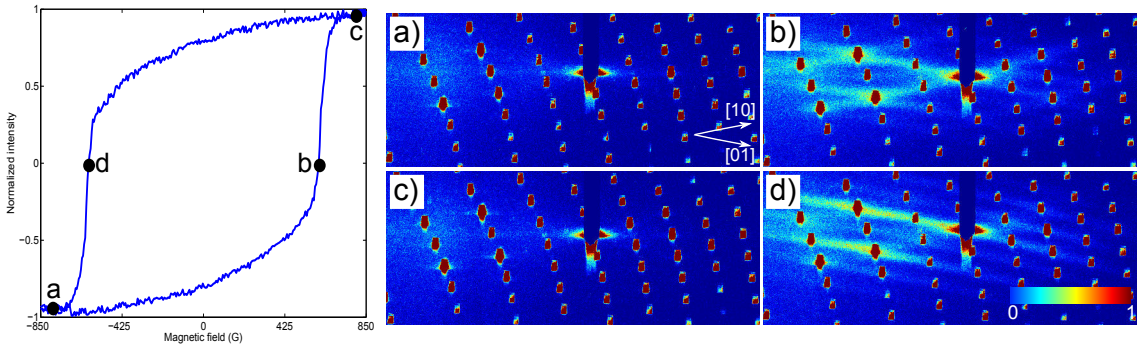


Figure 4.19: Diffuse scattering during magnetization reversal. On the left side is the hysteresis loop recorded at the specular position using the photodiode installed in the RESOXS diffractometer. On the right are four scattering patterns recorded at remanence after applying the fields indicated by the points on the hysteresis loop.

square ice (section 4.3.3); the primitive structural and magnetic unit cells are identical (figure 4.23a). As a consequence, only Bragg peaks are observed, synonymous with long-range correlations in the system. One can note a brighter background on the left side of the scattering pattern presented in panel (d).

Panels (b) and (d) exhibit additional diffuse scattering. In (b), the diffuse scattering is similar to the one in the as-grown state, namely diffuse scattering along the [01] and [10] directions resulting in a cross shape. However, in (c), the diffuse scattering is only along the [10] direction, indicating that Dirac strings are nucleated and grown in only one direction. This is inconsistent with a magnetic field applied parallel to the beam axis, for which no direction is favoured [52]. It could however be explained by a tilting of the direction of the applied field during the field sweeps. We note that this may indeed be the cause, since the field is applied in our experiment using an electromagnet composed of two sets of coils. If they had ay different H(I) behaviour, this could give rise to a tilt of the effective applied field.

From PEEM measurements, we know that the growth of the Dirac strings can be biased in one direction by applying an external magnetic field at an angle relative to the sublattice [52]. We performed the same type of experiments by applying an angle of 5 degrees. For similar values of the magnetic field, we observed a change in the diffuse scattering (figure 4.20). When no tilt is applied (panel a), the diffuse scattering forms a cross, indicating that Dirac strings are developed along both [10] and [01]. When the tilt is applied (panel b), the diffuse scattering evolves in a line-shape along [01], indicating that Dirac strings grow preferably along one direction. This observation is coherent with the information recorded by PEEM [52, 69], and thus supports our above explanation.

We next discuss whether quantitative or at least qualitative information can be retrieved from the diffuse scattering in the scattering pattern by the use of simulations. To simulate the effect of an applied field on a kagome array, we calculated several configurations by changing randomly the number and length of Dirac strings. We then computed the scattering pattern using the method discussed before (section 4.2). In figure 4.21, we show three simulated patterns corresponding to different length or number of Dirac strings in a kagome lattice. Despite the pixelation of the patterns due to the limited number of objects, one notes that shape and intensity of the diffuse signal is related to the number and/or length of the strings. When the number of chains increases but their length is kept constant, the signal broadens. When the number of chains is kept constant and the length of the chain increases, the signal tightens. Note that this is the expected relationship as

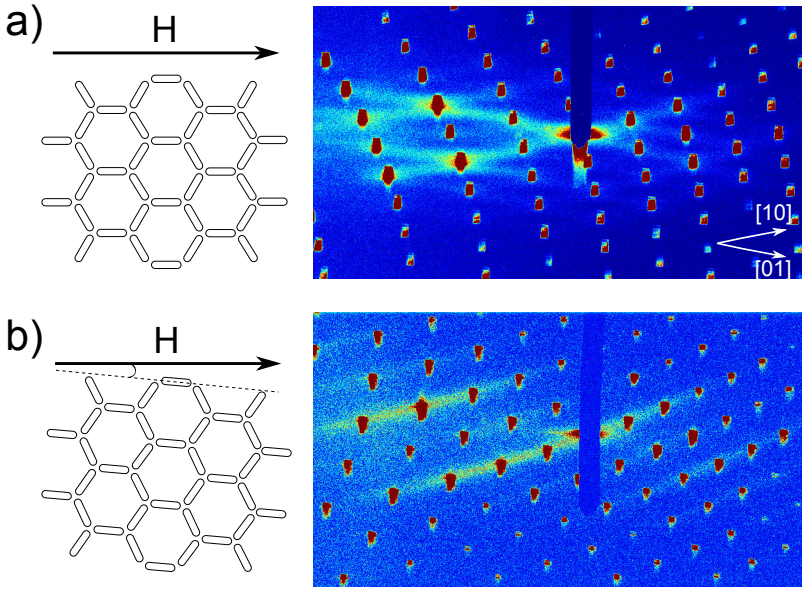


Figure 4.20: Effect of the angle between external magnetic field and kagome lattice. Scattering pattern a) has been recorded at remanence after a field has been applied parallel to one of the sub-lattices. In the case of the scattering pattern b), an angle of 5 degrees was used between field and axis.

observed and exploited in SAXS. We can thus expect to retrieve the statistical description of the sample, i.e. the form, the length and the number of objects.

In particular, the simplest information to retrieve is the direction(s) of nucleation and growth of the Dirac strings. The simulations shown in figure 4.21 have been obtained with strings grown along the [01] direction in real space, i.e. reversal of the magnetization of nanomagnets in the S_1 and S_3 sub-lattices (figure 4.17a). Correspondingly, the resulting diffuse scattering is oriented along the [10] direction. In analogy, for the chains grown along [10] (S_1 and S_2), the diffuse scattering appears along the [01] direction. From these observations, we can conclude that the presence of cross-shaped diffuse scattering (figure 4.17b) indicates short-ranged ordering along the two directions in real space. This indicates that no direction is favoured during sample deposition, which is what we also observed by PEEM (figure 4.17c).

4.4.4 Analysis of the diffuse scattering : difficulties and solutions

As discussed above, the diffuse scattering contains information about the short-range ordering in the system. To extract quantitative information, our approach is to cut a profile through a 2D scattering pattern (figure 4.22). For the scattering pattern in panel (a), this produces a profile with three peaks as shown in panel (b). We fitted each peak with a Gaussian function in order to get the full width at half maximum (FWHM) and the intensity of the peak. We present in panels (c) to (f) of the figure the evolution of the FWHM and of the peak intensity for both, simulation (c and e) and experiment (d and f). One notes that no good agreement is reached for the FWHM. On the other hand, the intensity shows a qualitative agreement. It increases until reaching a maximum then decreases for both experiment and simulation.

The main difficulty to obtain quantitative information is the convolution of the diffuse scattering with the beam size and divergence. This limits the achievable resolution on the

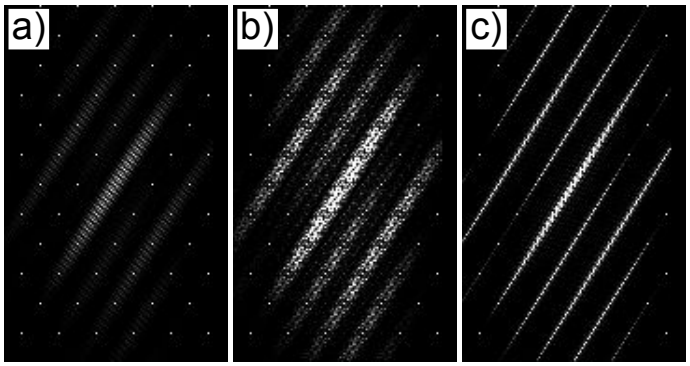


Figure 4.21: Simulated scattering patterns for different Dirac strings. Between the three scattering patterns, the number and length of the Dirac strings. For (a), there are 3 Dirac strings of 5 nanomagnets, for b) 12 strings with 5 nanomagnets and c) 3 strings with 17 nanomagnets.

detector, the diffuse scattering is "blurred". The experimental reason for this is that we needed to defocus the beam to spread out the Bragg peaks on several pixels. It prevents saturation of the CCD camera and thus allows the detection of the diffuse scattering.

To overcome this limitation in future experiments, we see as one option the use of a continuous film of Permalloy, which are magnetic only at the positions of the nanomagnets. There should be only magnetic scattering and no charge scattering, hence the diffuse scattering should be easier to record. As a second option, one could use a mask to hide the Bragg peaks, therefore being able to accumulate more photons on the CCD chip. As a third option, we also consider defocusing the beam in only one direction, here in the vertical direction, to get a better spatial **q** resolution in the other direction.

4.4.5 Evolution of the dichroic contrast during magnetization reversal

We also recorded the dichroic scattering pattern for several applied magnetic field. As in the case of artificial square ice, we wanted to get insights in the magnetization of each of the three sublattices of the kagome array as a function of the applied magnetic field [9].

At saturation, magnetic and structural unit cells are identical (figure 4.23a). The scattering pattern from panel (b) of the figure has been simulated for the configuration shown in the figure. All Bragg peaks show the same (red) dichroic contrast but the peaks $(1\,1)$ and $(\bar{1}\,1)$ have opposite (blue) contrast. We believe that this is for the following reason: along the beam axis (horizontal), the projection of the magnetic moments is ferromagnetic for each nanomagnet. In the direction perpendicular to the beam axis (vertical), the projection is however antiferromagnetic. Therefore, the projections of the magnetic moments on the beam axis are not equivalent in both directions, and this brings change of the dichroic contrast.

When we look at the experimental result (figure 4.23c), we do not retrieve this behaviour. Instead, all Bragg peaks owns the same (red) dichroic contrast. A possible explanation might be the presence of a remanent field originating from the electromagnet. To overcome this limitation in future experiments, we see as an option to remove the coils of the diffractometer after saturating the sample to observe whether or not experimental data can match simulation for the saturated state. It is however still not clear to us that this explanation is the only responsible for this difference between experiment and simulation. Another option could be a slight misalignment between the beam axis and the

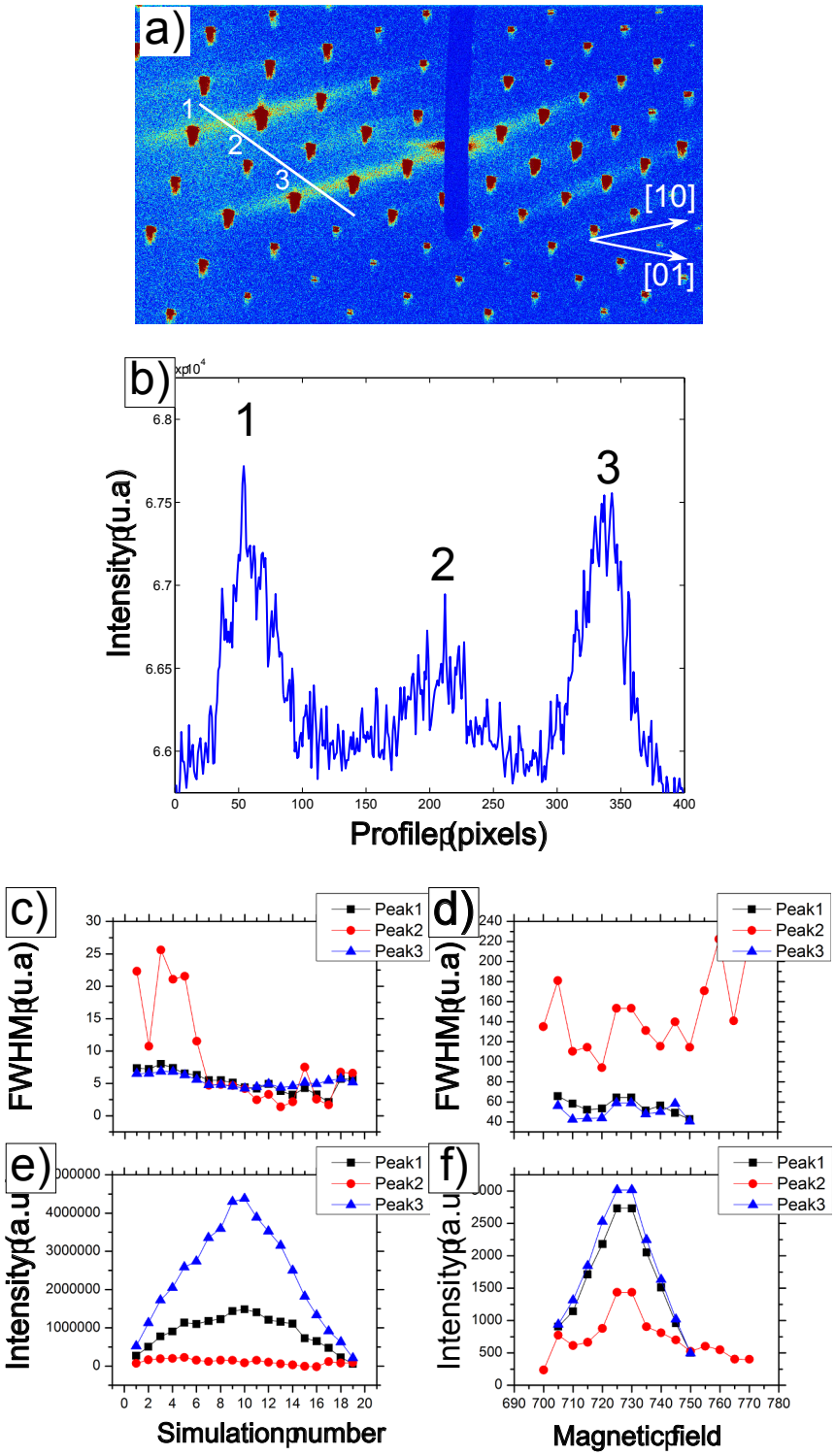


Figure 4.22: Analysis of the diffuse scattering. Profile in panel b) corresponds to the while line in the scattering patterns in panel a). The profile presented as an example is including three diffuse lines which corresponds to three peaks. They have been fitted using Gaussian functions. From these fits, we reported in the panels c) and d) the full-width at half-maximum and in the panels e) and f) the maximum intensity for both experiments (d and f) and simulations (b and e). No agreement is reached for the full-width at half-maximum, but a qualitative agreement is reached in the intensity (see text).

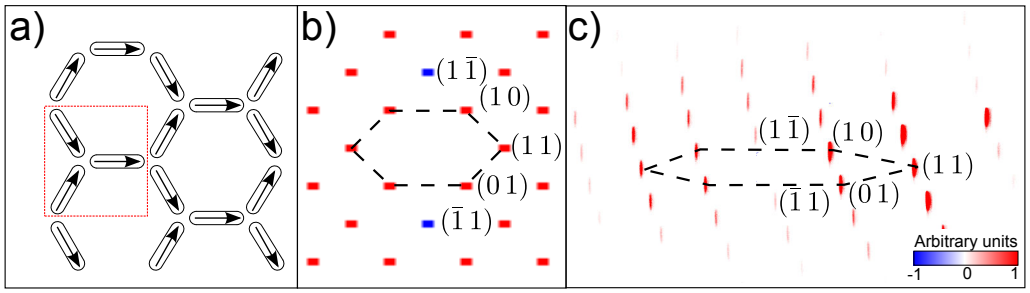


Figure 4.23: Artificial kagome ice saturated (a). We are comparing simulation (b) and experiments (c). There are agreements for all Bragg peaks but the peaks $(1\,\bar{1})$ and $(\bar{1}\,1)$. Origin of the two blue peaks in the simulation are described in the text. In the experiments, the remanent field is so strong that it dominates over the shape anisotropy, and all magnetic moments are forced to be parallel to the magnetic field.

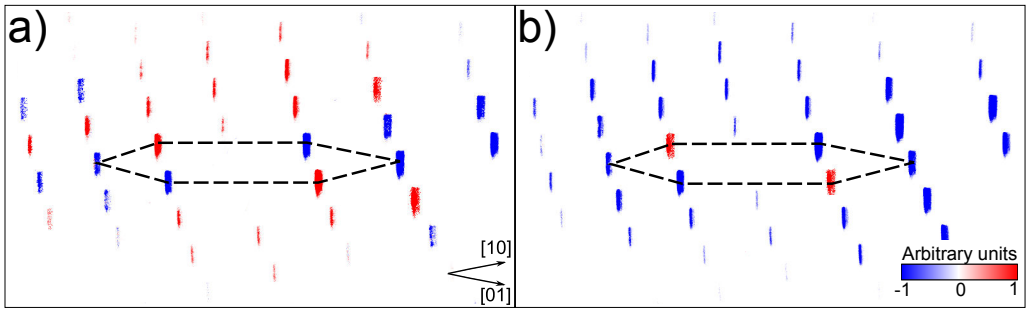


Figure 4.24: Dichroic scattering patterns recorded on the same branch of the hysteresis. The spectra have been recorded at a) 300 G and b) 350 G. We observe an inversion of the dichroic contrast, in a similar way as for the artificial square ice.

sub-lattice, in a similar manner such as the one encountered in the case of artificial square ice (section 4.3.4). More investigations are thus required to bring a clear explanation.

During reversal of the magnetization, we observe an inversion of the dichroic contrast. As an example, we show in figure 4.24 the dichroic scattering patterns recorded at consecutive points on the hysteresis loop. We applied the same procedure to analyse these data as in the case of the square lattice (section 4.3.4). We remind the reader that the first step was to match the higher-order peaks of experiments and simulations because they are sensitive to the overall magnetization state of the sample, then we refine to reach agreement for the first-order peaks. Here, in all the simulations performed, we always find an opposite behaviour for the peaks $(1\,\bar{1})$ and $(\bar{1}\,1)$ between experiments and simulations. In the current state, we are only able to reach agreement for the first-order peaks, which is not enough to bring significant information, mostly because of the higher symmetry of the kagome lattice compared to the square lattice which makes it more sensitive to misalignments.

We also rotated the sample with respect to the magnetic field direction to observe how the dichroic scattering evolves when the Dirac strings grow in a defined direction, for example, along [10]. For this, we rotated the sample by 7° degrees with respect to the magnetic field direction. We were thus able to favor the nucleation of Dirac strings along the same sublattices as when the angle is set to 5°, as demonstrated by PEEM imaging [52]. In figure 4.25, two scattering patterns recorded at successive steps of the magnetization protocol are presented. Similar to the not-tilted case, we observe a step-by-step reversal of the dichroic contrast. What is interesting to note is that the inversions seems to occur

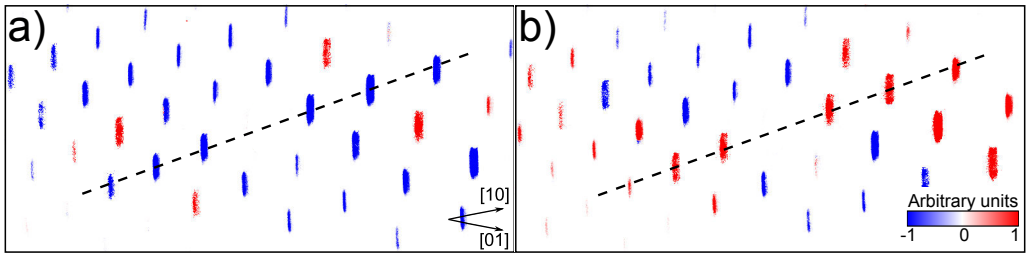


Figure 4.25: Dichroic scattering pattern recorded with a tilt of 7 degrees. a) and b) are successive measurements, at -600 G and -650 G respectively.

in the same direction [01] where the diffuse scattering is observed (figure 4.20b). We can relate this evolution to the following scenario. First, Dirac strings are nucleated and growth along specific sublattices. They are deviate from the perfect ordered state on a short-range which are then providing diffuse scattering in the scattering pattern. When these strings are long enough,i.e., when enough magnetic moments in the sublattices have been reversed, this involves a change in the dichroic contrast similar to what we observed for artificial square ice (section 4.3.3). To confirm this hypothesis, additional measurements are required during which both diffuse scattering and dichroic pattern will be measured at the same time. We could thus get information during the magnetization reversal on the whole illuminated area which is larger that what can one observe using real-space microscopy.

4.5 Summary

In this chapter, we have presented the results of our soft x-ray resonant magnetic scattering experiments performed on artificial spin ice arrays. These experiments have been carried out in reflection to be sensitive to the in-plane magnetization of the nanomagnets. The use of a CCD camera has allowed us to obtain an extended view of the reciprocal space.

Large ground-state ordering in the as-grown state of artificial square ice was observed which gives rise to pure magnetic Bragg peaks. Their magnetic origin was additionally confirmed by saturating the sample, which destroys this ground-state ordering and the magnetic peaks disappear. We followed the evolution of the magnetic state in the sample. Experiments have been compared to simulations, which are based on kinematic theory of x-ray diffraction. This comparison proved to be important for a better understanding of the scattering pattern. By considering the nanomagnets as cylinders, experimental features up to the third diffraction order have been reproduced successfully. Micromagnetic simulations indicated that nanomagnets' magnetization at the ends of the nanomagnets rotates out the nanomagnets' axis to close the magnetic flux originating from the nearest neighbours.

Diffuse scattering in artificial kagome ice gives insight in the short-range organisation of the system. We showed with simulations that chains of reversed magnetic moments, generally referred to "Dirac strings", can be the origin of this signal. However, due to experimental parameters related to the beam defocusing, it was not possible to quantitatively analyse this measurements. We propose that discrepancies between experiment and simulation may be due to a remanent field of the magnetic coils. This hypothesis will be verified in our next experiments.

Chapter 5

Complementary studies

Contents

5.1 Induced disorder in artificial square ice 86
5.2 Temperature dependence of the scattering pattern 87
5.3 Summary 89

Complementary to soft x-ray resonant magnetic scattering (SXRMS) on nanomagnets with frozen moments, we have explored additional ways to study the magnetic properties of artificial spin ice. In this chapter, we present and discuss the results, which are often preliminary.

Nanomagnets with static moments have been used in the first section. The work presented in this section involves tailoring of structural defects in artificial square ice lattices. It shows nevertheless the same magnetic properties as the perfect lattice in the as-grown state.

The last section is dedicated to dynamical studies, with the use of superparamagnetic nanomagnets at room temperature. We present very recent SXRMS measurements performed on this type of system to follow the evolution of the scattering pattern as a function of the temperature.

5.1 Induced disorder in artificial square ice

Following the idea of Hügli and colleagues who studied a modified artificial kagome ice [69], we induced disorder in an artificial square ice (figure 5.1). For this we introduced soft (blue) and hard (red) nanomagnets in the lattice, in order to use them as start and stop islands for the growth of Dirac strings. Our goal is here to use such an array to find how to extract quantitative information from the scattering pattern about the Dirac strings. In addition, we intend to study memory effects of the system. Two examples of memory effects are return point memory and complementary point memory [160]. The first corresponds to the return of the system in the same microscopic configuration after completing a hysteresis loop. The second is the inversion of the symmetry of the magnetic domains at two opposite points of the hysteresis. A theoretical work predicted that increasing the disorder in artificial spin ice leads to an increase the memory of this system [161].

We present in figure 5.2 the scattering patterns recorded in the as-grown state as well as after applying a saturating field of 1000 G; both scattering patterns have been recorded at the Fe L_3 absorption edge. Similar to the "normal" artificial spin ice, we observe magnetic Bragg peaks located between structural Bragg peaks (figure 4.8). This indicates that, despite the introduction of softer and harder islands, the system is organizing as the unperturbed one with type I vertices during sample growth.

One notes in the scattering pattern also additional Bragg peaks, which appear with a smaller periodicity in the reciprocal space. These are also present after saturating the sample (figure 5.2b), as well as on- and off-resonance. Their origin can be related to the two periodicities induced by the presence of soft and hard nanomagnets in the system. Indeed, these tailored defects have been introduced in the square lattice with a larger periodicity compared to the lattice parameter, meaning a smaller distance in **q**-space.

Disorder in the magnetic organisation should lead to the observation of diffuse scattering, as we already observed for artificial kagome ice (section 4.4). It is not the case here as no diffuse scattering is observed. We can conclude that it was probably too weak to be observed. Careful optimizations of the lattice and experimental set-up could lead to detection of this signal and thus to learn about the Dirac strings in the lattice.

We recorded the scattering patterns at each step of the magnetic field with both right- and left-handed circular polarized light. As we saw in the section 4.3.3, the dichroic contrast contains statistical information about the magnetic organization in the square sub-lattices. This could not be the solution for the study of memory in artificial spin ice, where one is more interested in the local organization. An other scattering technique could however be useful for this purpose. This is coherent x-ray speckle metrology [162]. It has already been

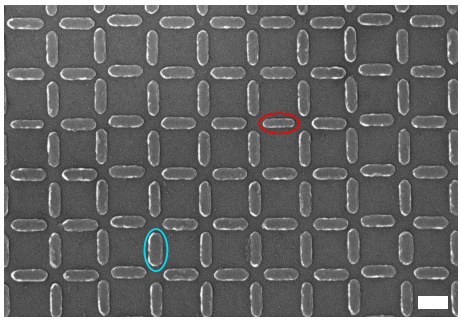


Figure 5.1: Induced disorder in artificial square ice. In an array of nanomagnets (230 × 80 nm), we have introduced periodically softer (200 × 80 nm, blue circle) and harder nanomagnets (200 × 40 nm, red circle). The scale bar (in white) represents 200 nm.

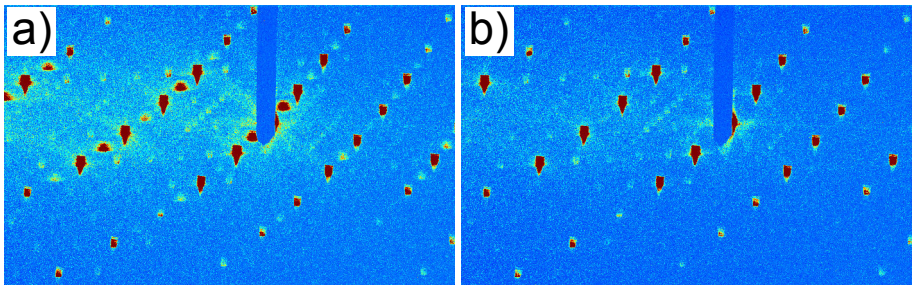


Figure 5.2: Effect of induced disorder on the scattering pattern. a) has been recorded in the as-grow state and b) after applying a saturating field (1000 G). Both scattering patterns have been recorded at 706.5 eV.

applied to memory effects in thin magnetic films [160]. In a forthcoming experiment, we intend to apply it to the case described in this section.

5.2 Temperature dependence of the scattering pattern

We intend to employ soft x-ray magnetic scattering (SXRMS) to confirm data obtained by L. Anghinolfi and co-workers using muon spin rotation (μSR) [163]. Indeed, thanks to the element specificity of this technique, one can rule out artefacts arising from other components of the sample. We performed such experiments using the RESOXS diffractometer located at the SIM beamline of the Swiss Light Source. The experiments which we will present in this short section have been performed end of March 2014, and only preliminary results are presented here, much further analysis and simulations are required to fully understand this set of data.

We used an array of nanomagnets similar to what has been used in ref. 163. Using the cryostat of the diffractometer and in the absence of any static magnetic field, we followed the evolution of the scattering pattern with the temperature. We cooled the sample below 20K which is lower than the transition temperatures expected from μSR measurements [163]. The evolution has been measured with a photodiode as no 2D detector was available at this time; five rocking curves are presented in figure (figure 5.3). There is no clear difference between the theta scans; the only observation is the disappearance of the oscillation located at $\theta = 11°$. At this stage, we cannot give a definitive explanation due to the limited amount of reciprocal space covered by the photodiode. This oscillation

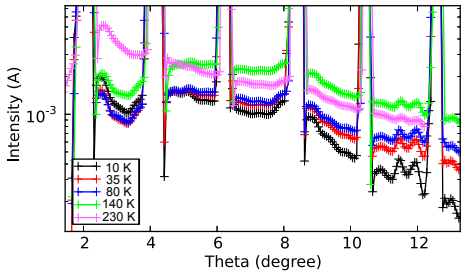


Figure 5.3: Evolution of the scattering pattern with the temperature. We measured part of the reciprocal space using a photodiode at several temperature. No strong difference has been observed, but one oscillation at 11 degrees disappears when the temperature increases. At this early stage, the interpretation of the results is not straightforward.

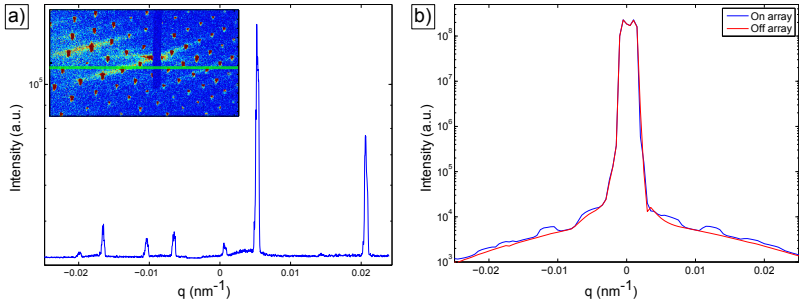


Figure 5.4: Comparison between 2D and 1D measurements. a) is the profile along the green line of the 2D scattering patterns in insert. We have integrated over 20 pixels (roughly to 200 micrometres in real space) to compare with b) which has been recorded with a photodiode with a front slit of the same size. The features present in both a) and b) correspond to Bragg peaks located at different positions in the second dimension, and the diffuse scattering cannot be distinguished from the background in both cases.

could be related to diffuse scattering indicating an ordering in the system, ideally to one of the two magnetic phase transition expected. But it could be also a Bragg peak close to the scattering plane. Indeed, the diode has a rather large vertical slit in front of it. One might expect the position of the sample to move slightly when the sample is cooled, therefore displacing the Ewald's sphere at the same time.

To illustrate this point, we compare a profile from a scattering pattern in two dimensions (figure 5.4a) with a theta scan performed using the photodiode (figure 5.4b). The large integration area is problematic as it records Bragg peaks located at different positions in the second dimension, providing more peaks on the spectrum. We prove that the features observed in the figure 5.4b are related to Bragg peaks by comparing this scan (black line) with an other one performed out of the sample array (red line). Moreover, the diffuse scattering cannot be distinguished from the background in the profile due to the limited dynamical range of the CCD camera (section 4.4.4). We therefore cannot be sure whether what is observed using the photodiode might be related to the diffuse scattering. Nevertheless, the higher dynamical range of the photodiode should allow one to measure this signal. This would however require using a pinhole in front of the diode to limit the amount of reciprocal space recorded at once. It also underlines that observing the scattering pattern in two dimensions instead of one really facilitates the interpretation of the scattering pattern.

5.3 Summary

In this final chapter, we have preliminary results obtained by complementary experimental techniques on new systems. This shows that the study of artificial spin ice is neither limited to real space measurements nor to the classical configurations studies.

Study memory effects in artificial spin ice could be performed by inserting tailored defects. To fully explore the properties of this system, using a coherent beam would be a natural evolution.

Magnetic transitions in artificial kagome ice have been confronted with 1D soft x-ray magnetic scattering. This technique does not bring so much about this problem due to the limited portion of reciprocal space available.

Chapter 6

Conclusion and outlooks

6.1 Summary and conclusions

In this thesis, we tried to evaluate whether soft x-ray resonant magnetic spectroscopy (SXRMS) can be used as a tool to probe the magnetic properties of artificial spin ice. The two dimensional arrays have been mainly studied by real-space microscopy, which present limitations in accessing long distances and short time scales. Scattering methods, on the other hand, have the potential to overcome these restrictions.

In chapter 1, we have described two types of artificial spin ice, the square and kagome ice. As observed in the literature, their magnetization states are rather complicated to describe, because of the strong degeneracy induced by the magnetic frustration (section 1.4).

Artificial spin ice is fabricated by lithography processes, which are described in chapter 2. We demonstrate that in such processes, all steps depend on each other, with the lift-off step the most critical. Choices of resist, material deposition and their impact on the lift-off step have been discussed. We also discussed the control of the sizes of the nanomagnets. By modulating the shape and the dose, we managed to produce nanomagnets as small as 60 nm $\times$ 20 nm over areas as large as 1.5 cm $\times$ 1.5 cm. These nanomagnets are composed of in-plane magnetic materials such as Permalloy ($Ni_{80}Fe_{20}$) capped by a layer to prevent oxidation. Magnetic characterization of these nanomagnets showed that they can be described as a single magnetic domain (section 1.4.1), while scattering results and micromagnetic simulations suggest a more complex magnetic structure at the ends of the nanomagnets (section 4.3.4).

The choice of SXRMS is relevant in the case of artificial spin ice because of the compatibility of the photon wavelength with the typical sizes of these systems. Moreover, it presents a high sensitivity to magnetism due to the strong XMCD effect found for absorption and scattering in this energy range (section 3.1.2). The measurements are done in the reciprocal space (section 3.2), which provides statistical information about the state of the magnetization in the system.

Such nanomagnet arrays have been studied with SXRMS (chapter 4). The reflection geometry provided sensitivity to the in-plane magnetization. Using a CCD camera, we obtained an extended view of the reciprocal space. To interpret in detail the information contained in the scattering pattern, we developed a 2D model based on the kinematic theory of x-ray diffraction (section 4.2.2). For both, artificial square and kagome ice, the observation of high order Bragg peaks demonstrated the high degree of order of these metamaterials. We could furthermore observed magnetic signals originating from short- or long-range ordering in the artificial spin ice arrays.

Bragg peaks of magnetic origin have been observed in the as-grown state of artificial square ice (section 4.3.1). Their origin is related to the organization of this state in large domains of type I vertices, which corresponds to the antiferromagnetic alignment of neighbouring vertices. We also demonstrated that following the evolution of the XMCD contrast of the Bragg peaks allows to retrieve statistical information about the magnetic organization in the system (section 4.3) [9]. With very simple statistical models, we obtained good agreement in the case of the artificial square ice for low diffraction orders. For higher orders, we observed quantitative discrepancies between experiment and simulation, this related to more complex magnetization of the nanomagnets (section 4.3.4). Micromagnetic simulations indicated that they cannot be considered as simple macrospin, because the magnetization can rotate at each end of a nanomagnet, out of the easy axis.

The sensitivity of the CCD camera allowed the detection of diffuse scattering in artificial kagome ice (section 4.4). Based on real space imaging and simulations, we attribute this to the establishment of short-range magnetic ordering in the system, referred in the literature as "Dirac strings". This signal is reproducible, and can be directed by an angle between the lattice and the magnetic field (figure 4.20). The analysis of this signal is however more complicated than for artificial square ice. The lower symmetry of the system as well as choices in the experiment parameters are limiting our ability to further exploit the signal. Only qualitative information about the direction of nucleation and growth of the "Dirac strings" has been obtained despite knowing that information are encoded in the diffuse scattering as observed in the simulations (figure 4.21).

Additional studies have also been performed to explore the properties of artificial spin ice. Tailored disorder has been introduced in artificial square ice to control the size of the "Dirac strings" (figure 5.1). Introducing defects in a periodic way brought new Bragg peaks in the scattering pattern. The array exhibits the same magnetic behaviour in the as-grown state as the regular system.

To conclude, on one hand, scattering provides insight in the magnetic ordering of the artificial square ice, both at short- and long-range. On the other hand, interpretation of the scattering patterns is not straightforward and requires the elaboration of theoretical models. Choices of experimental parameters for the acquisition of patterns is also of high importance. We thus have to leave our initial question open and can only state that SXRMS has indeed strong potential but that further development are required.

6.2 Outlooks

Most of the experiments carried out through this thesis have been performed on nanomagnets with static magnetic moments at room temperature. However, recent advances have enabled the fabrication of superparamagnetic nanomagnets [70, 74, 84]. The time scale of the fluctuations have however prevented microscopy techniques to reach dynamics ranges of interest. Scattering techniques could thus be the tool of choice to study such fluctuations on shorter time scales. The work carried out in this thesis could be seen as a first step towards the dynamics of artificial spin ice with nanomagnets with fluctuating magnetic moments.

Improvements in both sample preparation and experimental set-up have been made since the early results of SXRMS on thermally activated artificial spin ice (section 5.2). Artificial spin ice arrays can now be produced on silicon nitride membrane, thus enabling experiments in transmission geometry. The proof of principle is shown in panel a of figure 6.1.

One notes the small size of the Bragg peaks which are focused on few pixels. This

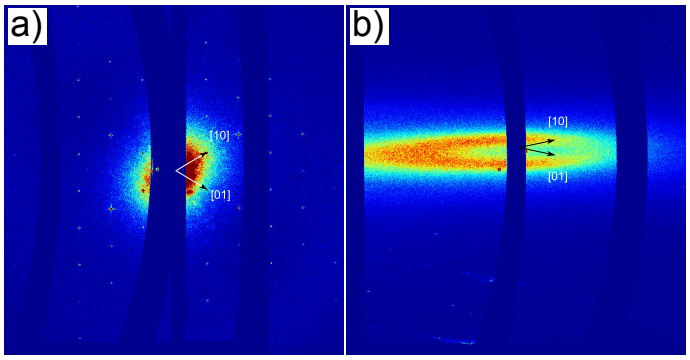


Figure 6.1: 2D scattering patterns on thermally activated artificial spin ice. Experiments were carried out on a kagome arrays with nanomagnets of size $60\times20\times3$ nm^3 (section 5.2), respectively. Scattering pattern in panel a) has been recorded in transmission geometry with an array produced on a silicon nitride membrane. One notes the small size of the Bragg peaks due to the beam being focused at the sample position. In b), the scattering pattern has been obtained in reflection geometry. The use of a mask in front of the CCD camera hides the Bragg peaks, thus allowing the recording of the diffuse scattering. Realisation of the mask by Dr. V. Scagnoli, and sample produced by O. Sendetskyi, *Paul Scherrer Institut*.

limits the acquisition time of the CCD camera. One solution which we have used in all the experiments carried out at the Synchrotron SOLEIL is to defocus the Bragg peaks on several pixels (chapter 4), thus decreasing the intensity per pixel. During experiments carried out at the Swiss Light Source in June 2014, we used a mask to hide the Bragg peaks (figure 6.1b). Using this alternative solution, we observed the diffuse scattering and its dependence with temperature. The results are still under investigation, but it is nevertheless a good news for future experiments.

X-ray photon correlation spectroscopy (XPCS), an advanced x-ray scattering technique, has been developed since the advent of x-ray sources with a coherent beam of sizeable intensity (figure 6.2) [164]. This beam is used to coherently illuminate the sample, resulting in a scattering pattern composed of intensity speckles. The origin of these speckles is the constructive and destructive interference of the coherent radiation scattered from the elements of the sample, which in our case are the magnetic islands. Since the arrangement of the individual scattering objects is preserved in a speckle pattern, changes in the magnetic order will be reflected by variations of the speckle intensities. Following these intensity variations in real time thus yields a statistical description of the fluctuations in terms of the characteristic time and length scale dependence, but also gives an indication of the nature of the fluctuations [165]. We remark that so far XPCS has primarily been used in the hard x-ray regime and much less in the soft x-ray range [166]. Performing XPCS measurements on artificial spin ice would bring not only novel insights into the nature of magnetic fluctuations occurring in the system, but also a development and application of this technique on a frustrated system.

As a first step for XPCS, we made the first tests of coherent SXRMS in June 2014 at the Swiss Light Source. We introduced a pinhole of 30 μm diameter in the beam path prior to the diffractometer. We used the transmission geometry which makes simpler the acquisition of speckles. The size of a speckle size dx_s depends on the illuminated area.

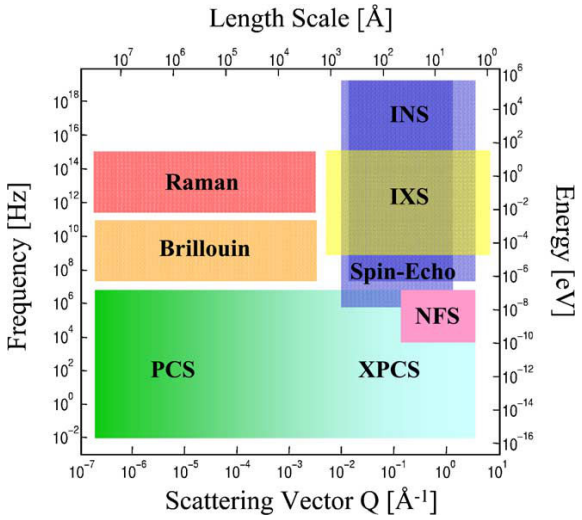


Figure 6.2: Scattering and frequencies accessible with spectroscopic techniques. The acronyms correspond to: INS: Inelastic Neutron Scattering; IXS: Inelastic X-ray Scattering; NFS: Nuclear Forward Scattering; PCS: Photon Correlation Spectroscopy; XPCS: X-ray Photon Correlation Spectroscopy. Reproduced from Grübel and Zontone [164].

Considering the photon wavelength λ and array size D, dx_s is calculated using [1]:

$$dx_s = 1.27\frac{\lambda d}{D}$$

with d the detector-sample distance. In our experiments, we illuminated areas of different size, starting from 4.5×4.5 μm^2 up to 175×175 μm^2 . Using the equation above with $\lambda = 0.00175\mu m$ and $d = 30cm$, one found that an illuminated area of 4.5 μm gives speckles with a size of 114 μm and an area of 18 μm speckles of $29\mu m$. Given the size of the CCD pixel (20×20 μm), we were expecting to be able to resolve the speckles which has not been the case in our experiments. We believe that their intensities are very weak compared to the Bragg peaks which limits the acquisition time (figure 6.1a). The design of a mask similar to that for the reflection geometry would allow such an observation.

We also could go one step further and perform Fourier transform holography (FTH) [143]. By using a gold mask, this will allow us to image an area of a few micrometers in diameter. By choosing an appropriate fluctuation rate, one might be able to obtain a series of images detailing the specific spatial arrangement of the fluctuations. Imaging of a periodic array by FTH has been achieved before [167] and could be possibly extended to artificial spin ice. It is also a routine technique at free electron laser sources [168]. FTH imaging of the artificial spin ice would bring more detailed insight about the details of the magnetization in the nanomagnets by achieving a higher resolution than observed with real space microscopy techniques. In particular, it could be used to confirm our hypothesis about the magnetization state at the ends of the nanomagnets (see section 4.3.4).

Both techniques could be used using the new experimental chamber dedicated to coherent spectroscopy located at the SEXTANTS beamline of the synchrotron SOLEIL (annex C). Currently under commissioning (July 2014), this novel end station has been designed to provide a high degree of stability which is a necessary prerequisite for both XPCS and FTH experiments when the sample and the mask are on independent holders. Detection of the signal is assured by a CCD camera similar to the one we used to record the 2D

[1] According to equation 2 in http://publib.upol.cz/ obd/fulltext/physic38/physic38-11.pdf

scattering pattern (section 4.1.2). Artificial spin ice could thus be studied using this new instrument using with XPCS and FTH. And thus, further insights will be obtained about the magnetic properties of these fascinating materials.

Appendix A

Fabrication

Experimentals protocols

Spin-coating

- 20 nm PMMA (50K)
  Solution : 1% PMMA (50K) in ethyl lactate
  Speed : 4000 rpm
  Acceleration : 3000 rpm
  Time : 45 s
  Baking temperature : 180°C
  Baking time : 5 min

- 70 nm PMMA (950K)
  Solution : 2% PMMA (950K) in ethyl lactate
  Speed : 4000 rpm
  Acceleration : 3000 rpm
  Time: 45 s
  Baking temperature : 180°C
  Baking time : 5 min

Development

in Hamatech Spray-developer

- Solution : Methyl isobutyl ketone: Isopropanol
  Ratio : 1:3
  Time : 45s

Evaporation

in Balzers BAE 250

- Permalloy evaporation
  Material : Permalloy ($Ni_{80}Fe_{20}$)
  Boat material : Tungsten Minimum current : 4.6 A
  Maximum current : 4.8 A

- Cobalt evaporation
  Material : Cobalt
  Boat material : Tungsten Minimum current : 4.6 A
  Maximum current : 4.8 A

Lift-off

All solvents are MOS quality

- Samples remain in acetone at 50°C for 10 minutes
- Samples are sonicated once 10 minutes in acetone at 50°C
- Samples are sonicated once 5 minutes in acetone at 50°C
- Samples are sonicated twice 3 minutes in isopropanol at 25°C

Applications

Artificial spin ice

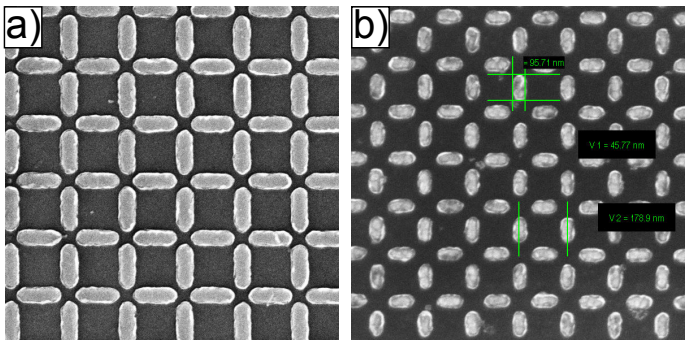


Figure A.1: Artificial square ice created by electron-beam lithography. a) island length: 230 nm, width: 80 nm; lattice parameter: 310 nm. b) island length: 92 nm, width: 42 nm, lattice parameter: 179 nm

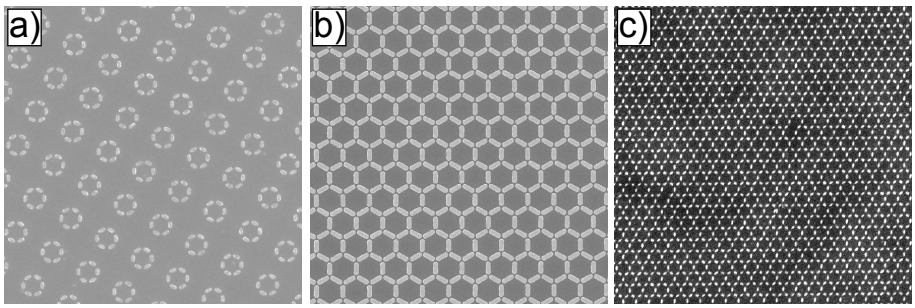


Figure A.2: Artificial kagome ice created by electron-beam lithography. a) island length: 60 nm, width: 20 nm; lattice parameter: 175 nm. b) island length: 230 nm, width: 80 nm, lattice parameter: 550 nm. c) island length: 40 nm, width: 15 nm, lattice parameter: 175nm.

Appendix B

Algorithms

In collaboration with A. Farhan from the *Paul Scherrer Institut*, we developed several algorithms for the analysis of the correlations between nanomagnets in artificial spin ice, similar to what has been done by Wang and co-workers in artificial square ice [43] or by Rougemaille and colleagues in artificial kagome ice [169]. We will present here the algorithms developed for the analysis of artificial kagome ice pictures, but the same idea have been used for artificial square ice.

The analysis is based on x-ray photoelectron emission microscopy picture. An algorithm assimilates each nanomagnets to a pixel, which intensity is compared to the average intensity of the picture (figure B.1). Depending on the sub-lattice as well as on the comparison, it attributes to each nanomagnets a spin, which is later use to calculate dot products. Then, another algorithm is used to establish a table of the distances between nanomagnets, used to determine which correlation needs to be calculated (figure B.2). Dependant on the distance, one of the two algorithms is then called to compute the correct correlation value (figure B.4 and figure B.5), which is normalized by the number of calls at the end of the code.

Apart from the execution speed, one main problem of this code appears when the contrast in the picture is not strong enough. In that case, the comparison between the pixel value and the average value can be wrong, and brings wrong results at the end.

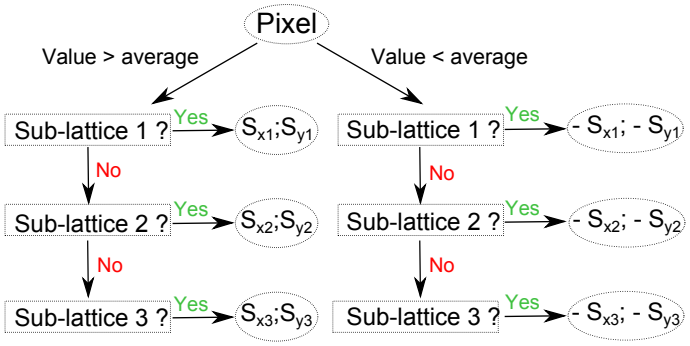


Figure B.1: Determination of the spin value. Depending of the comparison between pixel intensity and average pixel intensity, each nanomagnet represented by a pixel is attributed a spin value.

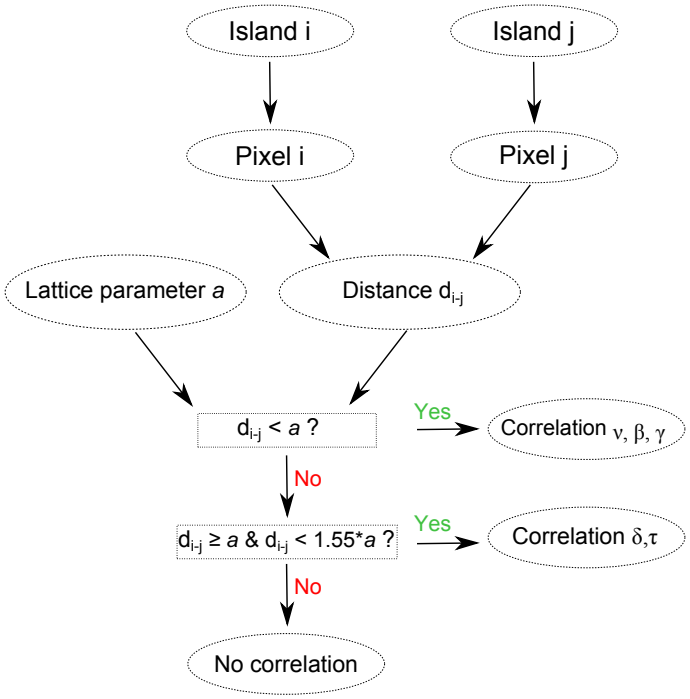


Figure B.2: Computation of distances. This algorithm determines the distance between two pixels, and after comparison with the lattice parameter a, determine which correlation algorithm needs to be called. The notation of the correlations followed Rougemaille *et al.* B.3 [169].

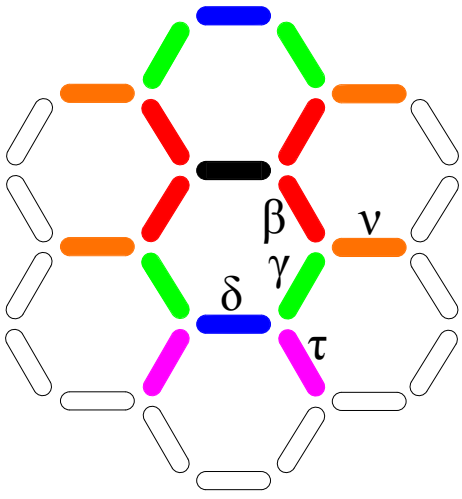


Figure B.3: Nomenclature of the correlations. Adapted from Rougemaille *et al.* [169]

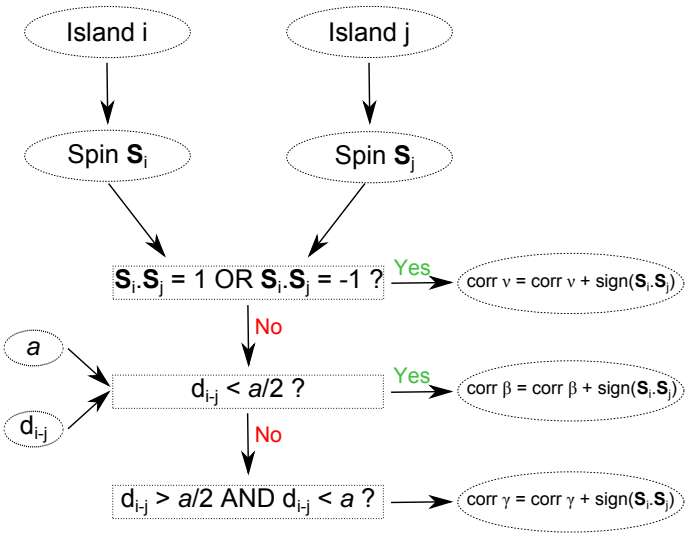


Figure B.4: Correlation ν, β and γ.

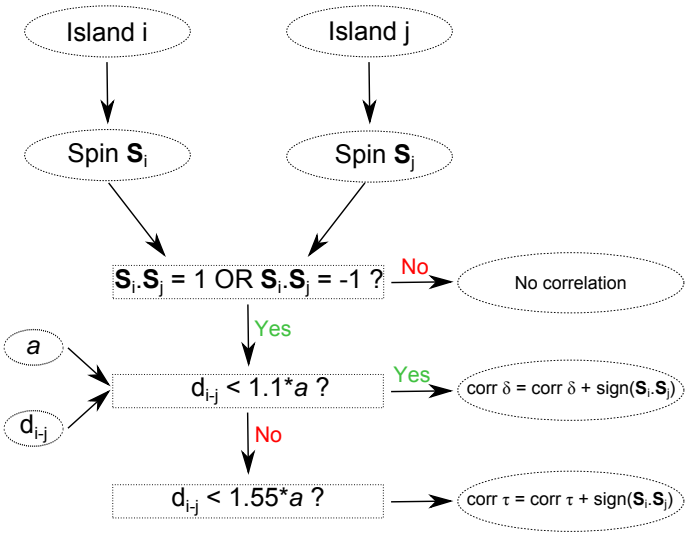


Figure B.5: Correlation δ and τ.

Appendix C

Instrumentation

The COSMOS (COherent Scattering MicrOScopy) instrument (figure C.1)) is a new instrument dedicated to soft x-ray techniques requiring both flexibility and stability, such as x-ray photon correlation spectroscopy or Fourier transform holography. It is currently located at the beamline SEXTANTS of the synchrotron SOLEIL [150]. So far, it allows to perform experiments requiring transmission of the x-ray beam, and future developments are planned to make reflection geometry also available.

This instrument is composed of two chambers. Experimental set-up and sample are located in the front chamber (right in figure C.1b and figure C.1c). The bottom chamber contains a Princeton CCD camera which acts as a 2D detector. (left on figure C.1b). It is mounted on a trolley moved by two stepper motors, one allowing to move along the beam axis and the second one in the direction perpendicular. We can therefore allow the incoming photon beam to go through the instrument and thus to be used in subsequent experiments (figure C.3b).

The CCD chip contains 2048×2048 pixels of individual size 13.5 $\mu m\times$ 13.5 μm. The CCD chip is protected with an aluminium filter against visible light and a beamstop is placed at the position of the incoming x-ray beam to prevent direct exposition. This beamstop is moved using two motors along both x and y axis.

As mentioned, the front part of COSMOS contains the experimental set-up with sample (figure C.2). The chamber is composed of an opened aluminium cube whic is closed by stainless steel plates. These plates can be designed for specific requirements and are thus easily exchangeable. The top side is closed by an adapter plate holding a CF 200 quick-access door (Vacom). Sides of this cube are closed by seven plates with variable size of

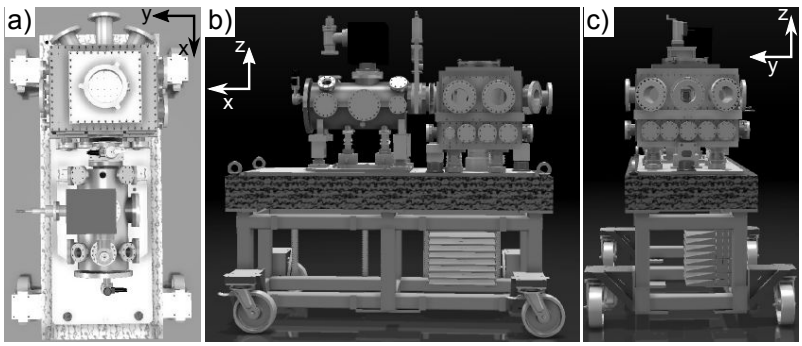


Figure C.1: Different views of COSMOS: a) top view, b) side view and c) front view with corresponding axis notation.

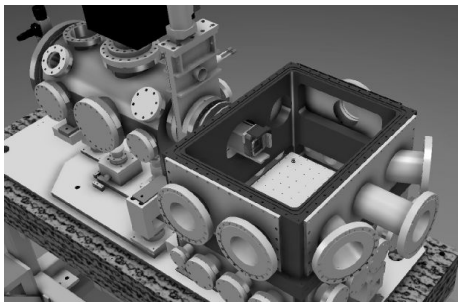


Figure C.2: Experimental chamber. An optical table is located in the chamber which allow a strong adaptability of the experimental set-up as well as a simple change of samples.

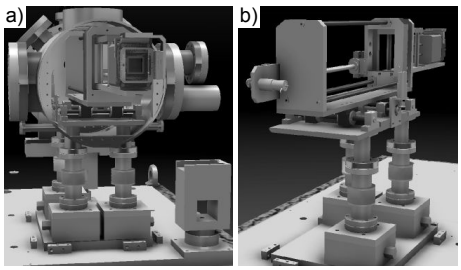


Figure C.3: Detector chamber. a) Front and b) bottom views. The detector is mounted on a trolley having two motions. The first one is along the beam axis, allowing to probe different values of the **q**-space. The second motion is perpendicular to this axis, thus allowing the incoming beam to pass through the instrument to be used in subsequent instruments.

flanges. The smallest flanges (CF 50) are used for electrical connectivity and the largest (CF 150) for pumps and windows.

Sealing is maintained by double vitton gaskets; a primary pump is connected to the gap between the gaskets to ensure good vaccuum conditions without requiring the use of copper gasket. A second primary pump in combination with a turbo-pump is used to pump within the cube. After pumping overnight, we reach a base pressure of 2×10^{-6} mbar with an experimental set-up in the cube, without baking the whole instrument.

The cube is decoupled from the rest of COSMOS by use of four pneumatic dampers FAEBI (Bilz). The experimental set-up is located on an optical table which is directly set on the frame of the instrument. We thus expect no vibration from the different pumps to be transmitted as stability is an important factor for the use of advanced x-ray technique.

As mentioned, the rear part contains the detector (figure C.3). When samples or set-up are changed, it is kept under vacuum by an independent primary and secondary pumping. The base pressure is 1×10^{-6} mbar overnight. Water cooling and electrical contact are ensured by the different flanges located around the chamber.

At the time when this thesis was written (September 2014), COSMOS was still under commissioning. Nevertheless, the first experiments carried by external users have happened in July 2014 on carbon-based materials. These have shown that this instrument offers a real opportunity to perform advanced x-ray technique; in this case was the use of coherent x-rays. A project using COSMOS for the investigation of fast dynamics in artificial spin ice using XPCS and FTH have been approved and will take place in December 2014. We expect then to use the full power of the chamber to bring new insights on the properties of this magnetic system based on the scientific work presented in this thesis.

Bibliography

[1] A P Ramirez. Strongly geometrically frustrated magnets. *Annu. Rev. Mater. Sci.*, 24(1):453–480, 1994.

[2] J. Snyder, J. S. Slusky, R. J. Cava, and P. Schiffer. How 'spin ice' freezes. *New J. Phys.*, 413(6851):48–51, September 2001.

[3] C. Nisoli, R. Moessner, and P. Schiffer. Colloquium: Artificial spin ice: Designing and imaging magnetic frustration. *Rev. Mod. Phys.*, 85(4):1473–1490, October 2013.

[4] L. J. Heyderman and R. L. Stamps. Artificial ferroic systems: novel functionality from structure, interactions and dynamics. *J. Phys.: Condens. Matter*, 25(36):363201, September 2013.

[5] C. Phatak, A. K. Petford-Long, O. Heinonen, M. Tanase, and M. De Graef. Nanoscale structure of the magnetic induction at monopole defects in artificial spin-ice lattices. *Phys. Rev. B*, 83:5, May 2011.

[6] E. Mengotti, L. J. Heyderman, A. Fraile Rodriguez, A. Bisig, L. Le Guyader, F. Nolting, and H. B. Braun. Building blocks of an artificial kagome spin ice: Photoemission electron microscopy of arrays of ferromagnetic islands. *Phys. Rev. B*, 78, October 2008.

[7] S. Ladak, D. E. Read, G. K. Perkins, L. F. Cohen, and W. R. Branford. Direct observation of magnetic monopole defects in an artificial spin-ice system. *Nat. Phys.*, 6:359–363, May 2010.

[8] T. Fennell, O. A. Petrenko, B. Fak, S. T. Bramwell, M. Enjalran, T. Yavors'kii, M. J. P. Gingras, R. G. Melko, and G. Balakrishnan. Neutron scattering investigation of the spin ice state in dy2ti2o7. *Phys. Rev. B*, 70, October 2004.

[9] J. Perron, L. Anghinolfi, B. Tudu, N. Jaouen, J.-M. Tonnerre, M. Sacchi, F. Nolting, J. Lüning, and L. J. Heyderman. Extended reciprocal space observation of artificial spin ice with x-ray resonant magnetic scattering. *Phys. Rev. B*, 88(21):214424, 2013.

[10] K. Chesnel, M. Belakhovsky, G. van der Laan, F. Livet, A. Marty, G. Beutier, S. P. Collins, and A. Haznar. Tracking the local reversal processes in nanostructures by magnetic speckles. *Phys. Rev. B*, 70:180402(R), November 2004.

[11] D. R. Lee, J. W. Freeland, Y. Choi, G. Srajer, V. Metlushko, and B. Ilic. X-ray resonant magnetic scattering study of magnetization reversals in a nanoscale spin-valve array. *Phys. Rev. B*, 76, October 2007.

[12] C. Spezzani, M. Fabrizioli, P. Candeloro, E. Di Fabrizio, G. Panaccione, and M. Sacchi. Magnetic order in a submicron patterned permalloy film studied by resonant x-ray scattering. *Phys. Rev. B*, 69(22):224412, 2004.

[13] G. Schütz, W. Wagner, W. Wilhelm, P. Kienle, R. Zeller, R. Frahm, and G. Materlik. Absorption of circularly polarized x rays in iron. *Phys. Rev. Lett.*, 58(7):737–740, February 1987.

[14] H. Cavendish. Three papers, containing experiments on factitious air, by the hon. henry cavendish, f. r. s. *Phil. Trans.*, 56:141–184, January 1766.

[15] CNRS. Oeuvres de lavoisier. tome premier. traité élémentaire de chimie., 1864. Traité élémentaire de chimie.

[16] J. D. Bernal and R. H. Fowler. A theory of water and ionic solution, with particular reference to hydrogen and hydroxyl ions. *J. Chem. Phys*, 1(8):515–548, August 1933.

[17] W. F. Giauque and M. F. Ashley. Molecular rotation in ice at 10°k. free energy of formation and entropy of water. *Phys. Rev.*, 43(1):81–82, January 1933.

[18] L. Pauling. The structure and entropy of ice and of other crystals with some randomness of atomic arrangement. *J. Am. Chem. Soc.*, 57(12):2680–2684, 1935.

[19] R.L. Stamps. Magnetism. In E. Beaurepaire, H. Bulou, L. Joly, and F. Scheurer, editors, *Magnetism and Synchrotron Radiation: Towards the Fourth Generation Light Sources*, number 151 in Springer Proceedings in Physics, pages 1–49. Springer International Publishing, January 2013.

[20] W. Heisenberg. Mehrkörperproblem und resonanz in der quantenmechanik. *Z. Physik*, 38(6-7):411–426, June 1926.

[21] P. a. M. Dirac. On the theory of quantum mechanics. *Proc. R. Soc. Lond. A*, 112(762):661–677, October 1926.

[22] C. Lacroix. Introduction to magnetism. In E. Beaurepaire, H. Bulou, F. Scheurer, and J.-P. Kappler, editors, *Magnetism: A Synchrotron Radiation Approach*, number 697 in Lecture Notes in Physics, pages 1–13. Springer Berlin Heidelberg, January 2006.

[23] N. F. Mott. A discussion of the transition metals on the basis of quantum mechanics. *Proc. Phys. Soc.*, 47(4):571, July 1935.

[24] J. C. Slater. The ferromagnetism of nickel. *Phys. Rev.*, 49(7):537–545, 1936.

[25] J. C. Slater. The ferromagnetism of nickel. II. temperature effects. *Phys. Rev.*, 49(12):931–937, 1936.

[26] E. C. Stoner. Collective electron ferromagnetism. *Proc. R. Soc. Lond. A*, 165(922):372–414, April 1938.

[27] W. Weber. Introduction to magnetism. In E. Beaurepaire, H. Bulou, F. Scheurer, and J.-P. Kappler, editors, *Magnetism and Synchrotron Radiation*, number 133 in Springer Proceedings in Physics, pages 1–41. Springer Berlin Heidelberg, January 2010.

[28] K. Baberschke. Anisotropy in magnetism. In K. Baberschke, W. Nolting, and M. Donath, editors, *Band-Ferromagnetism*, number 580 in Lecture Notes in Physics, pages 27–45. Springer Berlin Heidelberg, January 2001.

[29] J.I. Martin, J. Nogués, K. Liu, J.L Vicent, and I. K. Schuller. Ordered magnetic nanostructures: fabrication and properties. *Journal of Magnetism and Magnetic Materials*, 256(1–3):449–501, January 2003.

[30] J. E. Greedan. Geometrically frustrated magnetic materials. *J. Mater. Chem.*, 11(1):37–53, January 2001.

[31] M. J. Harris, S. T. Bramwell, D. F. McMorrow, T. Zeiske, and K. W. Godfrey. Geometrical frustration in the ferromagnetic pyrochlore ho2ti2o7. *Phys. Rev. Lett.*, 79(13):2554–2557, September 1997.

[32] T. Fennell, P. P. Deen, A. R. Wildes, K. Schmalzl, D. Prabhakaran, A. T. Boothroyd, R. J. Aldus, D. F. McMorrow, and S. T. Bramwell. Magnetic coulomb phase in the spin ice ho2ti2o7. *Science*, 326(5951):415–417, October 2009.

[33] J. Snyder, B. G. Ueland, J. S. Slusky, H. Karunadasa, R. J. Cava, and P. Schiffer. Low-temperature spin freezing in the dy2ti2o7 spin ice. *Phys. Rev. B*, 69(6):064414, February 2004.

[34] H. Kadowaki, Y. Ishii, K. Matsuhira, and Y. Hinatsu. Neutron scattering study of dipolar spin ice ho2sn2o7: Frustrated pyrochlore magnet. *Phys. Rev. B*, 65, April 2002.

[35] A. P. Ramirez, A. Hayashi, R. J. Cava, R. Siddharthan, and B. S. Shastry. Zero-point entropy in 'spin ice'. *Nature*, 399:333–335, May 1999.

[36] S. T. Bramwell and M. J. P. Gingras. Spin ice state in frustrated magnetic pyrochlore materials. *Science*, 294, November 2001.

[37] B. C. den Hertog and M. J. P. Gingras. Dipolar interactions and origin of spin ice in ising pyrochlore magnets. *Phys. Rev. Lett.*, 84(15):3430–3433, 2000.

[38] S. V. Isakov, R. Moessner, and S. L. Sondhi. Why spin ice obeys the ice rules. *Phys. Rev. Lett.*, 95(21):217201, November 2005.

[39] P. J. Baker, M. J. Matthews, S. R. Giblin, P. Schiffer, C. Baines, and D. Prabhakaran. Unusual field dependence of spin fluctuations on different timescales in tb2ti2o7. *Phys. Rev. B*, 86:6, September 2012.

[40] S. T. Bramwell, S. R. Giblin, S. Calder, R. Aldus, D. Prabhakaran, and T. Fennell. Measurement of the charge and current of magnetic monopoles in spin ice. *Nature*, 461:956–U211, October 2009.

[41] S. R. Dunsiger, A. A. Aczel, C. Arguello, H. Dabkowska, A. Dabkowski, M.-H. Du, T. Goko, B. Javanparast, T. Lin, F. L. Ning, H. M. L. Noad, D. J. Singh, T. J. Williams, Y. J. Uemura, M. J. P. Gingras, and G. M. Luke. Spin ice: Magnetic excitations without monopole signatures using muon spin rotation. *Phys. Rev. Lett.*, 107(20):207207, November 2011.

[42] P. Quemerais, P. McClarty, and R. Moessner. Possible quantum diffusion of polaronic muons in dy2ti2o7 spin ice. *Phys. Rev. Lett.*, 109, 2012.

[43] R. F. Wang, C. Nisoli, R. S. Freitas, J. Li, W. McConville, B. J. Cooley, M. S. Lund, N. Samarth, C. Leighton, V. H. Crespi, and P. Schiffer. Artificial 'spin ice' in a geometrically frustrated lattice of nanoscale ferromagnetic islands. *Nature*, 439(7074):303–306, January 2006.

[44] Y. Qi, T. Brintlinger, and J. Cumings. Direct observation of the ice rule in an artificial kagome spin ice. *Phys. Rev. B*, 77:094418, March 2008.

[45] L. A. S. Mol, A. R. Pereira, and W. A. Moura-Melo. Extending spin ice concepts to another geometry: The artificial triangular spin ice (vol 85, 184410, 2012). *Phys. Rev. B*, 86, December 2012.

[46] J. Li, X. Ke, S. Zhang, D. Garand, C. Nisoli, P. Lammert, V. H. Crespi, and P. Schiffer. Comparing artificial frustrated magnets by tuning the symmetry of nanoscale permalloy arrays. *Phys. Rev. B*, 81:092406, March 2010.

[47] M. J. Morrison, T. R. Nelson, and C. Nisoli. Unhappy vertices in artificial spin ice: new degeneracies from vertex frustration. *New J. Phys.*, 15(4):045009, April 2013.

[48] C. Tannous and J. Gieraltowski. The stoner–wohlfarth model of ferromagnetism. *Eur. J. Phys.*, 29(3):475, May 2008.

[49] E. C. Stoner and E. P. Wohlfarth. A mechanism of magnetic hysteresis in heterogeneous alloys. *Phil. Trans. R. Soc. Lond. A*, 240(826):599–642, May 1948.

[50] G. Möller and R. Moessner. Artificial square ice and related dipolar nanoarrays. *Phys. Rev. Lett.*, 96(23):237202, 2006.

[51] G. Möller and R. Moessner. Magnetic multipole analysis of kagome and artificial spin-ice dipolar arrays. *Phys. Rev. B*, 80:140409(R), October 2009.

[52] E. Mengotti. *The artificial kagome spin-ice system: from building blocks to emergent monopoles*. PhD thesis, ETH Zurich, Zurich, 2010.

[53] L. A. Mol, R. L. Silva, R. C. Silva, A. R. Pereira, W. A. Moura-Melo, and B. V. Costa. Magnetic monopole and string excitations in two-dimensional spin ice. *J. Appl. Phys.*, 106(6):063913–063913–5, September 2009.

[54] R. F. Wang, J. Li, W. McConville, C. Nisoli, X. Ke, J. W. Freeland, V. Rose, M. Grimsditch, P. Lammert, V. H. Crespi, and P. Schiffer. Demagnetization protocols for frustrated interacting nanomagnet arrays. *J. Appl. Phys.*, 101(9):09J104–09J104–3, May 2007.

[55] X. Ke, J. Li, C. Nisoli, Paul E. Lammert, W. McConville, R. F. Wang, V. H. Crespi, and P. Schiffer. Energy minimization and ac demagnetization in a nanomagnet array. *Phys. Rev. Lett.*, 101(3), July 2008.

[56] C. Nisoli, R. Wang, J. Li, W. F. McConville, P. E. Lammert, P. Schiffer, and V. H. Crespi. Ground state lost but degeneracy found: The effective thermodynamics of artificial spin ice. *Phys. Rev. Lett.*, 98(21):217203, 2007.

[57] Z. Budrikis, J. P. Morgan, J. Akerman, A. Stein, Paolo Politi, S. Langridge, C. H. Marrows, and R. L. Stamps. Disorder strength and field-driven ground state domain formation in artificial spin ice: Experiment, simulation, and theory. *Phys. Rev. Lett.*, 109, July 2012.

[58] J. P. Morgan, A. Stein, S. Langridge, and C. H. Marrows. Thermal ground-state ordering and elementary excitations in artificial magnetic square ice. *Nat. Phys.*, 7:75–79, January 2011.

[59] Z. Budrikis, K. L. Livesey, J. P. Morgan, J. Akerman, A. Stein, S. Langridge, C. H. Marrows, and R. L. Stamps. Domain dynamics and fluctuations in artificial square ice at finite temperatures. *New J. Phys.*, 14:035014, March 2012.

[60] C. Nisoli. On thermalization of magnetic nano-arrays at fabrication. *New J. Phys.*, 14(3):035017, March 2012.

[61] A. Farhan, P. M. Derlet, A. Kleibert, A. Balan, R. V. Chopdekar, M. Wyss, J. Perron, A. Scholl, F. Nolting, and L. J. Heyderman. Direct observation of thermal relaxation in artificial spin ice. *Phys. Rev. Lett.*, 111(5):057204, 2013.

[62] I. Syôzi. Statistics of kagomé lattice. *Prog. Theor. Phys.*, 6(3):306–308, 1951.

[63] M. Tanaka, E. Saitoh, H. Miyajima, T. Yamaoka, and Y. Iye. Magnetic interactions in a ferromagnetic honeycomb nanoscale network. *Phys. Rev. B*, 73, February 2006.

[64] S. Ladak, D. E. Read, W. R. Branford, and L. F. Cohen. Direct observation and control of magnetic monopole defects in an artificial spin-ice material. *New J. Phys.*, 13:063032, June 2011.

[65] E. Mengotti, L. J. Heyderman, A. F. Rodriguez, F. Nolting, R. V. Huegli, and H.-B. Braun. Real-space observation of emergent magnetic monopoles and associated dirac strings in artificial kagome spin ice. *Nat. Phys.*, 7:68–74, January 2011.

[66] P. a. M. Dirac. Quantised singularities in the electromagnetic field. *Proc. R. Soc. Lond. A*, 133(821):60–72, September 1931.

[67] C. Castelnovo, R. Moessner, and S. L. Sondhi. Magnetic monopoles in spin ice. *Nature*, 451:42–45, January 2008.

[68] D. J. P. Morris, D. A. Tennant, S. A. Grigera, B. Klemke, C. Castelnovo, R. Moessner, C. Czternasty, M. Meissner, K. C. Rule, J.-U. Hoffmann, K. Kiefer, S. Gerischer, D. Slobinsky, and R. S. Perry. Dirac strings and magnetic monopoles in the spin ice dy2ti2o7. *Science*, 326(5951):411–414, October 2009.

[69] R. V. Hügli, G. Duff, B. O'Conchuir, E. Mengotti, A. Fraile Rodriguez, F. Nolting, L. J. Heyderman, and H. B. Braun. Artificial kagome spin ice: dimensional reduction, avalanche control and emergent magnetic monopoles. *Phil. Trans. R. Soc. A*, 370:5767–5782, 2012.

[70] A. Farhan, P. M. Derlet, A. Kleibert, A. Balan, R. V. Chopdekar, M. Wyss, L. Anghinolfi, F. Nolting, and L. J. Heyderman. Exploring hyper-cubic energy landscapes in thermally active finite artificial spin-ice systems. *Nat. Phys.*, 9(6):375–382, 2013.

[71] Alan Farhan, Armin Kleibert, Peter M. Derlet, Luca Anghinolfi, Ana Balan, Rajesh V. Chopdekar, Marcus Wyss, Sebastian Gliga, Frithjof Nolting, and Laura J. Heyderman. Thermally induced magnetic relaxation in building blocks of artificial kagome spin ice. *Phys. Rev. B*, 89(21):214405, 2014.

[72] H. Frauenfelder, S. G. Sligar, and P. G. Wolynes. The energy landscapes and motions of proteins. *Science*, 254(5038):1598–1603, December 1991.

[73] V. Kapaklis, U. B. Arnalds, A. Harman-Clarke, E. Papaioannou, M. Karimipour, P. Korelis, A. Taroni, P. C. W. Holdsworth, S. T. Bramwell, and B. Hjorvarsson. Melting artificial spin ice. *New J. Phys.*, 14, March 2012.

[74] J. M. Porro, A. Bedoya-Pinto, A. Berger, and P. Vavassori. Exploring thermally induced states in square artificial spin-ice arrays. *New J. Phys.*, 15(5):055012, May 2013.

[75] S. Zhang, I. Gilbert, C. Nisoli, G.-W. Chern, M. J. Erickson, L. O'Brien, C. Leighton, P. E. Lammert, V. H. Crespi, and P. Schiffer. Crystallites of magnetic charges in artificial spin ice. *Nature*, 500(7464):553–557, 2013.

[76] Y. Li, T.X. Wang, H.Y. Liu, X.F. Dai, and G.D. Liu. Geometry effect on the magnetic ordering of geometrically frustrated rectangular and triangular magnets. *Physics Letters A*, 375(13):1548–1551, March 2011.

[77] L. A. S. Mol, A. R. Pereira, and W. A. Moura-Melo. Extending spin ice concepts to another geometry: The artificial triangular spin ice. *Phys. Rev. B*, 85:184410, May 2012.

[78] J. H. Rodrigues, L. A. S. Mól, W. A. Moura-Melo, and A. R. Pereira. Efficient demagnetization protocol for the artificial triangular spin ice. *Appl. Phys. Lett.*, 103(9):092403, August 2013.

[79] G.-W. Chern, M. J. Morrison, and C. Nisoli. Degeneracy and criticality from emergent frustration in artificial spin ice. *Phys. Rev. Lett.*, 111(17):177201, October 2013.

[80] V. S. Bhat, J. Sklenar, B. Farmer, J. Woods, J. T. Hastings, S. J. Lee, J. B. Ketterson, and L. E. De Long. Controlled magnetic reversal in permalloy films patterned into artificial quasicrystals. *Phys. Rev. Lett.*, 111(7):077201, 2013.

[81] A. A. Mistonov, N. A. Grigoryeva, A. V. Chumakova, H. Eckerlebe, N. A. Sapoletova, K. S. Napolskii, A. A. Eliseev, D. Menzel, and S. V. Grigoriev. Three-dimensional artificial spin ice in nanostructured co on an inverse opal-like lattice. *Phys. Rev. B*, 87(22):220408, 2013.

[82] J. P. Morgan, J. Akerman, A. Stein, C. Phatak, R. M. L. Evans, S. Langridge, and C. H. Marrows. Real and effective thermal equilibrium in artificial square spin ices. *Phys. Rev. B*, 87:024405, 2013.

[83] S. D. Pollard, V. Volkov, and Y. Zhu. Propagation of magnetic charge monopoles and dirac flux strings in an artificial spin-ice lattice. *Phys. Rev. B*, 85:180402(R), May 2012.

[84] K. Zeissler, S. K. Walton, S. Ladak, D. E. Read, T. Tyliszczak, L. F. Cohen, and W. R. Branford. The non-random walk of chiral magnetic charge carriers in artificial spin ice. *Sci. Rep.*, 3:1252, February 2013.

[85] T. Fennell, S. T. Bramwell, D. F. McMorrow, P. Manuel, and A. R. Wildes. Pinch points and kasteleyn transitions in kagome ice. *Nat. Phys.*, 3(8):566–572, 2007.

[86] J. P. Morgan, C. J. Kinane, T. R. Charlton, A. Stein, C. Sánchez-Hanke, D. A. Arena, S. Langridge, and C. H. Marrows. Magnetic hysteresis of an artificial square ice studied by in-plane bragg x-ray resonant magnetic scattering. *AIP Advances*, 2(2):022163–022163–10, June 2012.

[87] P. B. Meggs. *A history of graphic design*. John Wiley & Sons, 3,illustrated edition, 1998.

[88] Intel. Moore's law and intel innovation, March 2013.

[89] V. A. Guzenko. Paul scherrer institut (PSI) :: Electron beam lithography, 2012.

[90] AllRESIST GmbH. Photoresist, e-beam resist, optical-/e-beam-lithographie - ALLRESIST GmbH, germany, 2013.

[91] I. Haller, M. Hatzakis, and R. Srinivasan. High-resolution positive resists for electron-beam exposure. *IBM J. Res. Dev.*, 12(3):251 –256, May 1968.

[92] M. Hatzakis. Electron resists for microcircuit and mask production. *J. Electrochem. Soc.*, 116(7):1033–1037, July 1969.

[93] B. A. Miller-Chou and J. L. Koenig. A review of polymer dissolution. *Prog. Polym. Sci.*, 28(8):1223–1270, August 2003.

[94] M. A. McCord and M. J. Rooks. Electron beam lithography. In *Microlithography*, volume 1 of *Handbook of Microlithography, Micromachining and Microfabrication*, pages 128–252. IET, illustrated edition, 1997.

[95] T. H. P. Chang. Proximity effect in electron-beam lithography. *J. Vac. Sci. Technol.*, 12(6):1271–1275, 1975.

[96] D. Drouin, A. R. Couture, D. Joly, X. Tastet, V. Aimez, and R. Gauvin. CASINO v2.42—a fast and easy-to-use modeling tool for scanning electron microscopy and microanalysis users. *Scanning*, 29(3):92–101, 2007.

[97] M. Vos, R.P. McEachran, E. Weigold, and R.A. Bonham. Elastic electron scattering cross sections at high momentum transfer. *Nucl. Instrum. Meth. B*, 2013.

[98] M. Parikh. Self-consistent proximity effect correction technique for resist exposure (SPECTRE). *J. Vac. Sci. Technol.*, 15(3):931–933, 1978.

[99] K. Harafuji, A. Misaka, K. Kawakita, N. Nomura, H. Hamaguchi, and M. Kawamoto. Proximity effect correction data processing system for electron beam lithography. *J Vac. Sci. Technol. B*, 10(1):133–142, 1992.

[100] GenISys. GenISys - BEAMER, February 2013.

[101] M. Mohammad, M. Muhammad, S. K. Dew, and M. Stepanova. Fundamentals of electron beam exposure and development. In M. Stepanova and S. K. Dew, editors, *Nanofabrication*, pages 11–41. Springer Vienna, January 2012.

[102] S. Yasin, D. G. Hasko, and H. Ahmed. Comparison of MIBK/IPA and water/IPA as PMMA developers for electron beam nanolithography. *Microelectronic Engineering*, 61–62:745–753, 2002.

[103] S. Gorelick, V. A. Guzenko, J. Vila-Comamala, and C. David. Direct e-beam writing of dense and high aspect ratio nanostructures in thick layers of PMMA for electroplating. *Nanotechnology*, 21(29):295303, July 2010.

[104] M. S. Blois. Preparation of thin magnetic films and their properties. *J. Appl. Phys.*, 26(8):975–980, August 1955.

[105] Laura J. Heyderman. *Magnetic Properties of Coupled Permalloy Thin Films*. PhD thesis, University of Bristol, Bristol, November 1991.

[106] W. D. Miller. Tungsten contamination of vacuum-deposited permalloy films. *Vacuum*, 15(12):ii–xii, December 1965.

[107] J. Manjkow, J. S. Papanu, D. W. Hess, D. S. S. Soong, and A. T. Bell. Influence of processing and molecular parameters on the dissolution rate of poly-(methyl methacrylate) thin films. *J. Electrochem. Soc.*, 134(8):2003–2007, August 1987.

[108] M. Altarelli. Resonant x-ray scattering: A theoretical introduction. In E. Beaurepaire, H. Bulou, F. Scheurer, and J.-P. Kappler, editors, *Magnetism: A Synchrotron Radiation Approach*, number 697 in Lecture Notes in Physics, pages 201–242. Springer Berlin Heidelberg, January 2006.

[109] J. Stöhr and H. C. Siegmann. *Magnetism - From Fundamentals to Nanoscale Dynamics*. Springer, 1 edition, October 2006.

[110] M. Altarelli. Theoretical basis of photon spectroscopies. In E. Beaurepaire, H. Bulou, L. Joly, and F. Scheurer, editors, *Magnetism and Synchrotron Radiation: Towards the Fourth Generation Light Sources*, number 151 in Springer Proceedings in Physics, pages 95–138. Springer International Publishing, January 2013.

[111] F. De Bergevin and M. Brunel. Observation of magnetic superlattice peaks by x-ray diffraction on an antiferromagnetic NiO crystal. *Phys. Lett. A*, 39(2):141–142, April 1972.

[112] F. De Bergevin and M. Brunel. Diffraction of x-rays by magnetic-materials. i. general formulas and measurements on ferromagnetic and ferrimagnetic compounds. *Acta Crystallogr. Sect. A*, 37(MAY):314–324, 1981.

[113] M. Brunel and F. De Bergevin. Diffraction of x-rays by magnetic materials. 2. measurements on anti-ferromagnetic fe2o3. *Acta Crystallogr. Sect. A*, 37(MAY):324–331, 1981.

[114] B. T. Thole, G. van der Laan, and G. A. Sawatzky. Strong magnetic dichroism predicted in the m4,5 x-ray absorption spectra of magnetic rare-earth materials. *Phys. Rev. Lett.*, 55(19):2086–2088, November 1985.

[115] G. van der Laan, B. T. Thole, G. A. Sawatzky, J. B. Goedkoop, J. C. Fuggle, J.-M. Esteva, R. Karnatak, J. P. Remeika, and H. A. Dabkowska. Experimental proof of magnetic x-ray dichroism. *Phys. Rev. B*, 34(9):6529–6531, November 1986.

[116] C. T. Chen, F. Sette, Y. Ma, and S. Modesti. Soft-x-ray magnetic circular dichroism at the l2,3 edges of nickel. *Phys. Rev. B*, 42(11):7262–7265, October 1990.

[117] M. Blume. Magnetic scattering of x rays (invited). *J. Appl. Phys.*, 57(8):3615–3618, April 1985.

[118] D. Gibbs, D. R. Harshman, E. D. Isaacs, D. B. McWhan, D. Mills, and C. Vettier. Polarization and resonance properties of magnetic x-ray scattering in holmium. *Phys. Rev. Lett.*, 61(10):1241–1244, September 1988.

[119] J. P. Hannon, G. T. Trammell, M. Blume, and Doon Gibbs. X-ray resonance exchange scattering. *Phys. Rev. Lett.*, 61(10):1245–1248, September 1988.

[120] J. P. Hannon, G. T. Trammell, M. Blume, and Doon Gibbs. X-ray resonance exchange scattering. *Phys. Rev. Lett.*, 62(22):2644–2644, 1989.

[121] J. M. Tonnerre, L. Sève, D. Raoux, G. Soullié, B. Rodmacq, and P. Wolfers. Soft x-ray resonant magnetic scattering from a magnetically coupled ag /ni multilayer. *Phys. Rev. Lett.*, 75(4):740–743, July 1995.

[122] C. Spezzani, P. Torelli, R. Delaunay, C. F. Hague, F. Petroff, A. Scholl, E. M. Gullikson, and M. Sacchi. Resonant diffuse x-ray scattering from magnetic multilayers. *Physica B*, 345(1–4):153–156, March 2004.

[123] A. Thompson, D. T. Attwood, E. M. Gullikson, M. R. Howells, K.-J. Kim, J. Kirz, J. B. Kortright, I. Lindau, Y. Liu, P. Pianetta, A. Robinson, J. Scofield, J. Underwood, and G. Williams. *X-Ray Data Booklet*. Lawrence Berkeley National Laboratory, Berkeley, October 2009.

[124] J. Stöhr and Y. Wu. X-ray magnetic circular dichroism: Basic concepts and theory for 3d transition metal atoms. In A. S. Schlachter and F. J. Wuilleumier, editors, *New Directions in Research with Third-Generation Soft XRay Synchrotron Radiation Sources*, Series E: Applied Sciences, pages 221–250. Kluwer, Netherlands, 1994.

[125] A. Rogalev, F. Wilhelm, J. Jaouen, J. Goulon, and J.-P. Kappler. X-ray magnetic circular dichroism: Historical perspective and recent highlights. In E. Beaurepaire, H. Bulou, F. Scheurer, and J.-P. Kappler, editors, *Magnetism: A Synchrotron Radiation Approach*, number 697 in Lecture Notes in Physics, pages 71–93. Springer Berlin Heidelberg, January 2006.

[126] H. Wende and C. Antoniak. X-ray magnetic dichroism. In E. Beaurepaire, H. Bulou, F. Scheurer, and K. Jean-Paul, editors, *Magnetism and Synchrotron Radiation*, number 133 in Springer Proceedings in Physics, pages 145–167. Springer Berlin Heidelberg, January 2010.

[127] B. T. Thole, P. Carra, F. Sette, and G. van der Laan. X-ray circular dichroism as a probe of orbital magnetization. *Phys. Rev. Lett.*, 68(12):1943–1946, March 1992.

[128] P. Carra, B. T. Thole, M. Altarelli, and X. Wang. X-ray circular dichroism and local magnetic fields. *Phys. Rev. Lett.*, 70(5):694–697, 1993.

[129] R. Santra. Concepts in x-ray physics. *J. Phys. B: At. Mol. Opt. Phys.*, 42(2):023001, January 2009.

[130] J. Fink, E. Schierle, E. Weschke, and J. Geck. Resonant elastic soft x-ray scattering. *Rep. Prog. Phys.*, 76(5):056502, May 2013.

[131] P. a. M. Dirac. The quantum theory of the electron. *Proc. R. Soc. Lond. A*, 117(778):610–624, February 1928.

[132] P. a. M. Dirac. A theory of electrons and protons. *Proc. R. Soc. Lond. A*, 126(801):360–365, January 1930.

[133] A.I. Akhiezer and V.B. Beresteskii. *Quantum electrodynamics*. Wiley, New York, 1965.

[134] H. A. Kramers and W. Heisenberg. Über die streuung von strahlung durch atome. *Z. Physik*, 31(1):681–708, February 1925.

[135] L. Paolasini and F. de Bergevin. Magnetic and resonant x-ray scattering investigations of strongly correlated electron systems. *C.R. Phys.*, 9(5–6):550–569, June 2008.

[136] J. P. Hill and D. F. McMorrow. X-ray resonant exchange scattering: Polariztaion dependence and correlation function. *Acta Crystallogr. Sect. A*, 52(2):236–244, March 1996.

[137] J. H. Hubbell, Wm J. Veigele, E. A. Briggs, R. T. Brown, D. T. Cromer, and R. J. Howerton. Atomic form factors, incoherent scattering functions, and photon scattering cross sections. *J.Phys.Chem.Ref.Data*, 4(3):471–538, July 1975.

[138] J. Als-Nielsen and D. McMorrow. *Elements of Modern X-ray Physics*. John Wiley & Sons, 2nd edition, April 2011.

[139] J. D. Watson and F. H. C. Crick. Molecular structure of nucleic acids: A structure for deoxyribose nucleic acid. *Nature*, 171(4356):737–738, April 1953.

[140] W. H. Bragg and W. L. Bragg. The reflection of x-rays by crystals. *Proc. R. Soc. Lond. A*, 88(605):428–438, July 1913.

[141] H. A. Hauptman. The phase problem of x-ray crystallography. *Rep. Prog. Phys.*, 54(11):1427, November 1991.

[142] G. Taylor. The phase problem. *Acta Crystallogr. Sect. D*, 59(11):1881–1890, October 2003.

[143] S. Eisebitt, J. Lüning, W. F. Schlotter, M. Lörgen, O. Hellwig, W. Eberhardt, and J. Stöhr. Lensless imaging of magnetic nanostructures by x-ray spectro-holography. *Nature*, 432(7019):885–888, 2004.

[144] W. Borchardt-Ott. The lattice and its properties. In *Crystallography*, pages 9–21. Springer Berlin Heidelberg, Berlin Heidelberg, 3rd edition, January 2012.

[145] P. P. Ewald. Introduction to dynamical theory of x-ray diffraction. *Acta Crystallogr. Sect. A*, A 25:103–&, 1969.

[146] C. A. Ross, S. Haratani, F. J. Castaño, Y. Hao, M. Hwang, M. Shima, J. Y. Cheng, B. Vögeli, M. Farhoud, M. Walsh, and H. I. Smith. Magnetic behavior of lithographically patterned particle arrays (invited). *J. Appl. Phys.*, 91(10):6848–6853, May 2002.

[147] K. K. Kohli, A. L. Balk, J. Li, S. Zhang, I. Gilbert, P. E. Lammert, V. H. Crespi, P. Schiffer, and N. Samarth. Magneto-optical kerr effect studies of square artificial spin ice. *Phys. Rev. B*, 84, November 2011.

[148] S. Gliga, A. Kákay, R. Hertel, and O. G. Heinonen. Spectral analysis of topological defects in an artificial spin-ice lattice. *Phys. Rev. Lett.*, 110(11):117205, March 2013.

[149] N. Jaouen, J. M. Tonnerre, G. Kapoujian, P. Taunier, J. P. Roux, D. Raoux, and F. Sirotti. An apparatus for temperature-dependent soft x-ray resonant magnetic scattering. *J. Synchrotron Radiat.*, 11:353–357, July 2004.

[150] M. Sacchi, N. Jaouen, H. Popescu, R. Gaudemer, J. M. Tonnerre, S. G. Chiuzbaian, C. F. Hague, A. Delmotte, J. M. Dubuisson, G. Cauchon, B. Lagarde, and F. Polack. The SEXTANTS beamline at SOLEIL: a new facility for elastic, inelastic and coherent scattering of soft x-rays. *J. Phys.: Conf. Ser.*, 425(7):072018, March 2013.

[151] A. Authier. *Dynamical Theory of X-Ray Diffraction.* Oxford University Press, November 2003.

[152] L. Sève, J. M. Tonnerre, and D. Raoux. Determination of the anomalous scattering factors in the soft-x-ray range using diffraction from a multilayer. *J. Appl. Crystallogr.*, 31(5):700–707, October 1998.

[153] K. Chesnel, M. Belakhovsky, S. Landis, J. C. Toussaint, S. P. Collins, G. van der Laan, E. Dudzik, and S. S. Dhesi. X-ray resonant magnetic scattering study of the magnetic coupling in co/pt nanolines and its evolution under magnetic field. *Phys. Rev. B*, 66:024435, July 2002.

[154] G. van der Laan. Soft x-ray resonant magnetic scattering of magnetic nanostructures. *C.R. Phys.*, 9(5–6):570–584, 2008.

[155] N. Rougemaille, F. Montaigne, B. Canals, M. Hehn, H. Riahi, D. Lacour, and J.-C. Toussaint. Chiral nature of magnetic monopoles in artificial spin ice. *New J. Phys.*, 15(3):035026, March 2013.

[156] J. P. Morgan. *Ordering and Defects in Artificial Magnetic Square Ice: Thermodynamic and Field-Driven Processes.* PhD thesis, University of Leeds, Leeds, September 2011.

[157] Z. Budrikis, P. Politi, and R. L. Stamps. Disorder regimes and equivalence of disorder types in artificial spin ice. *J. Appl. Phys.*, 111:07E109, April 2012.

[158] J. S. Pedersen. Analysis of small-angle scattering data from colloids and polymer solutions: modeling and least-squares fitting. *Adv. Colloid. Interfac.*, 70:171–210, 1997.

[159] H. Schnablegger and Y. Singh. *The SAXS Guide Getting acquainted with the principles.* Anton Paar, Austria, October 2011.

[160] M. S. Pierce, C. R. Buechler, L. B. Sorensen, S. D. Kevan, E. A. Jagla, J. M. Deutsch, T. Mai, O. Narayan, J. E. Davies, Kai Liu, G. T. Zimanyi, H. G. Katzgraber, O. Hellwig, E. E. Fullerton, P. Fischer, and J. B. Kortright. Disorder-induced magnetic memory: Experiments and theories. *Phys. Rev. B*, 75(14):144406, 2007.

[161] A. Libal, C. Reichhardt, and C. J. O. Reichhardt. Hysteresis and return-point memory in colloidal artificial spin ice systems. *Phys. Rev. E*, 86, August 2012.

[162] M. S. Pierce, R. G. Moore, L. B. Sorensen, S. D. Kevan, O. Hellwig, E. E. Fullerton, and J. B. Kortright. Quasistatic x-ray speckle metrology of microscopic magnetic return-point memory. *Phys. Rev. Lett.*, 90(17):175502, 2003.

[163] L. Anghinolfi, J. Perron, M. Flokstra, O. Sendetskyi, T. Prokscha, A. Suter, P. M. Derlet, S. Lee, H. Luetkens, and L. J. Heyderman. Muon spin relaxation in active artificial spin ice. *submitted*, 2014.

[164] G. Grübel and F. Zontone. Correlation spectroscopy with coherent x-rays. *Journal of Alloys and Compounds*, 362(1–2):3–11, January 2004.

[165] S. Srivastava, A. K. Kandar, J. K. Basu, M. K. Mukhopadhyay, L. B. Lurio, S. Narayanan, and S. K. Sinha. Complex dynamics in polymer nanocomposites. *Phys. Rev. E*, 79(2):021408, 2009.

[166] S. Konings, C. Schüßler-Langeheine, H. Ott, E. Weschke, E. Schierle, H. Zabel, and J. B. Goedkoop. Magnetic domain fluctuations in an antiferromagnetic film observed with coherent resonant soft x-ray scattering. *Phys. Rev. Lett.*, 106(7):077402, 2011.

[167] B. Pfau, C. M. Günther, E. Guehrs, T. Hauet, H. Yang, L. Vinh, X. Xu, D. Yaney, R. Rick, S. Eisebitt, and O. Hellwig. Origin of magnetic switching field distribution in bit patterned media based on pre-patterned substrates. *Appl. Phys. Lett.*, 99(6):062502–062502–3, August 2011.

[168] D. Gauthier, M. Guizar-Sicairos, X. Ge, W. Boutu, B. Carré, J. R. Fienup, and H. Merdji. Single-shot femtosecond x-ray holography using extended references. *Phys. Rev. Lett.*, 105(9):093901, 2010.

[169] N. Rougemaille, F. Montaigne, B. Canals, A. Duluard, D. Lacour, M. Hehn, R. Belkhou, O. Fruchart, S. El Moussaoui, A. Bendounan, and F. Maccherozzi. Artificial kagome arrays of nanomagnets: A frozen dipolar spin ice. *Phys. Rev. Lett.*, 106(5):057209, 2011.

[170] C. Nisoli, J. Li, X. Ke, D. Garand, P. Schiffer, and V. H. Crespi. Effective temperature in an interacting vertex system: Theory and experiment on artificial spin ice. *Phys. Rev. Lett.*, 105, July 2010.

[171] R. V. Hügli, G. Duff, B. O'Conchuir, E. Mengotti, L. J. Heyderman, A. Fraile Rodriguez, F. Nolting, and H. B. Braun. Emergent magnetic monopoles, disorder, and avalanches in artificial kagome spin ice (invited). *J. Appl. Phys.*, 111:07E103, April 2012.

Résumé

Introduction

La frustration est un phénomène physique qui existe dans de nombreux systèmes. Elle survient lorsque toutes les interactions d'un système ne peuvent être satisfaites en même temps [1]. Dans la nature, le meilleur exemple d'un système frustré est la glace (d'eau). Les différentes longueurs des liaisons entre atomes d'oxygène et d'hydrogène autorisent plusieurs organisations pour une même énergie [18]. À la fin des années 90, des scientifiques ont découvert que certains cristaux magnétiques reproduisent le comportement frustré de la glace. Ces pyrochlores magnétiques ont pour formule chimique $A_2B_2O_7$ avec A un atome de terre rare. Ces atomes sont organisés en tétraèdres [2]. L'état fondamental est décrit par la "règle de glace": dans un tétraèdre, deux moments magnétiques pointent vers son centre et deux moments pointent en-dehors [35]. Cette règle mène à une frustration dans le système car toutes les intéractions (dipolaires et d'échanges) ne peuvent être minimisées en même temps. Par analogie avec la glace, ces matériaux sont appelés "glace de spins". Ce comportement particulier n'est observé qu'à de très basses températures proche du zéro absolu. À température ambiante, les moments pointent dans n'importe quelle direction sous l'effet des fluctuations thermiques.

Depuis 2006, les scientifiques produisent de la "glace de spins artificielle" à l'aide de procédés lithographiques [43]. Ce métamatériau voit les atomes de terre rare remplacés par des nanoaimants allongés. Ces derniers sont composés de matériaux magnétiques comme le Permalloy (un alliage nickel-fer) ou le cobalt avec une aimantation dans le plan. La forme allongée force le moment magnétique dans la direction longue des nanoaimants. Ces particules sont monodomaines car la création d'une paroi de domaine couterait trop d'énergie au système par rapport à la réduction de l'énergie magnétostatique (figure 4.4. Leurs organisation en réseaux bidimensionnels qui reproduisent le comportement des atomes dans la glace de spins, et notamment la règle de glace.

L'un des avantages de la glace de spins artificielle est la possibilité d'observer ces propriétés à l'aide de techniques microscopiques, ce qui n'est pas chose facile avec le système original à cause de sa structure tridimensionnelle. Cependant, elle est un cristal à deux dimensions pour lequel les techniques de diffusion sont applicables. À partir de ces observations, on peut se demander si la diffusion magnétique des rayons X pour étudier la glace de spins artificielle ? Et si oui, quelles sont les informations obtenues, et comment les relier à l'organisation magnétique du système.

Dans ce résumé, nous allons reprendre les points clés du travail effectué. Dans un premier temps, nous allons rappeler les propriétés de la glace de spins artificielle et en particulier les différents niveaux d'organisation des moments magnétiques des nanoaimants autour d'un vertex. L'organisation de l'état initial ainsi que le comportement lors de l'inversion de l'aimantation vont également être évoqués. Ensuite, nous allons présenter le procédé de lithographie développé pour la production des échantillons utilisés dans nos

expériences. La troisième partie de ce résumé comporte un court rappel sur la diffusion résonante des rayons-X mous et l'origine de sa sensibilité au magnétisme. Par la suite, les principaux résultats sont présentés ainsi que les informations obtenues sur l'organisation magnétique. Finalement, nous proposons différentes pistes pour améliorer les paramètres expérimentaux. Avant de conclure, nous rappelons les principaux résultats de nos expériences complémentaires sur ce système.

Organisation magnétique de la glace de spin artificielle

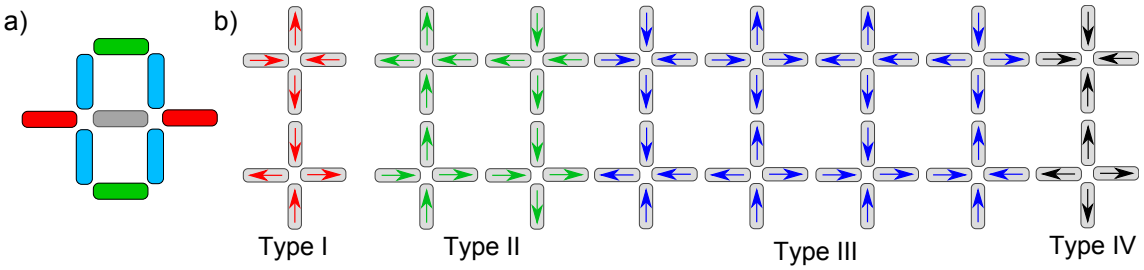
Glace de spins carrée

Première glace de spins artificielle produite, la glace carrée n'est cependant pas équivalente à son pendant naturel [43]. À cause de la géométrie, toutes les interactions dipolaires entre nanoaimants ne sont pas identiques (section 1.4.2). Dans le panneau a) de la figure ci-contre, on a représenté en partie un réseau carré. Les interactions entre plus proches voisins (en bleu) sont plus importantes que les interactions longitudinales (en rouge) qui sont elles-mêmes plus importantes que les interactions transversales (en vert) à cause des distances croissantes entre nanoaimants. En ne considérant que quatre moments magnétiques, à cause des différences entre ces interactions, on peut organiser les moments magnétiques de seize façons différentes (panneau b). Les vertex de type I correspondent à une minimisation des interactions entre plus proches voisins qui mène simultanément à un couplage longitudinal antiferromagnétique. Il s'agit de l'organisation de plus basse énergie. C'est le contraire dans les vertex de type II où ce sont les interactions longitudinales qui sont minimisées au détriment des interactions entre plus proches voisins. Néanmoins dans ces deux cas, la charge magnétique du vertex est nulle, ce qui fait de ces six configurations les seules respectants la "règle de glace" : deux spins pointant vers l'intérieur et deux spins pointant vers l'extérieur du vertex. Au contraire, les arrangements de type III et IV ne respectent pas la règle de glace et ont une charge magnétique non nulle ($\pm$ 2 et $\pm$ 4). Ce sont les arrangements de plus hautes énergies (section 1.4.3).

La recherche de l'état de plus basse énergie de la glace de spins carrée a été un sujet de recherche intensif (section 1.4.2). En effet, il est très tôt apparu que cet état ne pouvait être atteint en utilisant un protocole de démagnétisation [54–56]. En 2011, le groupe de C. Marrows de l'université de Leeds a démontré que le système s'organisait en large domaines de basse énergie séparés par des murs de domaine formés par des vertex de types II et III [58]. Cette organisation est possible grâce à la thermalisation qui se produit lorsque le matériau magnétique est déposé sur le substrat. Celle-ci laisse le temps aux moments magnétiques de se réorganiser [60]. Jusque très récemment, une organisation complète du système dans cet état n'avait pas été observée expérimentalement. En 2013, A. Fahran et ses collègues ont atteint cet objectif, en utilisant des nanoaimants superparamagnétique [61]. Le superparamagnétisme se traduit par une fluctuation du moment magnétique à cause d'une barrière de potentiel très basse qui peut être dépassée grâce à l'énergie thermique. Utilisant cette propriété et à l'aide d'une rampe de température, ils ont étudié la dynamique magnétique qui mène à l'organisation complète du réseau dans son état le plus stable.

Glace de spins kagomé

Le pavage trihexagonal, également appelé kagomé, est connu pour être à l'origine de frustrations géométriques dans les matériaux magnétiques [1] (section 1.4.3). La première glace



Glace de spins carrée. À cause de la géométrie, toutes les interactions dipolaires entre nanoaimants ne sont pas équivalentes (a). Autour d'un vertex existe seize possibilités pour arranger les spins (b). [43].

de spins artificielle utilisant ce réseau a été produite en 2008 [44]. Dans cette configuration, toutes les interactions entre moments magnétiques sont équivalentes comme dans la glace de spins naturelle, mais il n'y a que trois moments par vertex (figure 1.9). Il existe huit possibilités pour arranger les spins. Six sont dominés par la "règle de glace" qui dans le système kagomé s'exprime par deux spins pointant vers un vertex et un en dehors ou vice-versa (type 1). Les deux dernières possibilités ont une énergie plus élevée car tous les moments pointent soit vers l'intérieur soit vers l'extérieur du vertex (type 2). Dans tous les cas, la charge magnétique du vertex n'est pas nulle. Pour les vertex de type 2, la charge magnétique du vertex est souvent qualifiée de "monopole" dans la littérature car proche de la description faite par Dirac [65]. Ces monopoles sont connectés par des chaînes de moments magnétiques renversées par rapport à un fond saturé. Ces dernières sont appelées "chaînes de Dirac" [65].

Fabrication de la glace de spins artificielle

La glace de spins artificielle est obtenue par lithographie [43]. La lithographie est un procédé permettant de transférer rapidement un motif sur un substrat, et ce de manière répétée et reproductible. Il existe de nombreuses techniques lithographiques (section 2.1); pour produire la glace de spins artificielle, nous avons eu recourt à la lithographie par faisceau d'électrons (chapter 2).

Le procédé développé comporte étapes : déposition de la résine, écriture à l'aide d'un faisceau d'électrons, développement, déposition des matériaux et "lift-off". Chacune de ces étapes a une influence sur les autres, et notamment sur l'étape finale qui peut se révéler impossible sous certaines conditions (figure 2.3).

Lors de la première, un polymère servant de résine est déposée sur la surface d'un substrat par la technique dite d'enduction centrifuge (section 2.2). Quelques gouttes de solution contenant le polymère sont déposées sur un substrat qui tourne ensuite à haute vitesse pour éjecter le solvant et former une couche continue et homogène. Dans notre procédé, nous avons utilisé du polymethylmethacrylate (PMMA), une résine de haute-résolution. Deux approches sont décrites en fonction des possibilités techniques disponibles lors de la déposition des matériaux magnétiques (section 2.2). Lorsque le substrat ne peut pas être refroidi pendant la déposition, deux couches de PMMA aux masses molaires différentes sont utilisées. Pendant la déposition, sous l'effet de la température, la résine est endommagée, et ces dommages peuvent empêcher le lift-off (figure 2.3). En utilisant deux couches de PMMA, on protège la couche inférieure des dommages thermiques, et on utilise le fait que la solubilité augmente lorsque la masse molaire diminue pour accélérer l'étape

de lift-off. Malheureusement, la couche de plus faible masse molaire est plus sensible aux électrons ce qui diminue la résolution. Si le substrat peut-être refroidi pendant la déposition, alors l'utilisation d'une seule couche de PMMA est possible. Cette dernière approche est plus simple d'utilisation que la première qui nécessite une exécution rapide pour éviter le mélange des deux couches.

Après l'enduction centrifuge vient l'écriture du motif dans la résine à l'aide d'un faisceau d'électron (section 2.3). Nous avons utilisé l'instrument installé au Laboratoire de Micro- et Nanotechnologie de l'Institut Paul Scherrer en Suisse. Il a permis de couvrir avec de très petits objets jusqu'à 1,5 × 1,5 cm^2 de substrat. Les nanoaimants ont une taille standard de 60 × 20 nm^2, mais les plus petits atteignent 40 × 15 nm^2 en longueur et largeur (annexe A). Des tailles aussi petites ont été atteintes en utilisant la technique de la "sous-découpe/sur-exposition". Cette méthode permet d'atteindre la taille désirée en réduisant la taille des objets à exposer, et en augmentant la dose appliquée. Un des désavantages de cette technique est le contrôle de la forme exacte des objets. En cause, : la diffusion des électrons du faisceau incident par les électrons des atomes de la résine et du substrat augmente la taille de la zone exposée (section 2.3.1).

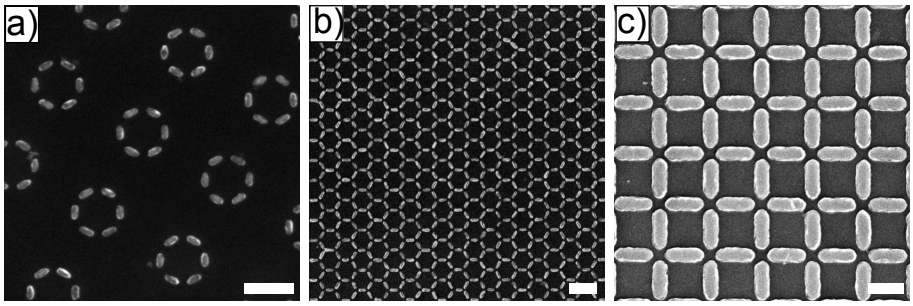
Un procédé chimique est utilisé pour séparer zones exposées et zones non-exposées lors du développement (section 2.3.4). Pour le PMMA, l'exposition au faisceau d'électrons a entrainé une rupture des liaisons chimiques dans le polymère. En rinçant le substrat avec un mélange approprié, on sépare ces chaînes fragmentées des chaînes intactes.

Les matériaux magnétiques sont déposés par la suite (section 2.4). Il existe plusieurs méthodes de déposition; nous avons utilisé est l'évaporation thermique (figure 2.8). De petites billes de matériaux sont déposées dans un creuset qui est chauffé par effet Joule. Le matériau s'évapore et les vapeurs se propagent dans la chambre avant de se déposer sur le substrat. Ce procédé est effectué sous vide (10^{-6} mbar) pour éviter l'oxydation du film. Nous avons déposé du Permalloy, un alliage magnétique nickel-fer ($Ni_{80}Fe_{20}$). Pour obtenir la composition correcte, des billes enrichies en nickel ont été utilisées ($Ni_{81}Fe_{19}$) [105]. Après la déposition de la couche mince magnétique, une couche d'aluminium de 5 nm est déposée pour prévenir l'oxydation du film. Ces couches minces ont été caractérisées structurellement par microscopie électronique par transmission (section 2.6.2) et magnétiquement par effet magnéto-optique Kerr (section 2.6.3). L'analyse structurale a révélé que les films ainsi déposés sont polycristallins, mais cela n'altère pas leurs propriétés magnétiques.

La dernière étape du procédé est le lift-off (section 2.5). Toute la résine restante ainsi que les matériaux déposés à sur celle-ci sont retirés du substrat pour ne laisser que les objets lithographiés. Comme dit au début de cette section, les choix dans les paramètres des étapes précédentes sont essentielles pour le réussir. Le lift-off est fait dans l'acétone chaud ($\sim 50°$) avant que l'échantillon ne soit rincé avec de l'isopropanol. Il est également préférable de minimiser la durée de cette étape, pour limiter l'oxydation des échantillons (section **??**).

Diffusion magnétique résonante des rayons-X mous

La diffusion magnétique résonante des rayons-X mous est une technique photon-entrant/ photon-sortant (figure 3.1). On peut la représenter en deux étapes qui n'en forment en réalité qu'une seule. Le photon est absorbé par un électron du nuage électronique qui effectue une transition entre son niveau fondamental $|0\rangle$ et un niveau d'énergie $|n\rangle$. Ensuite, cet électron effectue la transition inverse en émettant un photon possédant la même énergie (diffusion élastique), mais un vecteur d'onde différent. Lors des mesures de diffusion, on mesure le transfert de moment $\mathbf{q}$ en fonction des vecteurs d'onde du photon incident $\mathbf{k}_i$ et



Glace de spins artificielles produites par lithographie par faisceau d'électrons. a) Anneau de nanoaimants et réseau de glace de spins kagomé (b) et carrées (c) produites par lithographie par faisceau d'électrons. Pour a) et b), les nanoaimants ont une longueur et largeur de 60 nm et 20 nm respectivement, pour c) 470 nm et 80 nm. L'échelle (en blanc) représente 200 nm.

du photon diffusé $\mathbf{k}_f$ en utilisant :

$$\mathbf{q} = \mathbf{k}_f - \mathbf{k}_i$$

Le taux de transition w entre l'état fondamental $|0\rangle$ et l'état de transition $|n\rangle$ de la diffusion résonante est donné par la règle d'or de Fermi :

$$w = \frac{2\pi}{\hbar} \left|\langle f| H'_{int} |i\rangle\right|^2 \delta(E_f - E_i)$$

où $\hbar$ est la constante de Planck réduite, E_i et E_f les niveaux d'énergie de l'état initial et de l'état fondamental et H'_{int} l'Hamiltonien décrivant le système (section 3.1.2). Le dernier terme représente la conservation de l'énergie.

A la résonance ($E_i = E_f = \hbar\omega$), l'amplitude totale de la diffusion est donnée par [119, 136]:

$$f(\mathbf{q}, \hbar\omega) = f_0(\mathbf{q}) + f_{mag}(\hbar\omega) + f_{res}(\hbar\omega) \tag{C.1}$$

Le terme f_0 correspond à la diffusion non-résonante, également appelé diffusion Thomson. Ce terme est toujours présent et est le responsable de l'apparition des pics de Bragg de la structure de l'échantillon (section 4.3.1). Le dernier terme f_{mag} est également un terme relié à la structure (section 3.1.2). Enfin, le terme f_{res} est le terme responsable de la sensibilité de la diffusion aux propriétés magnétiques des matériaux. On peut le décomposer en [119,120] :

$$f_{res} \approx f_c(\mathbf{e}^*_\lambda \cdot \mathbf{e}_\lambda) - i f_m(\mathbf{e}^*_\lambda \times \mathbf{e}_\lambda) \cdot \mathbf{z} \tag{C.2}$$

avec $\mathbf{e}_\lambda$ et $\mathbf{e}^*_\lambda$ sont les vecteurs unitaires du photon incident et du photon diffusé respectivement. Les termes f_m et f_c sont des termes complexes indiquant une sensibilité au magnétisme et à la structure à la résonance (section 3.1.2).

Faire des mesures de diffusion équivaut à mesurer le transfert de moment $\mathbf{q}$. Les mesures effectuées ne sont pas en espace réel, mais en espace réciproque qui correspond à la transformée de Fourier de l'espace réel (section 3.2). Idéalement, on veut mesurer la magnitude et la phase en même temps pour pouvoir faire le lien directement entre les deux espaces. En pratique, on ne mesure que l'intensité, qui correspond au carré de la magnitude, et l'information sur la phase est perdue. Pour pouvoir comprendre les diagrammes de diffusion et obtenir des informations sur l'état de la magnétisation dans l'échantillon, nous avons comparé l'expérience avec des simulations obtenues à partir de la théorie cinématique de la diffusion des rayons X (section 4.2.1) [154]. Nous avons étendu cette théorie hors du plan de diffusion, pour pouvoir comparer directement nos simulations

avec les diagrammes mesurés à l'aide de notre détecteur bidimensionnel (section 4.2.2), et obtenir ainsi des informations statistiques sur l'échantillon [9].

Principaux résultats

Paramètres expérimentaux

Pour les expériences de diffusion résonante, nous avons utilisé des échantillons de glace de spins artificielle avec la géométrie carrée et la géométrie kagomé (figure 4.1). Dans les deux cas, les nanoaimants ont une longueur de 230 nm et une largeur de 80 nm, avec une épaisseur de 20 nm de Permalloy et une couche de 5 nm d'aluminium pour les protéger de l'oxydation. Le paramètre du réseau carré est égal à 310 nm et celui du réseau kagomé à 550 nm. Ces nanoaimants sont formés d'un seul domaine magnétique et leurs moments magnétiques sont fixes à température ambiante.

Les mesures ont été effectuées à l'aide du diffractomètre RESOXS localisé sur la ligne de lumière SEXTANTS au synchrotron SOLEIL [149, 150]. Comme la magnétisation des nanoaimants est dans le plan, nous avons effectué nos expériences en réflexion (section 4.1.2). Le faisceau de photons X arrive sur l'échantillon avec un angle d'incidence de 8 degrés. Le diagramme de diffusion est enregistré à l'aide d'une caméra CCD Princeton de 2048 $\times$ 2048 pixels située à 30 centimètres de l'échantillon. Le détecteur permet de détecter une gamme de moments de transfert dans la direction horizontale de $\Delta q_x = \pm$ 2.10^{-1} nm^{-1} et dans la direction verticale de $\Delta q_z = \pm$ 1 nm^{-1}. Ce diffractomètre est également équipé de bobines qui ont permis d'appliquer un champ magnétique jusqu'à 1200 G (0.12 T) [149].

Glace de spins carrée

Pics antiferromagnétiques dans l'état déposé

La figure ci-contre montre la structure et l'organisation magnétique de la glace de spins carrée, ainsi que les diagrammes de diffusion expérimentaux correspondant.

Sous le seuil d'absorption d'un élément, la diffusion résonante n'est sensible qu'aux informations sur la structure du système, lié au terme f_0 non-résonant dans l'expression de l'amplitude totale de diffusion (section 3.1.2). L'organisation structurelle de la glace de spins carrée permet de décrire le réseau comme la combinaison de deux sous-réseaux (en blanc et gris). La cellule unitaire est formée de deux nanoaimants, un provenant de chaque sous-réseau (panneau a). Pour être sensible aux deux sous-réseaux simultanément, les mesures sont effectuées avec le faisceau de photons parallèle à la diagonale du réseau total (flèches noires dans la figure). Si ces mesures étaient effectuées avec le faisceau parallèle à l'un des sous-réseaux, nous n'aurions accès qu'à la magnétisation de ce dernier [86]. Le diagramme de diffusion obtenu sous le seuil d'absorption L_3 du fer présente uniquement les informations sur la structure du réseau carré (panneau b). La présence des pics de Bragg indiquent que notre échantillon est parfaitement cristallin.

Au seuil d'absorption, la diffusion devient sensible à l'organisation magnétique dans le système. Dans le panneau c, on a représenté l'organisation de plus basse énergie de la magnétisation dans la glace de spins carrée (vertex de type I). Comme indiqué dans la section 1.4.2, des observations par microscopie de force magnétique ont permis d'observer la formation de large domaines de type I [58,170]. La cellule unitaire magnétique fait deux fois la taille de la cellule unitaire structurale (panneau a). Par conséquent, sa représentation en espace réciproque donne des pics de Bragg situés à des distances intermédiaires par

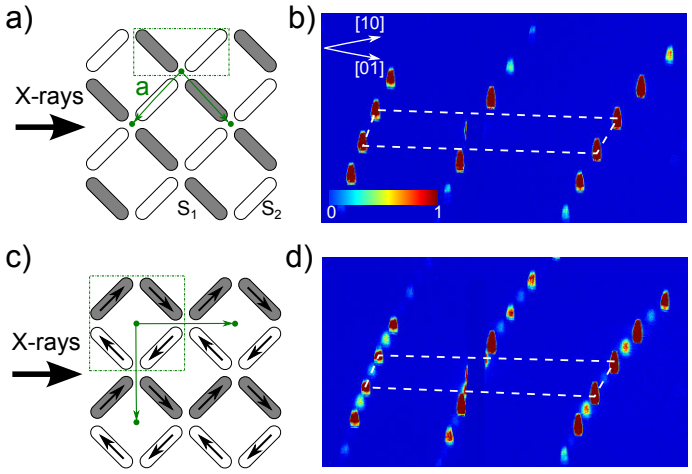


Diagramme de diffusions de la glace de spins carrée dans l'état déposé. a) Structure de l'échantillon. On a indiqué la cellule unitaire de structure à l'aide d'une boîte en pointillée. Elle contient deux nanoaimants avec des orientations différentes qui forment deux sous-réseaux S_1 et S_2 (en gris et blanc). Les vecteurs de répétition de longueur a sont indiqués en vert. b) Diagramme de diffusion enregistré sous le seuil d'absorption L_3 du Fe(690 eV), qui contient uniquement des informations de structure. c) Organisation magnétique de la glace de spins carrée dans l'état déposé. La cellule unitaire magnétique est indiquée par une boîte en pointillée. d) Diagramme de diffusion enregistré au seuil d'absorption L_3 du Fe (706.8 eV). Il contient des informations structurelles et magnétiques. Les pics de Bragg additionnelssitués aux positions intermédiaires sont d'origine magnétique.

rapport à la réflexion spéculaire (faisceau direct réfléchi). C'est la situation observée dans le diagramme de diffusion du panneau d. On peut donc conclure que l'émergence de nouveaux pics par rapport à la situation hors-résonance est dûe à l'organisation à longue-distance dans l'état déposé de la glace de spins carrée (section 4.3.1).

Inversion de la magnétisation

Lorsqu'on applique un champ externe suffisamment fort pour saturer l'échantillon, les pics de Bragg magnétiques disparaissent (figure 4.11). Tous les moments magnétiques se retrouvent alignés avec le champ externe, et les cellules unitaires structurelle et magnétique sont équivalentes. Pour suivre l'état de la magnétisation dans le réseau, on utilise la composante magnétique des pics de Bragg à l'aide du dichroïsme circulaire magnétique des rayons X (XMCD) (section 3.1.1). A chaque étape sur la boucle d'hystérésis, deux diagramme de diffusion sont mesurés avec des photons polarisés circulairement à droite et à gauche. En effectuant la soustraction entre les deux diagrammes, on obtient le diagramme dichroïque qui fournit des informations sur l'état de la magnétisation du système (section 4.3.4.

En suivant l'évolution du contraste dichroïque, nous avons tracé les courbes d'hystérésis des pics de Bragg du premier et du deuxième ordre de diffraction, avec $h^2 + l^2 = 1$ et $h^2 + l^2 = 2$ respectivement (figure 4.12). Les pics de premier ordre (10) et (01) sont sensibles aux sous-réseaux du système. En effet, à cause de la différence d'alignement de 1,5 degrés entre le champ externe et la diagonale du réseau carré, ces deux pics ont une valeur différente de champ coercitif. Pour le pic (10), il est égal à 475 Oe et pour le pic (01) à 455 Oe. On ne retrouve pas cette différence pour les pics du second ordre $(1\bar{1})$ et $(\bar{1}1)$ qui donnent la même valeur de champ coercitif, 468 Oe (section 4.3.3). Ce

dernier comportement indique que les pics de second ordre ne donnent d'information que sur la magnétisation totale de l'échantillon contrairement aux pics de premier ordre (section 4.3.3).

Contribution des sous-réseaux à la magnétisation rémanente

Pour déterminer la contribution de chacun des sous-réseaux à la magnétisation à rémanence M_r du réseau, nous avons utilisé des simulations numériques (section 4.2.3). Ces simulations ont été effectuées pour différentes configurations des sous-réseaux S_1 et S_2 jusqu'à atteindre le meilleur accord avec les résultats expérimentaux.

Pendant l'inversion de la magnétisation, la magnétisation totale du réseau est liée au nombre de moments magnétiques renversés N^- par rapport à la situation à saturation N. On peut calculer la valeur normalisée de la magnétisation rémanente par rapport à la magnétisation à saturation $\mathcal{M}_r = M_r/M_{sat}$ en utilisant la relation $\mathcal{M}_r = (N^+ - N^-)/N = 1 - 2N^-/N$ où N^+ est le nombre de moments magnétiques qui n'ont pas été renversés et $N = N^+ + N^-$. Comme précisé plus tôt, M_r est déduit du contraste dichroïque des pics de second ordre. Par conséquent, connaissant M_r et N, on peut remonter aux nombres de moments magnétiques qui ont été renversés ou non dans chacun des sous-réseaux S_1 et S_2 grâce au comportement dichroïque différent des pics de Bragg du premier ordre.

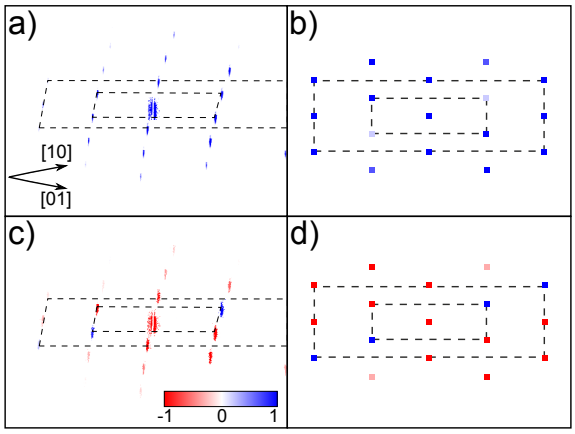
On présente dans la figure ci-contre le résultat de notre méthode pour deux valeurs différentes du champ magnétique. Dans les deux cas, nos simulations reproduisent quantitativement les résultats expérimentaux. Les diagrammes de diffusion a) et c) ont été enregistrés à rémanence après avoir appliqué un champ externe, de 480 Oe et -472 Oe respectivement. Le diagramme simulé b) a été obtenu avec 81 % des moments magnétiques du sous-réseau S_1 ont été renversés, et 72 % dans le sous-réseau S_2. Celui du panneau d) a été obtenu quand ces valeurs sont de 73 % et 20 % respectivement.

Cette méthodologie permet de reproduire le comportement des pics de Bragg jusqu'au troisième ordre (section 4.3.4). Au-dessus, des différences commencent à apparaître pour les raisons suivantes. Tout d'abord, les pics de grand ordre de diffraction sont sensibles aux petites distances dans l'échantillon. Notre modèle repose sur des nanoaimants réguliers, avec des tailles et des formes identiques. Ce n'est pas le cas en réalité où il existe une distribution de tailles et de formes à cause de l'effet de proximité (section 2.3.1). Ensuite, le modèle considère que les nanoaimants ne sont formés que d'un seul domaine magnétique et sont similaires à des macro-moments magnétiques. Les simulations micromagnétiques que nous avons effectuées montrent en réalité que l'aimantation tourne aux extrémités des nanoaimants pour réduire le champ fuyant de ses plus proches voisins (figure 4.15) [155].

Glace de spins kagomé

Diffusion magnétique

L'organisation de la glace de spins kagomé dans son état déposé est plus complexe que celle de la glace de spins carrée (figure 4.17c). La forte frustration de ce réseau conduit à une grande dégénération des niveaux d'énergie, avec son augmentation lorsque la taille du système augmente [6, 70]. Le système a par conséquent plus de probabilité de rester dans un minimum local d'énergie potentiel que d'atteindre son état fondamental. Il y a donc peu de chance d'obtenir un ordre magnétique à longue distance mais plutôt un ordre à courte distance comme on peut le voir dans la figure 4.17c. Par conséquent, le diagramme de diffusion ne comporte pas de nouveaux pics de Bragg mais un signal diffus. Ce signal est faible avec une intensité comparable à celle du bruit du détecteur (figure 4.17d). Il



Comparaison entre diagrammes de diffusion dichroïques expérimentaux et simulés. (a) et (c) ont été mesurés pour des valeurs de champ magnétique de 480 Oe et -472 Oe. Les meilleurs résultats numériques sont présentés en (b) et (d) [9].

disparaît lorsqu'un champ magnétique externe est appliqué sur l'échantillon. Dans ce cas, toutes les corrélations à courte distance disparaissent lors de la saturation, où tous les moments magnétiques pointent dans la direction du champ.

Comportement sous champ

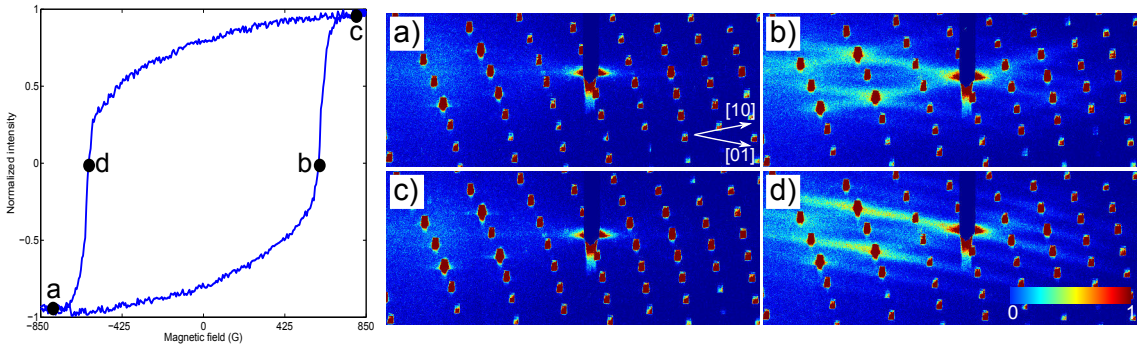
Nous avons étudié le comportement sous champ du signal diffus comme reproduit dans la figure ci-après (section 4.4.3). Aucun signal n'est observé à saturation (diagramme a et c) lorsque tous les moments sont alignés dans la direction du champ. Quand un champ magnétique est utilisé pour renverser l'aimantation, un signal diffu est à nouveau observé. D'après nos simulations (figure 4.21), il correspond à la nucléation et à la croissance de chaînes de Dirac, qui sont des chaines de moments magnétiques renversés [65]. Les diagrammes b et d de la figure ont été enregistrés aux valeurs du champ coercitif. L'asymétrie des deux entre les diagrammes de diffusion est liée aux bobines utilisées pour appliquer le champ magnétique [149]. Nous suspectons une différence de comportement entre les quatre bobines qui affecte la direction du champ magnétique (section 4.4.3).

Le signal diffus est lié à la direction des chaînes de Dirac dans le réseau. Si les chaînes sont dans la direction [01], le signal est dans la direction [10] et vice-versa; un signal dans les deux directions indiquent la présence de chaînes dans les deux directions de l'espace.

Nous avons également suivi l'évolution du contraste dichroïque des pics de Bragg, comme nous l'avons fait pour la glace de spins carrées. On observe ici aussi une inversion étape par étape du signal dichroïque (section 4.24). Il est cependant moins aisé d'obtenir des informations quantitatives, à cause de la symétrie plus élevée du système. La seule remarque que nous pouvons faire est la suivante : l'inversion du contraste dichroïque se produit le long des directions de la diffusion diffuse, suggérant une inversion locale de la magnétisation qui mène à une inversion de la magnétisation à de plus grandes distances.

Difficultés et solutions

Interpréter les résultats expérimentaux dans le cadre de la glace de spins kagomé est plus complexe que pour la glace carrée. La plus haute symétrie et dégénération des niveaux d'énergie en est sans doute l'une des causes, mais les possibilités techniques et d'analyses ne sont pour l'instant pas satisfaisantes (section 4.4.4).



Diffusion diffuse pendant l'inversion de l'aimantation de l'échantillon. Nous présentons à gauche une courbe d'hystérésis enregistrée à la position spéculaire à l'aide d'une photodiode. A droite se trouvent quatre diagrammes de diffusion enregistrés pour des valeurs différentes du champ magnétique.

L'analyse de la diffusion magnétique est problématique. Nous savons à l'aide de simulations simples (figure 4.21) que l'information sur les chaînes de Dirac se trouve dans le signal diffus. Nous avons tenté de faire un profil de ce signal en coupant le diagramme de diffusion dans la direction perpendiculaire au signal. On obtient trois pics que l'on peut faire concorder avec des fonctions de type gaussienne ou lorentzienne. Nous avons analysé une série de mesures expérimentales et de simulations numériques de cette manière, mais n'avons trouvé aucune corrélation quantitative entre les deux (figure 4.22).

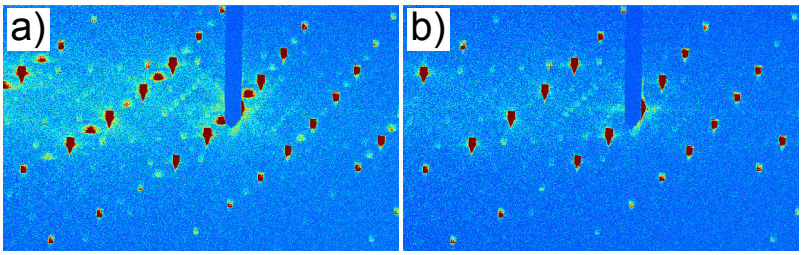
La principale difficulté de l'analyse provient de la convolution de la taille et de la divergence du faisceau incident avec le signal diffus. Nous ne tenons pas en compte de ce phénomène dans nos simulations. Cette convolution limite la résolution accessible avec la caméra CCD. La raison de cette convolution est le fait que nous avons réparti les pics de Bragg sur plusieurs pixels pour éviter la saturation du détecteur et enregistrer la diffusion diffuse. Pour éviter ceci, nous pourrions utiliser un film continu qui nous permettrait de n'enregistrer que les informations reliés au magnétisme (section 4.4.4).

Études complémentaires

Introduction de défauts dans la glace de spins carrée

Une solution pour faciliter l'analyse de la diffusion magnétique peut être de connaître la taille et le nombre de chaînes de Dirac dans le système. Bien que cela soit difficile dans un système où le désordre est aléatoire, on peut imaginer contrôler la nucléation et la croissance de ces chaînes en introduisant des nanoaimants agissant comme des points de nucléation et d'arrêt [171].

Nous avons introduit dans un réseau carré de tels nanoaimants, et nous avons effectué des mesures préliminaires de diffusion (section 5.1). Les quelques mesures sont préliminaires, mais nous savons d'ores et déjà que le système semble s'organiser dans son état de plus basse énergie lors de la déposition, comme la glace de spins non modifiée, avec la présence de pics de Bragg magnétiques dans le diagramme de diffusion (figure ci-contre). De plus, on observe la présence de pics de Bragg additionnels hors de la résonance dûs à l'introduction de nouvelles périodicités dans le système. Pour éliminer ces artéfacts structuraux, les nanoaimants doivent être introduits aléatoirement dans le réseau. On n'observe pas en revanche de diffusion diffuse qui est sans doute trop faible pour être observé dans les conditions utilisées.



Effet de l'introduction de désordre sur le diagramme de diffusion. Le diagramme a) a été enregistré après déposition et b) après saturation de l'échantillon. Les deux ont été enregistré à 706.5 eV avec des photons polarisés gauche.

Dépendance en température du diagramme de diffusion

Pour vérifier la présence de transitions de phase dans la glace de spins artificielle [163], est de reproduire l' expérience en diffusion résonante pour profiter de la spécificité chimique des rayons X. Nous avons utilisé le diffractomètre RESOXS à la source de lumière suisse. Cet instrument présente l'avantage d'être ans champ magnétique. Les échantillons étudiés sont similaires à ceux de la section précédente. Seule la couche protectrice diffère avec l'utilisation de 5 nm d'aluminium à (section 5.2).

La caméra CCD de l'instrument n'étant pas disponible au moment des mesures, les spectres ont été acquis avec une photodiode. Mesurés à différentes températures, ceux-ci ne présentent pas de différences claires. De plus, on ne peut pas distinguer du bruit un possible signal diffus. Enfin, on observe sur les spectres des pics de Bragg situés à d'autres positions de l'espace réciproque (figure 5.4). Ceci à cause de la fente ituée à l'avant du détecteur qui intègre une large zone de l'espace réciproque. Pour une mesure plus précise, un masque comportant un trou unique devrait être utilisé.

Conclusions

Des pics de Bragg purement magnétiques sont observés dans la glace de spins carré. Ceci est lié à l'organisation antiferromagnétique des vortex lors de la déposition. Cette information, bien que déjà connue par des mesures microscopiques, a été confirmée par la diffusion, indiquant que ce phénomène s'étend sur de larges domaines. Même lorsque ces pics ont disparu après l'application d'un champ magnétique externe, nous avons été capable de suivre l'évolution de l'aimantation dans le système grâce à la composante magnétique des pics de Bragg extraite grâce au dichroïsme circulaire magnétique des rayons X. Avec l'aide d'un modèle statistique simple, nous avons pu obtenir des informations quantitatives sur l'état de la magnétisation dans les deux sous-réseaux de la glace de spins carrée.

Un signal de diffusion magnétique a été observé dans l'état initial de la glace de spins kagomé. Nous avons corrélé son existence à la présence d'ordres à courte distance dans l'échantillon, surtout sous la forme de chaîne de moments magnétiques renversés. Cette diffusion magnétique a également été observée de manière reproductible lors de l'étude du système à plusieurs valeurs du champ magnétique. Nous avons discuté de la difficulté d'analyser ce signal, notamment à cause des difficultés induites par les conditions expérimentales. Nous avons également suivi l'évolution du signal dichroïque et montré que ces mêmes difficultés empêchaient une analyse rigoureuse du diagramme de diffraction.

Nous avons complété notre étude par des techniques complémentaires sur des systèmes différents. Des défauts ont été introduits dans la glace de spins carrée qui ne changent

pas les propriétés magnétiques du système, mais qui apportent de nouveaux signaux dans le diagramme de diffusion. Des expériences préliminaires de diffusion résonante ont été tentées à l'aide d'une photodiode, mais l'utilisation d'une caméra CCD reste nécessaire pour la bonne compréhension du diagramme de diffusion.

Pour conclure le travail présenté ici, on ne peut donner une réponse formelle aux deux questions introduites. En effet, des résultats prometteurs ont été obtenus, notamment en terme de détections de signaux magnétiques faibles à l'aide de la caméra CCD. Cependant des difficultés d'analyses dues à la nature du système ainsi qu'aux choix des paramètres expérimentaux empêchent, pour l'instant, une analyse plus poussée des données. Les études menées constituent néanmoins une première étape prometteuse dans l'étude de la glace de spins avec les techniques de l'espace réciproque. On peut d'ores et déjà imaginer utiliser des techniques avancées, comme la spectroscopie de corrélation de photons, qui donneront de plus amples détails sur la dynamique de la glace de spins artificielle.